Nickel-based Electrocatalysts for Urea-assisted Water Electrolysis

Jichao Zhang

A thesis presented for the degree of

Doctor of Philosophy

Supervised by

Professor Ivan P. Parkin

Professor Guanjie He

Department of Chemistry

University College London

April 2024

Declaration

I, Jichao Zhang, confirm that the work mentioned in my thesis is my own. Where information from other sources, I confirm that this has been presented in the thesis.

Abstract

The urea oxidation reaction (UOR) has become one of the most promising routes to substitute oxygen evolution reaction (OER) with large thermodynamic potential in various energy conversion applications. Nickel (Ni)-based materials were extensively applied as suitable UOR electrocatalysts with highly active Ni^{3+} species that can facilitate the urea dehydrogenation process. The currently reported UOR electrocatalysts mainly focus on minimizing the overpotential to drive the reactions and revealing the reaction mechanism by comparing the physicochemical properties before and after reactions. This leads to urgent issues for undesirable electrochemical performance for industrial applications at large current densities over long-term tests and unreliable mechanism exploration. Thus, the modified Ni-based electrocatalysts were proposed in this thesis for efficient and durable UOR and structure-performance relationships were established by *in situ* spectroscopy observation. Specifically, chromium (Cr)-doped Ni hydroxide catalysts ($Cr\text{-}Ni(OH)_2$) with unique wetting properties were first proposed to improve the UOR activity. The stability of Cr dopants was further probed to reveal the Cr leaching issues during the OER and UOR process. Second, to enhance the utilization efficiency of noble metal, single atomic ruthenium (Ru) sites were incorporated into the Ni hydroxide. The crucial roles of urea dehydrogenation and Ni oxidation in both low and high urea concentrations were disclosed, respectively. Zn-urea-air battery test and zero-gap membrane electrode assembly (MEA) test were conducted to validate the applicability in practical scenarios. Finally, platinum (Pt)-mediated Ni phosphide catalysts were synthesized to realize bifunctional activity for both electro-oxidation and electro-reduction, demonstrating a vision for urea-assisted water electrolysis. This thesis highlights the modification of Ni-based catalysts and reveals the reaction mechanism by *in situ* spectroscopic studies.

Impact statement

OER plays an essential role in numerous scenarios for energy conversion. However, the extensive application of most of the energy conversion scenarios is impeded by sluggish OER kinetics with the theoretical potential of 1.23 V *vs.* reversible hydrogen electrode (RHE). It is verified that the urgent issue of unfavorable energy efficiency for water electrolysis to produce hydrogen, metal-air batteries, CO_2 electro-reduction, and NOx electro-reduction stems from a lack of efficient and durable OER catalyst to lower the applied potential to drive the reaction under high current density over long-term operation to meet industrial requirements. Despite several promising achievements in developing OER catalysts, most of them are still undesirable with high overpotential. As compared with exerting enormous efforts to explore the highly effective OER catalysts, small molecule oxidation reactions have become new stream studies because of their relatively lower theoretical potential. Among those reactants, urea features with globally abundant and easily accessible from mammalian urine, sparking widespread research interest in developing suitable UOR catalysts.

The electro-generation of green hydrogen powered by renewable energy exhibits significant superiority over conventional grey hydrogen produced by steam reforming. During the water electrolysis process, high-purity hydrogen gas can be collected at the cathode, and oxygen gas can be obtained at the anode. However, low-value O_2 products and high overpotential originating from sluggish OER kinetics hamper further progress in practical scenarios, particularly at large scale. Therefore, it is of great significance to incorporate UOR to substitute OER for urea-assisted water electrolysis.

Ni-based materials, the popular UOR electrocatalysts, can form highly active Ni^{3+} species for urea dehydrogenation. Nevertheless, the electrochemical performance of the current UOR electrocatalysts is required to be further elevated to fulfil the criteria of industrial production. Motivated by the above concerns, in this thesis, the non-noble metal doping method was first used to modify the Ni-based catalysts to investigate the structure-performance relationship. The single atomic noble metal anchored Ni catalyst was subsequently proposed, which was followed by bifunctional Ni catalysts investigation. This thesis opens a new revenue for the modulation of Ni-based materials and establishes an understanding to unearth the reaction microenvironment at the interface from the perspective of *in situ* observation. The interesting findings could provide some inspiration for subsequent catalyst development and be extended to other energy conversion systems.

Research Paper Declaration Form 1

1. For a research manuscript that has already been published

a) **What is the title of the manuscript?**

Stabilizing efficient structures of superwetting electrocatalysts for enhanced urea oxidation reactions

b) **Please include a link to or doi for the work**

10.1016/j.checat.2022.09.023

c) **Where was the work published?**

Journal: Chem Catalysis

d) **Who published the work?** (e.g. OUP)

Elsevier

e) **When was the work published?**

13/10/2022

f) **List the manuscript's authors in the order they appear on the publication**

Jichao Zhang, Xuedan Song, Liqun Kang, Jiexin Zhu, Longxiang Liu, Qing Zhang, Dan J.L. Brett, Paul R. Shearing, Liqiang Mai, Ivan P. Parkin, Guanjie He

g) **Was the work peer reviewed?**

Yes

h) **Have you retained the copyright?**

No

i) **Was an earlier form of the manuscript uploaded to a preprint server?**

No

If 'No', please seek permission from the relevant publisher and check the box next to the below statement:

☒

*I acknowledge permission of the publisher named under **1d** to include in this thesis portions of the publication named as included in **1c**.*

2. For multi-authored work, please give a statement of contribution covering all authors

Jichao Zhang and Guanjie He conceived the project; Jichao Zhang designed the experiments, synthesized materials, and conducted electrochemical tests and characterization; Xuedan Song and Qing Zhang did DFT Calculations and analysis; Liqun Kang and Longxiang Liu took charge of spectroscopy and data analysis; Prof. Dan J.L. Brett, Prof. Paul R. Shearing, Prof. Ivan P Parkin supervised the project. Jichao Zhang drafted the initial manuscript; Jiexin Zhu and Liqiang Mai offered writing suggestions. All authors revised the manuscript.

3. **In which chapter(s) of your thesis can this material be found?**

   Chapter 2

4. **e-Signatures confirming that the information above is accurate** (this form should be co-signed by the supervisor/ senior author unless this is not appropriate, e.g. if the paper was a single-author work)

   Candidate

   Click or tap here to enter text.

   Date:

   Click or tap here to enter text.

   Supervisor/ Senior Author (where appropriate)

   Click or tap here to enter text.

   Date

   Click or tap here to enter text.

Research Paper Declaration Form 2

1. For a research manuscript that has already been published

a) **What is the title of the manuscript?**

Balancing Dynamic Evolution of Active Sites for Urea Oxidation in Practical Scenarios

b) **Please include a link to or doi for the work**

10.1039/D3EE03258B

c) **Where was the work published?**

Energy Environ. Sci.

d) **Who published the work?**

Royal Society of Chemistry

e) **When was the work published?**

30/10/2023

f) **List the manuscript's authors in the order they appear on the publication**

Jichao Zhang, Jiexin Zhu, Liqun Kang, Qing Zhang, Longxiang Liu, Fei Guo, Kaiqi Li, Jianrui Feng, Lixue Xia, Lei Lv, Wei Zong, Paul R. Shearing, Dan J. L. Brett, Ivan P. Parkin, Xuedan Song, Liqiang Mai and Guanjie He

g) **Was the work peer reviewed?**

yes

h) **Have you retained the copyright?**

No

i) **Was an earlier form of the manuscript uploaded to a preprint server?**

No

If 'No', please seek permission from the relevant publisher and check the box next to the below statement:

☒

*I acknowledge permission of the publisher named under **1d** to include in this thesis portions of the publication named as included in **1c**.*

2. For multi-authored work, please give a statement of contribution covering all authors

Jichao Zhang and Guanjie He conceived the project; Jichao Zhang designed the experiments, synthesized materials, and conducted electrochemical tests and characterization; Xuedan Song and Qing Zhang did DFT Calculations and analysis; Liqun Kang and Longxiang Liu took charge of spectroscopy and data analysis; Prof. Dan J.L. Brett, Prof. Paul R. Shearing, Prof. Ivan P Parkin supervised the project. Jichao Zhang drafted the initial manuscript; Jiexin Zhu, Fei Guo, Kaiqi Li, Jianrui Feng, Lixue Xia, Lei Lv, Wei Zong, and Liqiang Mai offered writing suggestions.

3. **In which chapter(s) of your thesis can this material be found?**

   Chapter 3

4. **e-Signatures confirming that the information above is accurate**

Candidate

Click or tap here to enter text.

Date:

Click or tap here to enter text.

Supervisor/ Senior Author (where appropriate)

Click or tap here to enter text.

Date

Click or tap here to enter text.

Research Paper Declaration Form 3

1. **For a research manuscript prepared for publication but that has not yet been published**

   a) **What is the current title of the manuscript?**

   Regulating reconstruction-engineered active sites for accelerated electrocatalytic conversion of urea.

   b) **Has the manuscript been uploaded to a preprint server?**

   No

   c) **Where is the work intended to be published?**

   Angew. Chem. Inter. Ed.

   d) **List the manuscript's authors in the intended authorship order**

   Jichao Zhang, Jianrui Feng, Jiexin Zhu, Liqun Kang, Longxiang Liu, Fei Guo, Jing Li, Kaiqi Li, Jie Chen, Wei Zong, Mingqiang Liu, Ruwei Chen, Ivan P. Parkin, Liqiang Mai and Guanjie He

   e) **Stage of publication**

   in submission

2. **For multi-authored work, please give a statement of contribution covering all authors**

   Jichao Zhang and Guanjie He conceived the project; Jichao Zhang is in charge of all experimental studies; Jianrui Feng did DFT Calculations and analysis; Jiexin Zhu, Liqun Kang, Longxiang Liu, Fei Guo, Jing Li, Kaiqi Li, Jie Chen, Wei Zong, Mingqiang Liu, Ruwei Che, Liqiang Mai provided suggestions and guidance. Prof. Ivan P Parkin supervised the project.

3. **In which chapter(s) of your thesis can this material be found?**

   Chapter 4

4. **e-Signatures confirming that the information above is accurate**

   Candidate

   Click or tap here to enter text.

   Date:

   Click or tap here to enter text.

Supervisor/ Senior Author (where appropriate)

Click or tap here to enter text.

Date

Click or tap here to enter text.

Acknowledgments

First and foremost, I am deeply indebted to all those who have helped me and supported me during my Ph.D. project.

Sincere thanks should be extended to Prof. Guanjie He and Prof. Ivan P. Parkin for their help and guidance during my Ph.D. at UCL. With their continued support and advice, I could learn a lot from them.

Then, I am thankful beyond measure to my intelligent colleagues and all my collaborators. It was an honor to work and study under their guidance. Also thank Dr. Steve Firth, Mr. Martin Vickers, and all UCL technicians for providing me the facility training and technical help.

I am also grateful beyond words to my parents for supporting me during this tough period.

Table of contents

List of Figures

Chapter 1. Introduction

Chapter 2. Methodology

Chapter 3. Non-noble metal doped Ni catalysts

Chapter 4. Single atomic noble metal modified Ni Catalysts

Chapter 5. Bifunctional Ni phosphide catalysts for urea-assisted water electrolysis

List of Tables

Chapter 1. Introduction

Chapter 3. Non-noble metal doped Ni catalysts

Chapter 4. Single atomic noble metal modified Ni Catalysts

Abbreviation

BCA	Bubble contact angle
C_{dl}	Double-layer capacitance
CV	Cyclic voltammetry
CP	Carbon paper
DFT	Density functional theory
DIW	Deionized water
EDS	Energy dispersive spectroscopy
EIS	Electrochemical impedance spectroscopy
EOR	Ethanol oxidation reaction
EXAFS	Extended X-ray absorption fine structure
HER	Hydrogen evolution reaction
HRTEM	High-resolution transmission electron microscope
HADDF-STEM	High-angle annular dark-field scanning transmission electron microscope
LSV	Linear sweep voltammetry
MEA	Membrane electrode assembly
MOR	Methanol oxidation reaction
MP-AES	Microwave plasma atomic emission spectrometers
NEXAFS	Near edge X-ray absorption fine structure
OCP	Open circuit potential
OER	Oxygen evolution reaction
PCET	Proton-coupled-electron-transfer
Pt/C	Platinum on carbon 20% weight loading
RHE	Reversible hydrogen electrode
RRDE	Rotating ring disk electrode
SACs	Single-atom catalysts
SAED	Selected area electron diffraction
SEM	Scanning electron microscope
UOR	Urea oxidation reaction
UV-vis	Ultraviolet-visible

WCA	Water contact angle
XANE	X-ray absorption near edge structure
XPS	X-ray photoelectron spectroscopy
XRD	X-ray diffraction

Chapter 1. Introduction

1.1 Background

Fossil fuels have been playing a key role in the development of the global economy since the first Industrial Revolution took place in Great Britain.[1] To drive our modern industrial world, the continuous exploitation of natural resources not only leads to their depletion but also the generation of industrial waste substances such as toxic gas (e.g. nitrogen dioxide, sulfur dioxide, and carbon monoxide), seriously affecting the ecological environment and the health of our human being.[2]

To reduce the impact of greenhouse gas and harmful substances accompanied by conventional industrial production, the iterative development of renewable energy, derived from wind, solar, hydropower, etc, has recently gained huge attention among research communities, which is expected to empower an industry of energy conversion.[3] The promising vision of the electro-generation of high-value-added chemical products is gradually achieved with the enormous progress of electrocatalytic studies to create an environmentally friendly and sustainable future.[4]

Hydrogen is a promising clean energy to substitute fossil fuels with a high energy density of 142 MJ kg^{-1}.[5] The continuous progress of hydrogen energy offers a promising route to realize carbon neutrality in the mid-21^{st} century.[6] The hydrogen source is widely distributed in nature.[7] The current widely-used method for hydrogen production is steam reforming of methane.[8] This process ($CH_4 + 2H_2O \rightarrow CO_2 + 4H_2$) requires enormous energy consumption to keep a high temperature of around 700 °C to drive the reaction with the assistance of catalysts, which is followed by the by-product formation of CO ($CH_4 + H_2O \rightarrow CO + 3H_2$) and the conversion step to generate CO_2 ($CO + H_2O \rightarrow CO_2 + H_2$).[9] As concluded in previous studies, there are several serious issues with this method, including the poisoning of catalysts attacked by CO and the complicated purification process to separate hydrogen from mixtures.[10] The sustained efficiency of hydrogen production could be seriously affected by the activity degradation brought by the inevitable poison of active sites.[11] The additional steps of the separation process further cause high costs.[12] Therefore, the environmental effect and low purity of hydrogen obtained from steam reforming of methane incur numerous concerns.

As a more attractive way of collecting green hydrogen, direct hydrogen production *via* water electrolysis is a hot research topic, triggering interest among a wide range of scholars all over the world.[13-15] The electrochemical water splitting process ($2H_2O \rightarrow 2H_2 + O_2$) encompasses high-purity hydrogen formed at the cathode and oxygen generated at the anode as shown in Figure 1.1. The simplified purification process could be realized with the assistance of a membrane, thus resulting in a low cost for separation from gas mixtures.[16] However, there are still numerous technical barriers to overcome for energy-saving and sustainable production to satisfy the eco-friendly requirements in this research area.[17] The first one is the development of effective catalysts.[18] Although countless studies are working on non-noble metal catalysts, Pt-based catalysts remain superior to other non-noble metal catalysts in terms of high activity and stability for hydrogen evolution reaction (HER).[19] In addition, the sluggish oxygen evolution reaction (OER) is another enormous issue.[20] Despite the tremendous effort to optimize the OER catalysts, the limit of the large thermodynamic potential of 1.23 V *vs.* RHE leads to a high overpotential to drive OER at a large current density.[21-23]

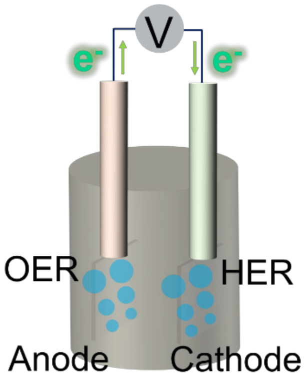

Figure 1.1. Schematic illustration of water electrolysis with HER at the cathode and OER at the anode.

There are also several challenges related to the storage and transportation of hydrogen.[24] Among those bottleneck issues for hydrogen energy, the high cost of hydrogen production arising from large electricity consumption seems the most urgent problem, seriously hindering the extensive applications of water splitting for hydrogen production.[25] Meanwhile, the sluggish OER is also the main reason for undesirable energy efficiency in metal-air batteries, CO_2 electro-reduction for C_{2+} chemicals production, and NOx electro-reduction for ammonium synthesis.[26-28]

Small molecule oxidation reactions have recently been suggested to replace OER due to their relatively lower theoretical potential.[29-31] Urea is easily accessible, non-toxic, and non-flammable and could be a great candidate for investigation.[32] Nickel-based catalysts with in situ generation of highly active Ni^{3+} species have been widely used for urea oxidation reaction (UOR).[33-35] Nonetheless, the electrochemical performance involving activity and stability still requires improvement, and the reaction mechanism understanding for the structure-performance relationship is expected to be established by *in situ* exploration. Therefore, in this chapter, the latest research on water electrolysis and urea-assisted hydrogen production, including the mechanism of HER, OER, and UOR, the latest UOR catalysts, and synthetic and characterization methods, has been outlined and summarized in terms of the electrochemical aspects.

1.1.1 Mechanism of HER

Using the electrochemical water splitting method to produce hydrogen is widely investigated and conducted in the alkaline medium, which is mainly due to the wide range of suitable catalysts for commercial applications.[36] As for water splitting in an acidic medium, only noble metals like Pt and Iridium (Ir) can sustain high efficiency over long-term operation.[37]

HER involves three steps with the hydrogen intermediates adsorption and desorption, including the Volmer step, Heyrovsky step, and Tafel step, which play a crucial role in affecting the kinetics of HER.[38] The first Volmer step proceeds with the dissociation of water molecules in an alkaline or neutral medium,[39] which is followed by the Heyrovsky step or the Tafel step as shown below:

Volmer step: $* + e^- + H_2O \rightarrow *H + OH^-$ (1.1)

Heyrovsky step: $*H + e^- + H_2O \rightarrow * + H_2 + OH^-$ (1.2)

Tafel step: $2*H \rightarrow 2* + H_2$ (1.3)

* is the active site of the catalyst.

When conducted in an acidic medium, a similar pathway without the dissociation of water. The hydrogen intermediate (*H) is subsequently converted to hydrogen by the Heyrovsky step or the Tafel step,[40] which is presented as follows:

Volmer step: $* + e^- + H^+ \rightarrow *H$ (1.4)

Heyrovsky step: $*H + e^- + H^+ \rightarrow H_2 + *$ (1.5)

Tafel step: $2*H \rightarrow 2* + H_2$ (1.6)

The reaction kinetics at the first Volmer step is affected by the domination of H^+ and OH^- in acid and alkaline environments.[41] The *H intermediates adsorption and desorption are considered as the rate-determining step (RDS) to form hydrogen as shown in Figure 1.2.

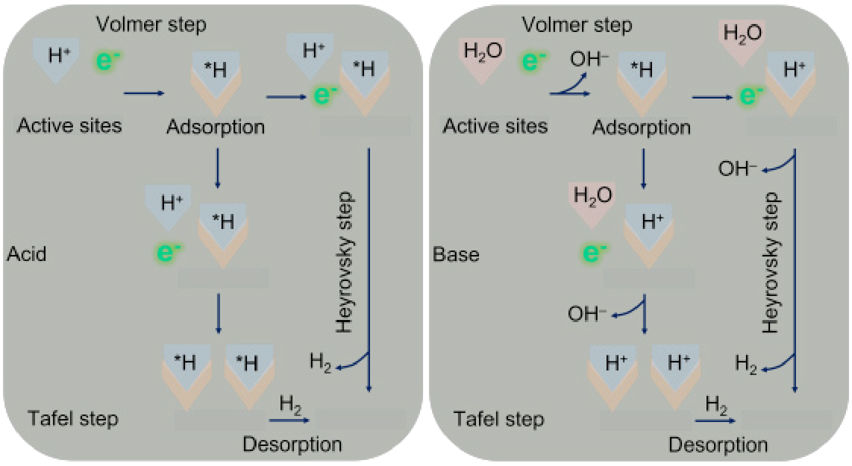

Figure 1.2. Schematic illustration of reaction pathway for HER in both acid and base medium.

It was claimed that the moderate bonding strength between hydrogen and active sites is a determining factor in evaluating the performance of HER catalysts.[42] Too strong or too weak bonding strength can lead to unsatisfactory hydrogen efficiency.[43] Using hydrogen adsorption energy (ΔG_H) close to zero as a descriptor for the evaluation of HER performance is suggested.[44] Noble metals such as Pt and Ir were selected as the most suitable materials to catalyze the HER process with lower overpotential.[45] As for non-noble metals, Ni, cobalt (Co), and copper (Cu) exhibit relatively higher HER activity, but currently, it is hard to be on par with Pt-based catalysts in terms of activity and durability at a wide range of pH value mediums.[46] Therefore, it is of great significance to modify the Pt-based catalysts with lower loading mass to reduce the high cost for commercial application. Moreover, taking into account the scarce source of noble metal, more efforts are still desired to modulate the non-noble catalysts to achieve Pt-like electrocatalytic performance.

1.1.2 Mechanism of OER

OER is another crucial half-reaction at the anode for water electrolysis when paired with HER at the cathode.[47] Meanwhile, OER also plays an essential role in energy storage and conversion scenarios, such as Zn-air battery, CO_2 electro-reduction, and NOx electro-reduction.[48] Different from the HER reaction pathway, the OER process involves a four-electron transfer process with a large thermodynamic potential of 1.23 V *vs.* RHE.[49] A significantly higher kinetic barrier than HER induces obstructed progress for water splitting to produce hydrogen at a large scale.

The reaction pathway of OER in an acidic medium is presented as follows:[50]

Step 1: $* + H_2O \rightarrow *OH + H^+ + e^-$ (1.7)

Step 2: $*OH \rightarrow *O + H^+ + e^-$ (1.8)

Step 3: $*O + H_2O \rightarrow *OOH + H^+ + e^-$ (1.9)

Step 4: $*OOH \rightarrow * + O_2 + H^+ + e^-$ (1.10)

* is the active site of the catalyst.

However, the reaction pathway of OER in the neutral and basic medium is quite different from that of in the acidic medium as shown below:[51]

Step 1: $* + OH^- \rightarrow *OH + e^-$ (1.11)

Step 2: $*OH + OH^- \rightarrow *O + H_2O + e^-$ (1.12)

Step 3: $*O + OH^- \rightarrow *OOH + e^-$ (1.13)

Step 4: $*OOH + OH^- \rightarrow * + O_2 + H_2O + e^-$ (1.14)

The continuous progress of developing active and durable OER catalysts can ameliorate high overpotential, particularly at high current density. Iridium oxides (IrO_2) and Ruthenium oxides (RuO_2) are widely selected as suitable materials to catalyze OER.[52] Despite the promising progress of non-noble metal-based catalysts, the stability issues of those materials over the long-term operation in an acid medium still cannot be well fixed.[53] The Ir or Ru-based materials are the most widely used catalysts due to their relatively stable in strong acid electrolytes.[54] However, with the limit of a huge theoretical potential of 1.23 V *vs.* RHE, even the best OER performance still possesses the large overpotential to meet the industrial requirement at a large current density. Therefore, leveraging alternative anode reactions to realize green hydrogen production with reduced energy consumption is of great significance.

1.1.3 Mechanism of UOR

Small molecule oxidation reactions, involving methanol, ethanol, hydrazine, hydroxymethylfurfural, urea, and glucose, have recently aroused the attention of research communities due to their relatively lower thermodynamic potential.[55] Among those reactants, urea is reputed to be sufficient in human urine and industrial urea-bearing wastewater.[56] UOR with a low thermodynamic potential (0.37 V *vs.* RHE) is extensively employed to substitute the sluggish OER due to non-flammable, non-toxicity, and a wide variety of sources, saving about 70% of electrical energy and simultaneously realizing urea-bearing wastewater treatment.[57] Particularly, as compared to seawater electrolysis to produce hydrogen, UOR requires a lower applied potential than chlorine evolution reaction (1.36 V *vs.* RHE), obviating chlorine formation to cause pollution.[58]

Exploration of the UOR mechanism in different mediums would facilitate the subsequent development of catalysts and guide further optimization in practical applications. As for an acidic medium, almost only the Pt-based catalysts can suffer from the strong acid electrolyte to catalyze the urea dissociation.[59] The final products are mainly nitrogen (N_2) and carbon dioxide (CO_2). The studies of UOR in saline or neutral environments are also rarely reported. A chloride (Cl)-mediated UOR mechanism was proposed in terms of Pt, Ir, Ru, and Ti metals, boron-doped diamond, and metal oxide-based catalysts.[60] Nonetheless, complicated intermediates and by-products were incorporated (*e.g.* chloramines and oxychlorides).

Despite the possibility of urea oxidation in acidic and neutral mediums, alkaline electrolytes were predominantly used. UOR usually proceeds in alkaline conditions with a multi-proton-coupled-electron-transfer (PCET) process.[61] The classical reaction pathway contains a six-electron transfer process ($CO(NH_2)_2 + 6\ OH^- \rightarrow N_2 + CO_2 + 5\ H_2O + 6\ e^-$), involving numerous C or N-intermediates, adsorption or desorption processes and dehydrogenation processes of those intermediates.[62] It is noted that the generated CO_2 would be immediately reacted with hydroxide anion to form carbonate (CO_3^{2-}), realizing effective *in situ* carbon capture to avoid greenhouse emissions.[63]

Different from the HER and OER as discussed above, the complicated UOR process leads to great challenges in obtaining a thorough understanding of the reaction microenvironment during the UOR process. Moreover, advanced *in situ* characterization methods are still required to capture the short-lived intermediates and detect phase transformation and structure evolution for the establishment of novel structure-performance relationships towards a wide range of effective UOR catalysts. Additionally, theoretical calculations, such as adsorption energy and difference charge density, are essential for researchers to figure out the reaction mechanism and provide reliable directions for the following experimental studies.

1.2 Electrocatalysts for UOR

The development of UOR catalysts originated in the 1970s. To realize highly efficient and durable UOR to assist water electrolysis for hydrogen production, continuous exploration of catalysts with promising activity and outstanding stability is carried out. The current prevalent electrocatalysts for UOR can be mainly divided into two categories, noble metal-based and non-noble metal-based metals.

1.2.1 Noble metal-based catalysts

In 1973, UOR was catalyzed by Pt anode with the products of N_2, H_2O, and CO_2 for the first time.[64] Over the next half-century, some noble metal-based catalysts were suggested to be able to enhance UOR activity, involving Platinum (Pt), Iridium (Ir), and Ruthenium (Ru).[65] Nonetheless, the UOR performance of those noble metal catalysts was still undesirable for applications in different scenarios, due to the limit of large overpotential, insufficient stability, and easy inactivation when operating over hundreds of hours. In addition, extensively utilizing those noble metals could remarkably lead to high cost for water electrolysis to obtain green hydrogen, which is due to their scarcity to access and expensive price. Therefore, noble metal-based catalysts are not the best choice, which requires further optimization to reduce the loading mass of noble metal for commercial applicability and practical employment prospects.

1.2.2 Non-noble metal-based catalysts

As compared to the imperfection of noble metal-based catalysts, developing non-noble metal-based UOR catalysts has been a mainstream study in the area of energy conversion scenarios.[66] In 2009, non-noble metal Ni-based materials were proposed for the first time to accelerate urea conversion.[67] After that, non-noble metal-based catalysts have been continuously proposed, which exhibit competitive UOR performance and outperform noble metal catalysts.[68]

Nickel (Ni)-based metal catalysts, such as hydroxides, oxides, and phosphides, can effectively facilitate urea dehydrogenation, which has already been extensively employed to replace OER in alkaline medium.[69] As reported by previous studies, the NiOOH species was considered as the real active site. This is due to the overpotential of Ni hydroxide ($Ni(OH)_2$) catalysts close to NiOOH formation.[70] The possible UOR mechanisms for NiOOH sites encompass two steps, which is the electrochemical-chemical (EC) oxidation mechanism as presented below:[71]

Electrochemical step: $6\ Ni(OH)_2 + 6\ OH^- \leftrightarrows 6\ NiOOH + 6\ H_2O + 6\ e^-$ (1.15)

Chemical step: $6\ NiOOH + CO(NH_2)_2 + H_2O \rightarrow 6\ Ni(OH)_2 + N_2 + CO_2$ (1.16)

Overall reaction: $CO(NH_2)_2 + 6\ OH^- \rightarrow N_2 + 5\ H_2O + CO_2 + 6\ e^-$ (1.17)

As for the classical EC mechanism, the generation of Ni^{3+} species (NiOOH) relies on a self-oxidation process, involving $Ni(OH)_2$ oxidized to NiOOH with the consumption of OH^-. Immediately after the electrochemical step, urea dehydrogenation can proceed at NiOOH active sites with the products of N_2 and CO_2 formation. Simultaneously, the NiOOH active sites are chemically reduced to $Ni(OH)_2$, which is followed by the regeneration of NiOOH active species with the reaction of the OH^- and $Ni(OH)_2$.

Despite the broad application of Ni-based catalysts, the complicated intermediates adsorption-desorption and multi-PCET process impose a limit on further improvement in electrochemical performance. Several material design strategies have been suggested to modify the Ni-based materials in terms of promoted generation of NiOOH active species and effective construction of novel active sites.[72]

As the typical active sites for UOR, abundant NiOOH species play an essential role in sustaining the high activity for Ni-based materials. It is noted that inadequate conductivity of NiOOH obtained from direct synthesis leads to the requirement of the E-step from Ni^{2+} through surface reconstruction to drive the UOR. Regulating the morphology with various rough micro-nano structures is usually employed to facilitate the generation of sufficient active species.[73] For example, Ding *et al.* proposed an ultrathin $Ni(OH)_2$ nanomesh by a modified hydrolysis method.[74] According to the results of scanning electron microscopy (SEM), transmission electron microscopy (TEM), and energy dispersion spectroscopy (EDS), a large specific surface area was observed (Figure 1.3). It was verified that $Ni(OH)_2$ nanomesh possess superior activity than conventional $Ni(OH)_2$ nanoparticles due to more active sites.

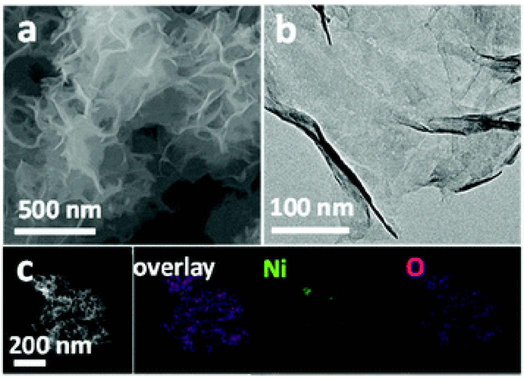

Figure 1.3. (a)-(b) SEM and TEM images of $Ni(OH)_2$ nanomesh. (c) EDS mapping images.[74] (Copyright, 2019, Royal Society of Chemistry).

Liu *et al.* successfully synthesized nickel phosphide (Ni_2P) catalysts on carbon cloth (CC) with nano-porous structures by leveraging hydrothermal and phosphorization methods as shown in Figure 1.4. The enhanced area of active sites, rapid electrolyte diffusion, and boosted mass transfer, could result in notable UOR performance improvement.[75]

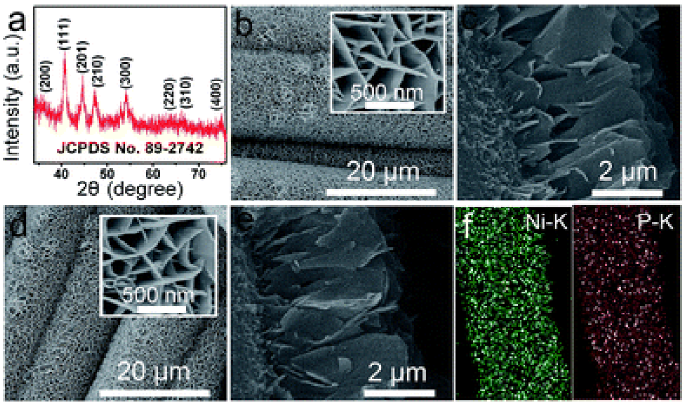

Figure 1.4. (a) XRD pattern of Ni_2P. (b)-(c) SEM images of the Ni precursor for further low-temperature phosphide reaction. (d)-(f) SEM and EDS images of Ni_2P.[75] (Copyright, 2017, Royal Society of Chemistry).

Additionally, Hu *et al*. reported a nickel nitride (Ni_3N) catalyst with a bead-like nanospheres structure on the nickel foam (Figure 1.5). Superior UOR performance originating from enriched NiOOH active sites was discovered.[76]

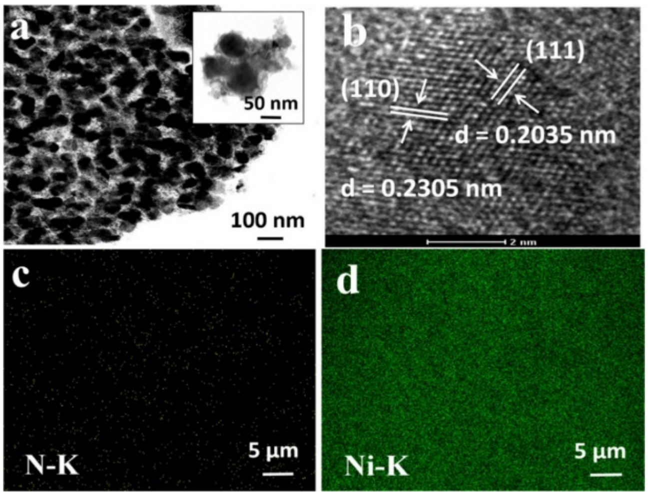

Figure 1.5. (a)-(b) TEM images of Ni_3N. (c)-(d) EDS mapping of Ni_3N.[76] (Copyright 2019, American Chemical Society).

Additionally, the heterogeneous metal atom doping strategy is another widely used method to enhance the generation of high-active NiOOH species. Yu *et al.* proposed a nickel molybdate ($NiMoO_4$) catalyst on nickel foam (Figure 1.6) with a nanorod structure by using hydrothermal and thermal annealing methods.[77]

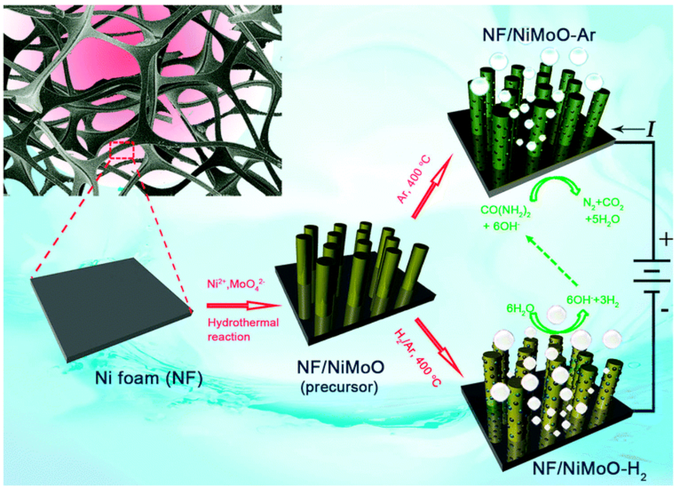

Figure 1.6. Schematic illustration of the fabrication process of the NiMO catalysts.[77] (Copyright, 2018, Royal Society of Chemistry).

The enhanced UOR performance could be ascribed to sufficient active Ni^{3+} sites. Besides, the existence of Mo^{6+} had a significant effect on regulating the electronic structure of Ni atoms, resulting in a boosted Ni oxidation process of Ni^{2+} transited to Ni^{3+}.

Xie *et al.* claimed that Cu-doped $Ni(OH)_2$ nanoarrays with hierarchical wire-on-sheet structure (Figure 1.7) possessed outstanding UOR performance. Ni^{3+} active species were demonstrated as high active sites for UOR.[78]

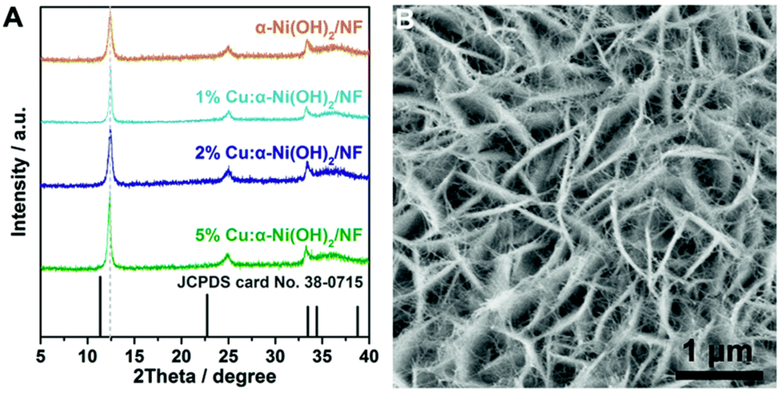

Figure 1.7. (a) XRD patterns of Cu-doped $Ni(OH)_2$ catalysts. (b) SEM images of nanosheets.[78] (Copyright, 2019, Royal Society of Chemistry).

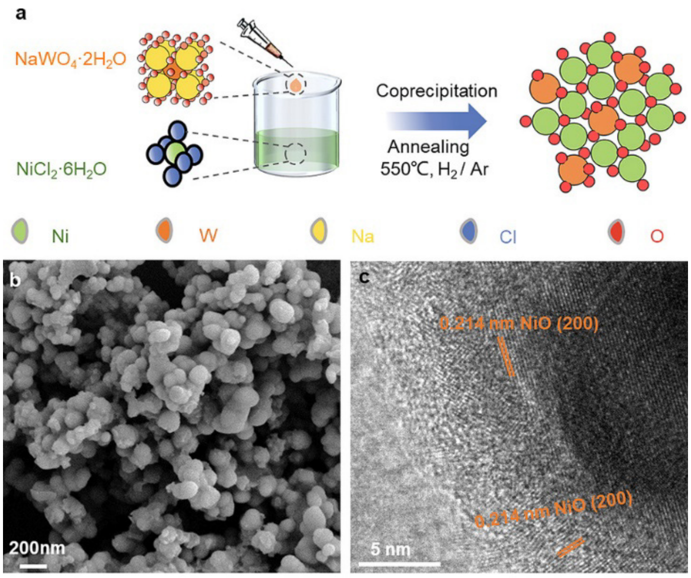

Figure 1.8. (a) schematic illustration of the fabrication process of Ni-WOx. (b)-(c) morphology characterization.[66] (Copyright 2021, John Wiley and Sons).

As shown in Figure 1.8, Wang *et al.* synthesized a Ni-based catalyst with the doping of tungsten (Ni-WO_x).[66] This catalyst presented superior activity towards UOR, requiring only 1.6 V *vs.* RHE to drive a current density of 440 mA·cm^{-2}. The reaction microenvironment during the UOR process would be modified by doping of W sites with charge redistribution of Ni sites, thus leading to the abundant Ni^{3+} active sites to boost the UOR performance.

Recently, Ni-based metal-organic frameworks (MOFs) catalysts, have also been extensively studied for highly efficient urea conversion. MOF-based materials exhibit well-defined crystalline micro-nano porous structures and encompass metallic cation centers with varying ligands, exhibiting adjustable physiochemical properties towards boosting the generation of NiOOH active sites. For example, Pan *et al.* proposed Fe, Mn, and Ni-doped ZIF-67-derived hollow polyhedron frame catalysts (Figure 1.9).[79] Ni-doped catalysts manifested optimal UOR performance. Furthermore, the outstanding activity with an onset potential of 1.43 V *vs.* RHE at 10 mA cm^{-2} and long-term stability over 25 hours were discovered.

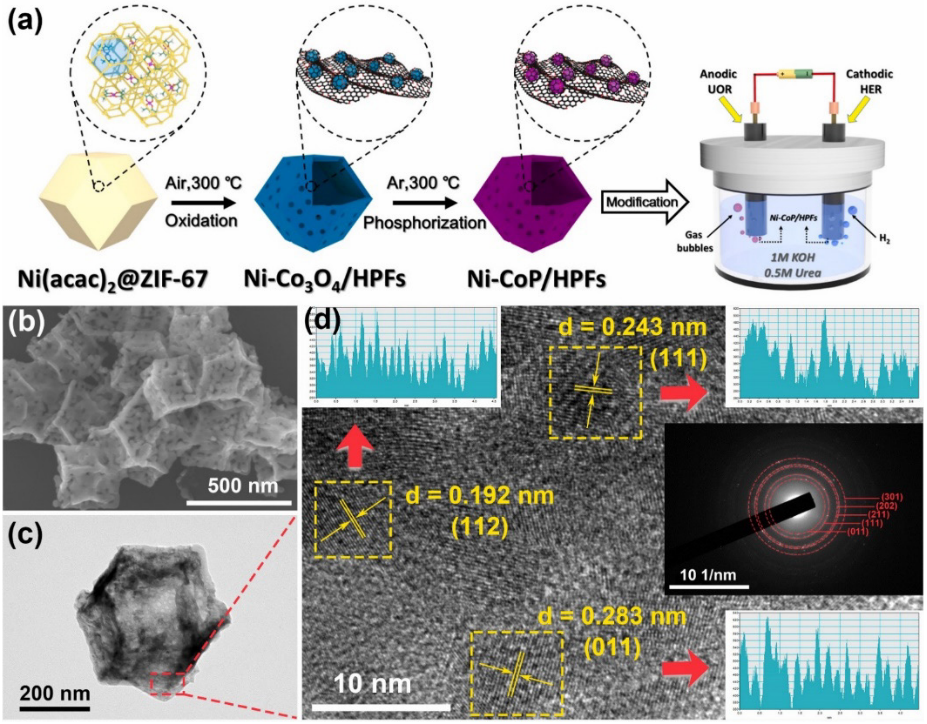

Figure 1.9. (a) Schematic illustration of the fabrication process. (b)-(d) morphology characterization.[79] (Copyright 2019, Elsevier).

Wang *et al.* synthesized Ni-doped carbon catalysts with micro-nano porous pomegranate-like structures, by using a solvothermal method with Ni-zinc (Zn)-based MOF as a self-template (Figure 1.10).[80] The UOR performance was evaluated and required 1.6 V *vs.* RHE to reach 10 mA·cm^{-2}. The large area of well-dispersed Ni active site (NiOOH) porous structure morphology was verified as the main factor in enhancing the UOR activity.

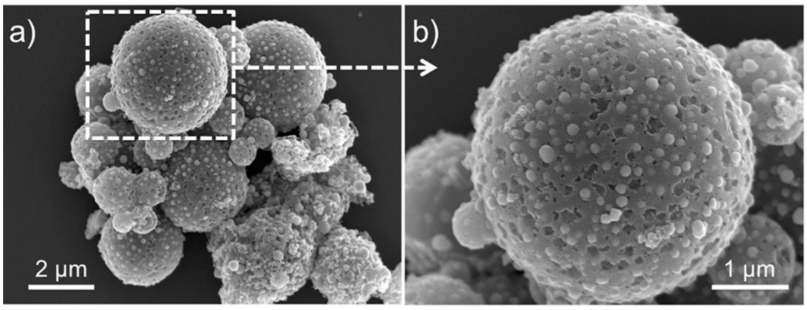

Figure 1.10. SEM images of Ni-doped carbon catalysts derived from NiZn-MOF template.[80] (Copyright 2018, American Chemical Society).

Furthermore, except for Ni-based UOR catalysts, the incorporation of other transition metal-based catalysts, such as cobalt (Co), manganese (Mn), or molybdenum (Mo), could achieve competitive UOR activity. Li *et al.* proposed a CoS_2/MoS_2 Schottky catalyst with the heterojunctions structure (Figure 1.11). The large area of active sites enabled charge redistribution and rapid mass transfer.[81] The CoMo-based catalysts facilitated the adsorption and decomposition of urea molecules and the C or N-intermediates. Only a low potential of 1.29 V *vs.* RHE was required to drive 10 mA cm^{-2} and possessed 60 hours of stability test without notable activation degradation. Liu *et al.* fabricated Zn-doped CoP catalysts with nanoarray structure. The UOR performance was validated and it was found that only a cell voltage of 1.38 V *vs.* RHE could drive 10 mA·cm^{-2}. According to the investigation of the reaction microenvironment during the UOR process, the real active species were CoOOH.[82] Chen *et al.* proposed a manganese dioxide (MnO_2)-based catalyst. It was verified that 2D micro-nano ultrathin nanocrystalline morphology could boost the UOR performance and only a cell voltage of 1.41 V *vs.* RHE was required to reach the current density of 10 mA·cm^{-2}.[83]

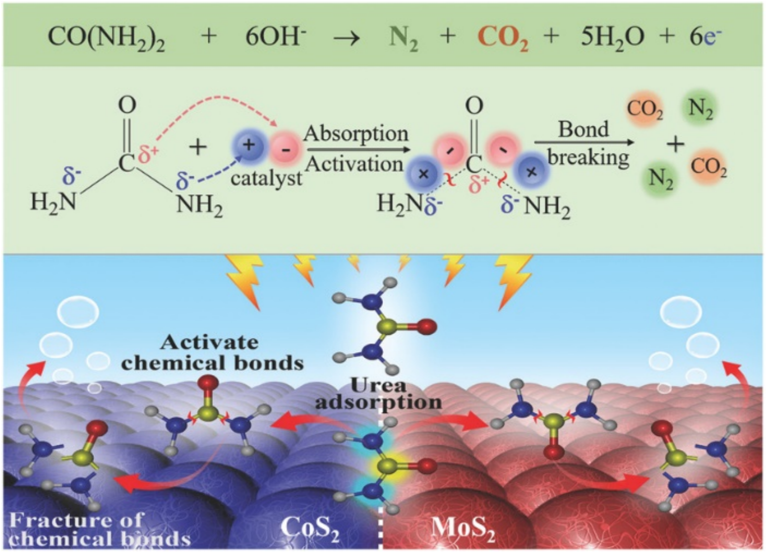

Figure 1.11. Schematic illustration of UOR mechanism of CoS2/MoS2 Schottky catalyst.[81] (Copyright 2018, John Wiley and Sons).

Despite numerous studies of developing highly efficient and durable UOR catalysts since 1973, it is noted that most of the researchers are still focusing on the optimization of Ni-based catalysts. Aiming to achieve superior UOR performance, the exploration of novel active sites is also carried out to further empower the Ni-based catalysts to extend the surface NiOOH mechanism. For example, dual active sites Ni ferrocyanide ($Ni_2Fe(CN)_6$) electrocatalysts were discovered by Qiao's group as shown in Figure 1.12.

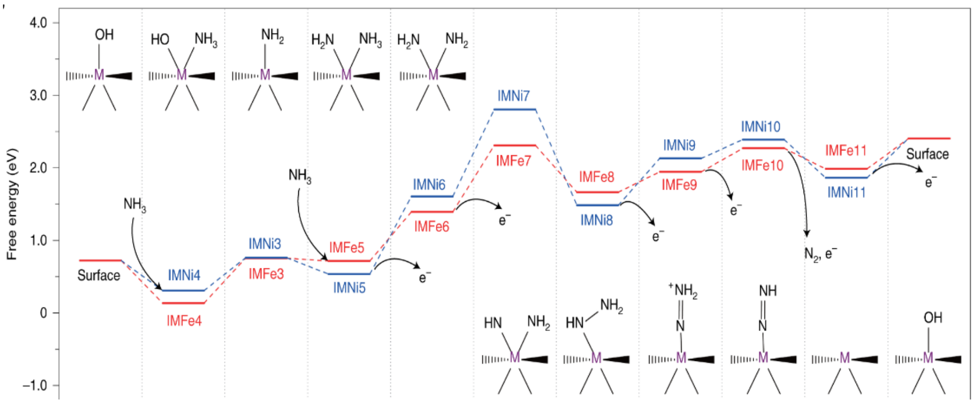

Figure 1.12. Reaction pathway diagrams for $Ni_2Fe(CN)_6$ electrocatalysts.[84] (Copyright 2021, Springer Nature).

The Ni^{2+} and Fe^{2+} dual active sites were validated to be effective in catalyzing urea. It was discovered that Ni^{2+} sites were conducive to converting urea to ammonium (NH_3) and CO_2, and Fe^{2+} sites were favorable for NH_3 dehydrogenation to form N_2.[84]

Single atomic catalysts (SACs) with well-defined structures have recently been suggested to improve atom utilization and electronic structure modulation for Ni-based catalysts. Li *et al.* proposed an ultrathin NiO anchored Ru-Co dual-atom support catalyst as shown in Figure 1.13. The potential to drive 10 mA cm^{-2} is 1.288 V vs RHE. The favorable electronic structure was incorporated by the unique heterointerface.[72] Lee *et al.* prepared atomic Rh sites on Co_3O_4. The potential to drive 10 mA cm^{-2} is 1.28 V vs RHE. The Rh sites would facilitate the adsorption/activation of urea molecules and stabilize the crucial intermediates to elevate UOR performance.[59] Zhang *et al.* claimed that Ni single atoms anchored on N-doped carbon nanosheet catalysts (Ni SACs-NC) possessed superior UOR performance. The unique $Ni-N_4$ sites could effectively modulate the electronic structure and stabilize the UOR intermediates.[85]

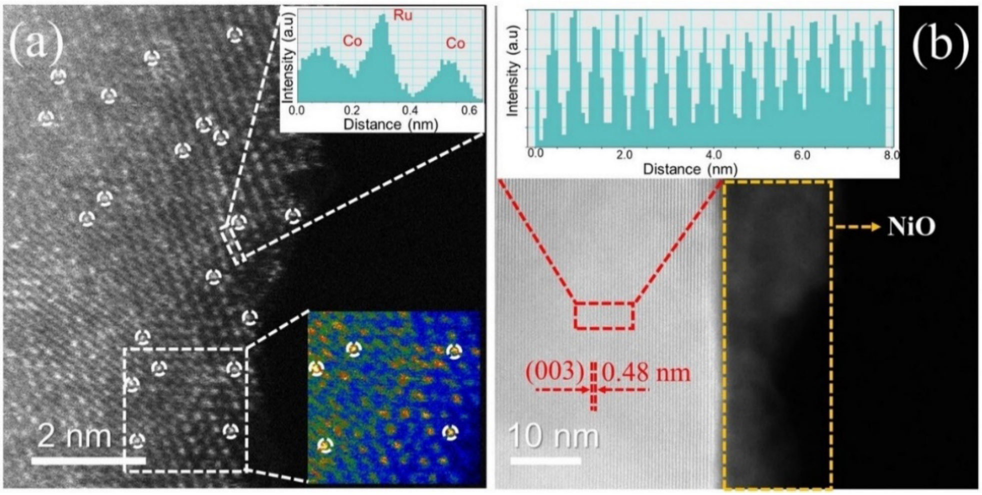

Figure 1.13. HAADF-STEM image of Ru-Co dual-atom support. (Copyright 2023, John Wiley and Sons).

Except for improving the catalytic activity, the selectivity of UOR was also reported. The competition issues between UOR and OER were revealed by Lin *et al.* The $NiWO_4$ catalysts were prepared as a proof-of-concept. According to the spectroscopic studies, it could be found that sufficient Ni^{3+} active sites would mitigate the contest of shared active sites between OER and UOR.[68] In addition, the over-oxidation of urea to form the nitrite has been recently reported. Savinova *et al.* analyzed the reaction pathway of Ni-based catalysts with different products (Figure 1.14). Different from the conventional carbonate pathway to form N_2 and CO_3^{2-}, the NO^{2-} and CNO^- would also form at high potential.[86]

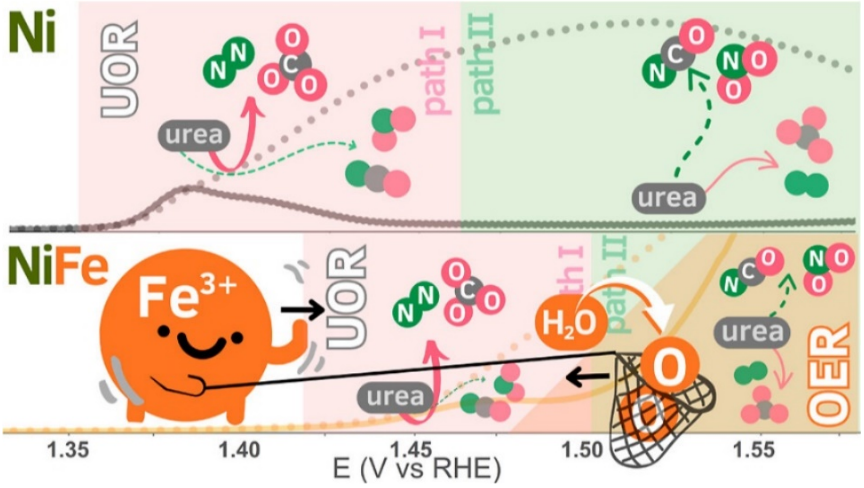

Figure 1.14. The schematic illustration of carbonate and cyanate reaction pathway. (Copyright 2023, American Chemical Society).

Klinkova *et al.* also reported over-oxidation of urea with formation of NOx (Figure 1.15). The reaction pathway could be steered by altering the composition of the catalyst.[87]

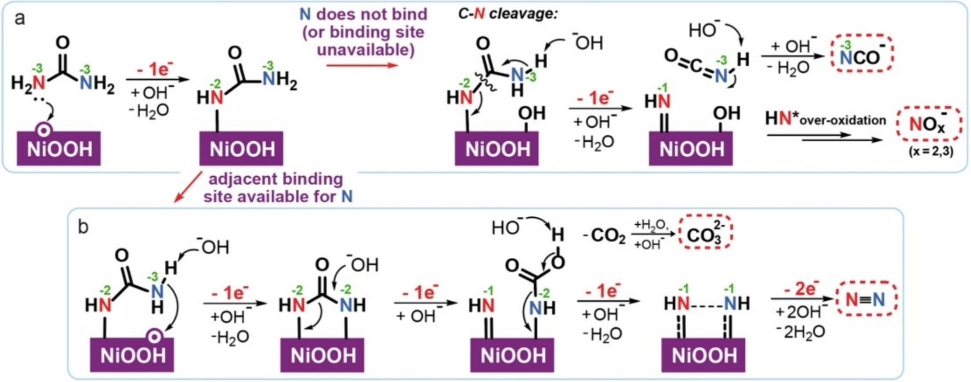

Figure 1.15. The schematic illustration of the reaction pathway for NOx. (Copyright 2022, John Wiley and Sons).

Yang *et al.* proposed a polyaniline-coating strategy to locally enrich the urea molecule for elevating the selectivity of N_2 products to suppress the over-oxidation of urea to form nitrite (Figure 1.16).[88]

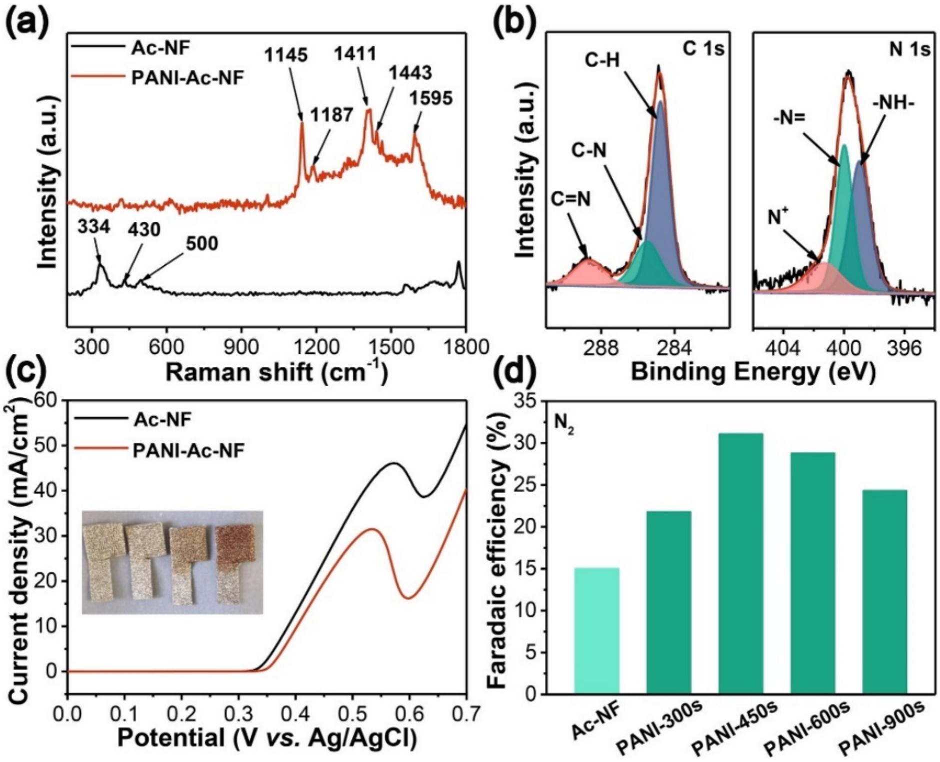

Figure 1.16. The polyaniline-coating strategy to improve the selectivity of N_2 products. (Copyright 2021, John Wiley and Sons)

The studies of novel active sites with unique reaction mechanisms for Ni-based catalysts are still in the early stages of investigation, which requires more cutting-edge *in situ* characterization methods to detect the short-lived intermediates and the evolution of active sites during the UOR process. Additionally, the selectivity of UOR still requires to be elevated to suppress OER and high-value products should be explored instead of low-value N_2 products.

The potential that is required to reach 100 mA cm^{-2} of recently reported UOR catalysts is summarized in Table 1.1, it could be found that there is still huge room for improvement of electrochemical performance in the way to gain more reliable findings for subsequent development of catalysts. The highly efficient UOR catalysts with lower overpotentials require further exploration and investigation.

Table 1.1. UOR performance of recently reported UOR electrocatalysts.

Catalyst	Potential at 100 mA cm^{-2} (V *vs.* RHE)	Urea concentration	Reference
Rh/NiV-LDH	1.38	0.33 M	[89]
W-$Ni(OH)_2$	1.38	0.5 M	[90]
Ni-Mo-S	1.39	0.5 M	[91]
NiS	1.39	0.33 M	[92]
MoO_2-MoO_3/Ni_2P	1.39	0.5 M	[93]
Fe-$NiCo_2S_4$/Ni_3S_2	1.39	0.5 M	[94]
V-Ni_3N	1.40	0.33 M	[95]
NiWOx	1.40	0.33 M	[66]
NiMoV LDH	1.40	0.33 M	[96]
Ni_3Se_2/MoO_2@$Ni_{12}P_5$	1.40	0.5 M	[97]
Cu-$Ni(OH)_2$	1.41	0.33 M	[78]
NiMoP	1.41	0.5 M	[98]
$Ni(OH)_2$@NF	1.43	0.33 M	[99]
CA-Ni/NiO@NCS	1.43	0.5 M	[100]
Ni-Mn-Se	1.44	0.33 M	[101]
Fc-NiCo-BDC	1.44	0.33 M	[102]
Mn-Co LDH	1.45	0.33 M	[103]
NiFe LDH	1.46	0.33 M	[104]
VS_2	1.46	0.33 M	[105]
CoNiOP/NF	1.48	0.33 M	[106]
NiMo alloy	1.50	0.33 M	[107]
CoMoO@Co/GF	1.51	0.5 M	[108]

Ni$_{1.5}$Co$_{1.5}$-O/CC	1.52	0.33 M	[109]
Ni MOF	1.53	0.33 M	[73]
NiFe-F	1.53	0.33 M	[110]
Co, V-NiS$_2$	1.54	0.33 M	[111]
NiFeCoSx@FeNi$_3$	1.56	0.33 M	[112]
NiF$_3$/Ni$_2$P@CC	1.57	0.33 M	[113]
F-P-Co$_3$O$_4$/NF	1.62	0.5 M	[114]
Co$_3$S$_4$	1.67	0.33 M	[115]

1.3 Challenges and Objectives

Creating green hydrogen with an energy-saving process to drive our society in the future causes a large demand for promising electrocatalysts to boost water electrolysis. UOR exhibits the potential to assist hydrogen production due to the abundant sources of urea-bearing wastewater. Despite the numerous studies of UOR catalysts, particularly focusing on Ni-based materials over the last ten years, the undesirable UOR performance in terms of activity and stability still requires to be elevated. Moreover, the majority of the studies only focused on lowering the potential to drive the UOR, ignoring the investigations of reaction mechanisms or gaining unreliable conclusions based on results before and after reactions. Furthermore, the validation of practical scenarios to replace OER with UOR is still rarely reported based on device tests for energy conversion applications. Therefore, there is still a lot of room in this area to achieve the goal of urea-assisted water electrolysis.

The strategies to overcome the above challenge could be summarized as follows: (1) Selecting the transition metal with partially filled d electrons to modulate the electronic structure of Ni active sites. (2) incorporating unique morphologies to tune the wetting properties and interfacial electric field to boost mass and electron transfer to stabilize crucial intermediates for achieving sufficient active sites. (3) Employing the *in situ* characterization methods to reveal the reaction mechanism during the UOR process. (4) designing and preparing large-scale measurements with large current density to bridge the gap between fundamental research and industrial applications.

Based on the above strategies, the objectives for realizing urea-assisted water electrolysis can be divided into different sub-goals. Exploring the UOR pathways for different Ni-based catalysts plays a crucial role in subsequent electrocatalyst design to meet requirements of practical applications with promising activity (lower overpotential) and outstanding durability over long-term operations. This is because the catalytic reaction pathway can vary for a specific Ni-based catalyst. Therefore, it holds great consequence to explore reaction microenvironments during the UOR process for Ni-based catalysts.

The *in situ* advanced characterization methods, such as Raman, XAS, FTIR, and DEMS, are expected to be widely applied to reflect the reaction microenvironments in real time. Furthermore, theoretical calculations based on density functional theory (DFT) are required to predict efficient catalysts and gain more reliable catalytic mechanisms based on experimental studies, such as reaction pathways, synergetic effects between various dopants, and active site analysis.

In addition, choosing earth-abundant and inexpensive materials as precursors or striving to lower the loading mass of noble metal catalysts is the primary goal of setting up new UOR catalysts for large-scale applications. To achieve commercial applicability, high-performance UOR catalysts are required to be synthesized by facile, environmentally friendly, and cost-effective fabrication methods. Moreover, how to realize the lab-to-fab process remains a huge challenge. For example, the direct usage of urea-bearing wastewater like urine is rarely reported. The complicated compositions of urine would probably affect the sustainable efficiency of active sites. Furthermore, most of the studies only worked on the development of catalysts, overlooking the device test in practical scenarios. To achieve the goal of urea-assisted water electrolysis for hydrogen production, the zero-gap membrane electrode assembly (MEA) test under large current density should be performed to validate the applicability of as-prepared catalysts.

The outline of this thesis could be summarized based on the objectives as shown in Figure 1.17.

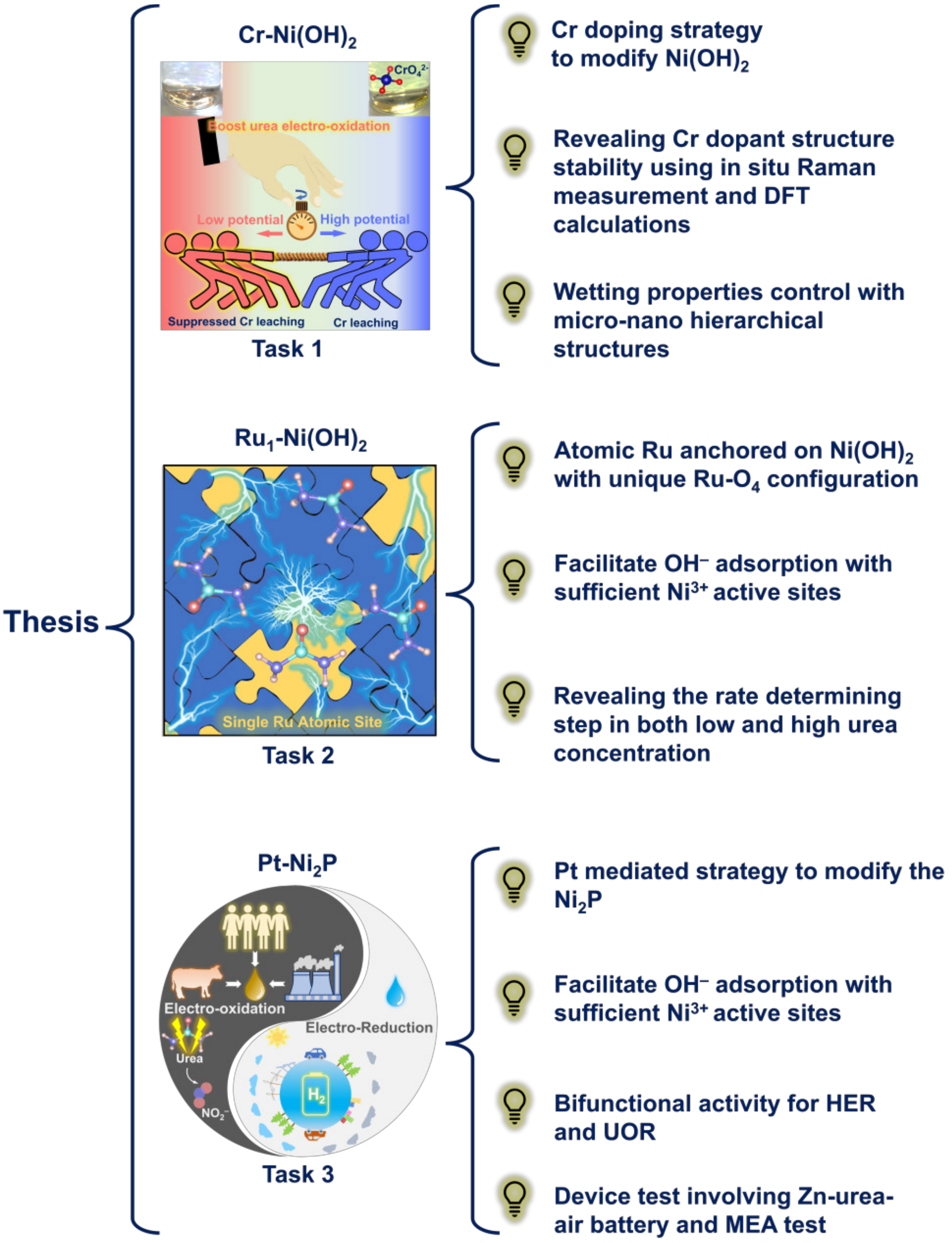

- Cr doping strategy to modify $Ni(OH)_2$
- Revealing Cr dopant structure stability using in situ Raman measurement and DFT calculations
- Wetting properties control with micro-nano hierarchical structures

- Atomic Ru anchored on $Ni(OH)_2$ with unique $Ru-O_4$ configuration
- Facilitate OH^- adsorption with sufficient Ni^{3+} active sites
- Revealing the rate determining step in both low and high urea concentration

- Pt mediated strategy to modify the Ni_2P
- Facilitate OH^- adsorption with sufficient Ni^{3+} active sites
- Bifunctional activity for HER and UOR
- Device test involving Zn-urea-air battery and MEA test

Figure 1.17. The overview of each task in this thesis.

Specifically, in the first task, the non-noble metal-doped Ni catalysts were first synthesized as the proof-of-concept to verify the stability of dopant structures during oxidation reactions. Chromium (Cr) with half-filled electrons in the d orbital has a wide range of oxidation states, which have been extensively used as dopants to regulate the electronic structure of active sites and stabilize the intermediates. However, the dopant stability issue is often overlooked by the research community. By combining the *in situ* spectroscopic observation and DFT calculations, the Cr leaching issues were revealed during the process of OER and UOR, respectively. The urea molecules would preferentially adsorb on the surface to suppress the Cr leaching into the electrolytes with the formation of chromate. Additionally, the co-precipitation of different feed ratios between Ni and Cr precursors under alkaline media could lead to the formation of hydroxide with different morphologies, thus enabling modulation of wetting properties to obtain well-designed pathways for electrons, ions, and generated gas substances.

As for the second task, the noble metal-doped Ni catalysts were then synthesized with an atomic heterostructure engineering strategy. Ruthenium (Ru) possesses unfilled electrons in d orbitals and a wide range of oxidation states, which also exhibit the potential to modify the Ni-based catalyst to generate abundant active sites. However, the high cost hinders their utilization for wide application. Single-atom catalysts (SAC) possess well-defined structures and high atom utilization efficiency, which can aid the establishment of structure-performance relationships. Therefore, $Ru\text{-}O_4$ coordinated configuration anchored on Ni hydroxide catalysts was proposed to facilitate the adsorption of OH^- to boost the electrochemical step to form abundant Ni^{3+} active sites. In addition, the critical roles of urea dehydrogenation and Ni oxidation in both low and high urea concentrations were unveiled by *in situ* spectroscopy observation.

Finally, a bifunctional Ni catalyst with both HER and UOR performance was proposed to realize urea-assisted water electrolysis. Instead of separating the fabrication process and assembling single-functionality catalysts, bifunctional electrocatalysts can enable reduced overall costs by simplifying the fabrication of anode and cathode to preclude leveraging varying precursors and procedures. Due to the same composite, The cross-contamination can also be ameliorated during the surface reconstruction over the long-term operation. Platinum (Pt) possesses a partially filled 5d orbital, which can facilitate interaction with various molecules, enabling fast electron transfer around the reaction microenvironments. Pt still exhibits higher activity and durability than non-noble metal catalysts. Additionally, Ni phosphides possess superior metallic properties and Pt-like HER performance. Therefore, a Pt-mediated strategy was proposed to modify the Ni phosphide. The electron redistribution around Pt-Ni sites and favorable adsorption of OH^- boost the formation of abundant dynamic Ni^{3+} active sites. Zn-urea-air battery and zero-gap MEA test were employed to validate the vision of replacing OER with UOR.

1.4 References

1. J. E. Garzón Baquero; D. Bellon Monsalve. *Int. J. Hydrogen Energy*, **2024**, *54*, 574-585.

2. D. Vadgama; R. Srivastava; S. Shinde. *Mater. Today:. Proc.*, **2024**, *1*, 2214.

3. Q. Hassan; P. Viktor; T. J. Al-Musawi; B. Mahmood Ali; S. Algburi*, et al. Renew. Energy Focus*, **2024**, *48*, 100545.

4. X. Zhang; S. Feizpoor; M. Humayun; C. Wang. *Chem Catal.*, **2024**, *4*, 100840.

5. S. Feng; D. Li; H. Dong; S. Xie; Y. Miao*, et al. Appl. Catal., B*, **2024**, *342*, 123451.

6. H. Bhattarai; A. P. K. Tai; M. Val Martin; D. H. Y. Yung. *Sci Total Environ*, **2024**, *906*, 167759.

7. R. Blay-Roger; W. Bach; L. F. Bobadilla; T. R. Reina; J. A. Odriozola*, et al. Renew. Sustain. Energy Rev.*, **2024**, *189*, 113888.

8. R. Yang; X. Che; B. Deng; Y. Lin. *Int. J. Hydrogen Energy*, **2024**, *61*, 238-250.

9. B. Zhang; Y. Li; R. Zhang; G. Liu; Z. Sun*, et al. Chem. Eng. Sci.*, **2024**, *292*, 120026.

10. F. V. Maziviero; D. M. A. Melo; R. L. B. A. Medeiros; J. C. A. Silva; T. R. Araújo*, et al. J. Energy Inst.*, **2024**, *113*, 101523.

11. Y. Li; Y. Wang; J. Wu; S. Gao; B. Zhu*, et al. Chem. Eng. Sci.*, **2024**, *291*, 119906.

12. W. Li; J. Zhang; W. Wang. *Coord. Chem. Rev.*, **2024**, *503*, 215638.

13. H. Zhao; Z. Y. Yuan. *Adv. Energy Mater.*, **2023**, *13*, 2300254.

14. J. C. Ehlers; A. A. Feidenhans'l; K. T. Therkildsen; G. O. Larrazábal. *ACS Energy Lett.*, **2023**, *8*, 1502-1509.

15. F.-Y. Gao; P.-C. Yu; M.-R. Gao. *Curr. Opin. Chem. Eng.*, **2022**, *36*, 100827.

16. Q. Hassan; A. Z. Sameen; H. M. Salman; M. Jaszczur. *Energy Harvesting and Systems*, **2024**, *11*, 20130011.

17. T. Terlouw; C. Bauer; R. McKenna; M. Mazzotti. *Energy Environ. Sci.*, **2022**, *15*, 3583-3602.

18. M. Wappler; D. Unguder; X. Lu; H. Ohlmeyer; H. Teschke*, et al. Int. J. Hydrogen Energy*, **2022**, *47*, 33551-33570.

19. Q. Li; A. Molina Villarino; C. R. Peltier; A. J. Macbeth; Y. Yang*, et al. J. Phys. Chem. C*, **2023**, *127*, 7901-7912.

20. H. Kojima; K. Nagasawa; N. Todoroki; Y. Ito; T. Matsui*, et al. Int. J. Hydrogen Energy*, **2023**, *48*, 4572-4593.

21. S. Jiao; X. Fu; S. Wang; Y. Zhao. *Energy Environ. Sci.*, **2021**, *14*, 1722-1770.

22. C. Deng; C. Y. Toe; X. Li; J. Tan; H. Yang*, et al. Adv. Energy Mater.*, **2022**, *12*, 2201047.

23. Z. Y. Yu; Y. Duan; X. Y. Feng; X. Yu; M. R. Gao*, et al. Adv Mater*, **2021**, *33*, e2007100.

24. O. Faye; J. Szpunar; U. Eduok. *Int. J. Hydrogen Energy*, **2022**, *47*, 13771-13802.

25. A. L. Hoang; S. Balakrishnan; A. Hodges; G. Tsekouras; A. Al-Musawi*, et al. Sustain Energy Fuels* **2023**, *7*, 31-60.

26. J. Yu; B.-Q. Li; C.-X. Zhao; Q. Zhang. *Energy Environ. Sci.*, **2020**, *13*, 3253-3268.

27. Y. Li; F. Liu; Z. Chen; L. Shi; Z. Zhang*, et al. Adv Mater*, **2022**, *34*, e2206002.

28. J. Zhang; W. He; T. Quast; J. R. C. Junqueira; S. Saddeler*, et al. Angew Chem Int Ed Engl*, **2023**, *62*, e202214830.

29. J. Li; H. Li; K. Fan; J. Y. Lee; W. Xie*, et al. Chem Catal.*, **2023**, *3*, 100638.

30. Q. Qian; X. He; Z. Li; Y. Chen; Y. Feng*, et al. Adv Mater*, **2023**, *35*, e2300935.

31. L. Zhu; J. Huang; G. Meng; T. Wu; C. Chen*, et al. Nat Commun*, **2023**, *14*, 1997.

32. Y. Zhu; C. Liu; S. Cui; Z. Lu; J. Ye*, et al. Adv Mater*, **2023**, *35*, e2301549.

33. M. Cai; Q. Zhu; X. Wang; Z. Shao; L. Yao*, et al. Adv Mater*, **2023**, *35*, e2209338.

34. J. Zhang; J. Zhu; L. Kang; Q. Zhang; L. Liu*, et al. Energy Environ. Sci.*, **2023**, *16*, 6015-6025.

35. J. Zhang; X. Song; L. Kang; J. Zhu; L. Liu*, et al. Chem Catal.*, **2022**, *2*, 3254-3270.

36. H. Lee; B. Choe; B. Lee; J. Gu; H.-S. Cho*, et al. J. Cleaner Prod.*, **2022**, *377*, 134210.

37. H. Liu; Y. Yang; J. Liu; M. Huang; K. Lao*, et al. ACS Appl Mater Interfaces*, **2024**, *16*, 16408-16417.

38. N. Elsayed; M. M. El-Rabiei; M. Negem; F. E.-T. Heakal. *Electrochim. Acta*, **2022**, *404*, 139783.

39. H. Tuysuz. *Acc Chem Res*, **2024**, *57*, 558-567.

40. D. Balun Kayan; E. Turunç. *Int. J. Energy Res.*, **2021**, *45*, 11146-11156.

41. J. Li; C. Zhang; T. Zhang; Z. Shen; Q. Zhou*, et al. Chem. Eng. J.*, **2020**, *397*, 125457.

42. X. Wang; H. Yao; C. Zhang; C. Li; K. Tong*, et al. Adv. Funct. Mater.*, **2023**, *33*, 230184.

43. H. Jiang; Y. Sun; B. You. *Acc Chem Res*, **2023**, *56*, 1421-1432.

44. A. H. Shah; C. Wan; Y. Huang; X. Duan. *J. Phys. Chem. C*, **2023**, *127*, 12841-12848.

45. S. Mathew; C. Y. Kim; M. K. Kim; K. C. Kim; W. S. Chung*, et al. ChemElectroChem*, **2021**, *8*, 2944-2949.

46. D. Chen; H. Bai; J. Zhu; C. Wu; H. Zhao*, et al. Adv. Energy Mater.*, **2023**, *13*, 2300499.

47. S. Shiva Kumar; H. Lim. *Energy Rep.*, **2022**, *8*, 13793-13813.

48. D. Likius; A. Rahman; C. Zivayi; V. Uahengo. *Catal. Lett.*, **2020**, *150*, 1942-1956.

49. J. Zhang; J. Dang; X. Zhu; J. Ma; M. Ouyang*, et al. Appl. Catal., B*, **2023**, *325*.

50. X. Li; L. Zhao; J. Yu; X. Liu; X. Zhang, *et al. Nanomicro Lett*, **2020**, *12*, 131.

51. Y. Liu; R. Zou; B. Qin; J. Gan; X. Peng. *Chem. Eng. J.*, **2022**, *446*, 136950.

52. R. Samanta; P. Panda; R. Mishra; S. Barman. *Energy & Fuels*, **2022**, *36*, 1015-1026.

53. H. Over. *ACS Catal.*, **2021**, *11*, 8848-8871.

54. W. Li; H. Zhang; M. Hong; L. Zhang; X. Feng, *et al. Chem. Eng. J.*, **2022**, *431*, 134072.

55. T. Wang; X. Cao; L. Jiao. *Angew Chem Int Ed Engl*, **2022**, *61*, e202213328.

56. S. Xu; X. Ruan; M. Ganesan; J. Wu; S. K. Ravi, *et al. Adv. Funct. Mater.*, **2024**, *34*, 2313309.

57. A. S. Rasal; H. M. Chen; W.-Y. Yu. *Nano Energy*, **2024**, *121*, 109183.

58. H. Liu; W. Shen; H. Jin; J. Xu; P. Xi, *et al. Angew Chem Int Ed Engl*, **2023**, *62*, e202311674.

59. A. Kumar; X. Liu; J. Lee; B. Debnath; A. R. Jadhav, *et al. Energy Environ. Sci.*, **2021**, *14*, 6494-6505.

60. I. El Gheriany; M. H. Abdel-Aziz; E.-S. Z. El-Ashtoukhy; G. H. Sedahmed. *Process Saf. Environ. Prot.*, **2022**, *159*, 133-145.

61. Z. Chen; W. Wei; B.-J. Ni. *Curr. Opin. Electrochem.*, **2022**, *31*, 100888.

62. Y. Song; K. Ji; H. Duan; M. Shao. *Exploration (Beijing)*, **2021**, *1*, 20210050.

63. Y. Ma; C. Ma; Y. Wang; K. Wang. *Catalysts*, **2022**, *12*, 337.

64. S. J. Yao; S. K. Wolfson; B. K. Ahn; C. C. Liu. *Nature*, **1973**, *241*, 471-472.

65. W. Simka; J. Piotrowski; G. Nawrat. *Electrochim. Acta*, **2007**, *52*, 5696-5703.

66. L. Wang; Y. Zhu; Y. Wen; S. Li; C. Cui, *et al. Angew Chem Int Ed Engl*, **2021**, *60*, 10577-10582.

67. B. K. Boggs; R. L. King; G. G. Botte. *Chem Commun (Camb)*, **2009**, 4859-4861.

68. R. Lin; L. Kang; T. Zhao; J. Feng; V. Celorrio, *et al. Energy Environ. Sci.*, **2022**, *15*, 2386-2396.

69. J. Li; S. Wang; S. Sun; X. Wu; B. Zhang*, et al. J. Mater. Chem. A*, **2022**, *10*, 9308-9326.

70. J. Bi; H. Ying; J. Hao; Z. Li. *Curr. Opin. Electrochem.*, **2022**, *33*, 100963.

71. X. Gao; S. Zhang; P. Wang; M. Jaroniec; Y. Zheng*, et al. Chem Soc Rev*, **2024**, *53*, 1552-1591.

72. X. Zheng; J. Yang; P. Li; Z. Jiang; P. Zhu*, et al. Angew Chem Int Ed Engl*, **2023**, *62*, e202217449.

73. D. Zhu; C. Guo; J. Liu; L. Wang; Y. Du*, et al. Chem Commun (Camb)*, **2017**, *53*, 10906-10909.

74. Y. Ding; Y. Li; Y. Xue; B. Miao; S. Li*, et al. Nanoscale*, **2019**, *11*, 1058-1064.

75. D. Liu; T. Liu; L. Zhang; F. Qu; G. Du*, et al. J. Mater. Chem. A*, **2017**, *5*, 3208-3213.

76. S. Hu; C. Feng; S. Wang; J. Liu; H. Wu*, et al. ACS Appl Mater Interfaces*, **2019**, *11*, 13168-13175.

77. Z.-Y. Yu; C.-C. Lang; M.-R. Gao; Y. Chen; Q.-Q. Fu*, et al. Energy Environ. Sci.*, **2018**, *11*, 1890-1897.

78. J. Xie; L. Gao; S. Cao; W. Liu; F. Lei*, et al. J. Mater. Chem. A*, **2019**, *7*, 13577-13584.

79. Y. Pan; K. Sun; Y. Lin; X. Cao; Y. Cheng*, et al. Nano Energy*, **2019**, *56*, 411-419.

80. L. Wang; L. Ren; X. Wang; X. Feng; J. Zhou*, et al. ACS Appl Mater Interfaces*, **2018**, *10*, 4750-4756.

81. C. Li; Y. Liu; Z. Zhuo; H. Ju; D. Li*, et al. Adv. Energy Mater.*, **2018**, *8*, 1801775.

82. T. Liu; D. Liu; F. Qu; D. Wang; L. Zhang*, et al. Adv. Energy Mater.*, **2017**, *7*, 1700020.

83. S. Chen; J. Duan; A. Vasileff; S. Z. Qiao. *Angew Chem Int Ed Engl*, **2016**, *55*, 3804-3808.

84. S.-K. Geng; Y. Zheng; S.-Q. Li; H. Su; X. Zhao*, et al. Nat. Energy*, **2021**, *6*, 904-912.

85. H. Jiang; J. Xia; L. Jiao; X. Meng; P. Wang*, et al. Appl. Catal., B*, **2022**, *310*, 121352.

86. V. M. Zemtsova; A. G. Oshchepkov; E. R. Savinova. *ACS Catal.*, **2023**, *13*, 13466-13473.

87. S. W. Tatarchuk; J. J. Medvedev; F. Li; Y. Tobolovskaya; A. Klinkova. *Angew Chem Int Ed Engl*, **2022**, *61*, e202209839.

88. J. Li; J. Li; T. Liu; L. Chen; Y. Li*, et al. Angew Chem Int Ed Engl*, **2021**, *60*, 26656-26662.

89. H. Sun; L. Li; H. C. Chen; D. Duan; M. Humayun*, et al. Sci Bull (Beijing)*, **2022**, *67*, 1763-1775.

90. J. Zhao; Y. Zhang; H. Guo; J. Ren; H. Zhang*, et al. Chem. Eng. J.*, **2022**, *433*, 134497.

91. F. Wang; K. Zhang; Q. Zha; Y. Ni. *J. Alloys Compd.*, **2022**, *899*, 163346.

92. M. Zhong; W. Li; C. Wang; X. Lu. *Appl. Surf. Sci.*, **2022**, *575*, 151708.

93. L. Hu; L. Jin; T. Zhang; J. Zhang; J. He*, et al. J Colloid Interface Sci*, **2022**, *614*, 337-344.

94. Y. Wang; N. Chen; X. Du; X. Han; X. Zhang. *J. Alloys Compd.*, **2022**, *893*, 162269.

95. R.-Q. Li; Q. Liu; Y. Zhou; M. Lu; J. Hou*, et al. J. Mater. Chem. A*, **2021**, *9*, 4159-4166.

96. Z. Wang; W. Liu; J. Bao; Y. Song; X. She*, et al. Chem. Eng. J.*, **2022**, *430*, 133100.

97. S. Feng; J. Luo; J. Li; Y. Yu; Z. Kang*, et al. Mater. Today Phys.*, **2022**, *23*, 100646.

98. H. Jiang; M. Sun; S. Wu; B. Huang; C. S. Lee*, et al. Adv. Funct. Mater.*, **2021**, *31*, 2104951.

99. L. Xia; Y. Liao; Y. Qing; H. Xu; Z. Gao*, et al. ACS Appl. Energy Mater.*, **2020**, *3*, 2996-3004.

100. X. Xu; X. Hou; P. Du; C. Zhang; S. Zhang*, et al. Nano Res.*, **2022**, *15*, 7124.

101. M. Maleki; G. Barati Darband; A. Sabour Rouhaghdam; R. Andaveh; Z. Mohammad Kazemi. *Chem Commun (Camb)*, **2022**, *58*, 3545-3548.

102. M. Li; H. Sun; J. Yang; M. Humayun; L. Li*, et al. Chem. Eng. J.*, **2022**, *430*, 132733.

103. Z. Wang; Y. Hu; W. Liu; L. Xu; M. Guan*, et al. Chemistry*, **2020**, *26*, 9382-9388.

104. J. Xie; H. Qu; F. Lei; X. Peng; W. Liu*, et al. J. Mater. Chem. A*, **2018**, *6*, 16121-16129.

105. S. A. Patil; N. K. Shrestha; H. T. Bui; V. D. Chavan; D. k. Kim*, et al. Int. J. Energy Res.*, **2022**, *46*, 8413-8423.

106. L. Yang; L. Zhang. *J Colloid Interface Sci*, **2022**, *607*, 546-555.

107. J. Cao; H. Li; R. Zhu; L. Ma; K. Zhou*, et al. J. Alloys Compd.*, **2020**, *844*, 155382.

108. L. Lei; Z. Yin; D. Huang; Y. Chen; S. Chen*, et al. J Colloid Interface Sci*, **2022**, *612*, 413-423.

109. Y. Liu; J. Guan; W. Chen; Y. Wu; S. Li*, et al. J. Alloys Compd.*, **2022**, *891*, 161790.

110. K. Wang; M. Hou; W. Huang; Q. Cao; Y. Zhao*, et al. J Colloid Interface Sci*, **2022**, *615*, 309-317.

111. Z. Ji; Y. Song; S. Zhao; Y. Li; J. Liu*, et al. ACS Catal.*, **2021**, *12*, 569-579.

112. J. Shen; Q. Li; W. Zhang; Z. Cai; L. Cui*, et al. J. Mater. Chem. A*, **2022**, *10*, 5442-5451.

113. K. Wang; W. Huang; Q. Cao; Y. Zhao; X. Sun*, et al. Chem. Eng. J.*, **2022**, *427*, 130865.

114. X. Du; G. Ma; X. Zhang. *Dalton Trans*, **2022**, *51*, 4909-4918.

115. J. Wu; J. Fan; S. Li; K. Cui; J. Wu*, et al. Mater. Sci. Eng. B.*, **2022**, *278*, 115654.

Chapter 2. Methodology

2.1 Materials characterization

X-ray diffraction (XRD) is an effective technique to gain basic information about the structure of the crystal. When X-rays irradiate the measured substance (crystal), the corresponding crystal plane will produce diffraction intensity. Different crystal planes at different angles are completely scanned. Thus the spectrum is presented according to the Bragg equation:

$$2d\sin\theta = n\lambda \tag{2.1}$$

λ represents the wavelength of the X-ray. d is the lattice distance of the crystal. θ is the angle of incidence.[1] The setup of XRD measurement involves X-ray sources and the monochromator. The sample and detector rotate to change the orientation and detect the diffracted X-ray.[2]

X-ray photoelectron spectrum (XPS) is a characterization method for surface analysis and valent state investigation. Based on the photoelectric effect, the photon is absorbed by an atom, resulting in ionization and the emission of inner shell electrons. By counting these ejected electrons and measuring the energy according to the equation:

$$E_b = h\nu - E_k - W \tag{2.2}$$

E_b, $h\nu$, E_k, and W represent the electron binding energy, energy of the incident X-ray, the kinetic energy of electrons, and the work function of the spectrometer, respectively.[3] The information of the surface (~ 10 nm), such as specific chemical composition and electronic state of those atoms can be thus revealed. The setup of XPS measurement involves a high vacuum system, monochromatic X-ray sources (Al Kα), electron lenses, a hemispherical analyzer, and a detector. Due to the common organic contamination, C 1s is used for calibration to mitigate the charging effect.[4]

The energy of X-rays can be divided into three ranges, including soft X-rays (0.1 keV - 2 keV), tender X-rays (2 keV - 6 keV), and hard X-rays (> 6 keV). X-ray absorption spectroscopy (XAS) is a useful technique to unearth the atomic configuration and electronic structure of the catalysts. The attenuation of X-ray is calculated by the equation: $I_t = I_0 e^{-\mu(E)d}$, where I_t, I_0, $\mu(E)$, and d represents the intensity of the incident and transmitted X-ray, the adsorption coefficient related to the energy of the incident radiation E, and the thickness of the sample.[5] When I_0 matches the binding energy of electrons in s orbitals, pre-edge features would be disclosed by exciting core-level electrons to the unoccupied orbitals, which can reflect the electronic geometry. When I_0 goes up into higher energy, the X-ray absorption near edge spectroscopy (XANES) or rising edge with a remark jump in the spectrum brought by the excited electrons going through the unoccupied states into the continuum state. Any shifts and features can be connected with the variation of oxidation state and geometric structure. The extended X-ray absorption fine structure (EXAFS) with oscillation in post-edge occurs due to the photoelectron scattering from a neighboring atom. Different from the XPS containing the electronic structure of the surface, EXAFS can provide more details about the local structure around a specific atom.[6]

Near edge X-ray absorption fine structures (NEXAFS) in the range of soft X-rays can be used to figure out the electron structure *via* exciting the core electron to the unoccupied orbitals for the K-edges elements from Li to Si. Due to the dipole-allowed 2p - 3d electron transition (L-edge), the valence states for 3d transitional metals could also be revealed, which can offer more details to supplement their K-edge spectra.[7]

Based on the interactions between electron magnetic waves with molecules, Raman spectroscopy involves inelastic scattering of light, which can be used to detect the intermediates and evolution of catalysts. A laser beam hits the molecular and leads to light bouncing back with various energies. The molecule’s polarizability is measured. Specifically, *in situ* Raman characterization shows superiority in reflecting the situations of reaction microenvironments in real-time.[8]

Ultraviolet light-visible (UV-vis) measurement is often used to analyze the discrepancy of the electrolyte before and after reactions. When the molecule absorbs UV light of a certain wavelength, the valence electrons transit from a low energy level to a high energy level. The maximum absorbance of a substance is reflected with a certain wavelength. The absorbance is proportional to the concentration according to the Lambert Beer's Law:

$$\text{Absorbance} = e\ c\ d \tag{2.3}$$

The e is the absorption coefficient. The c is the concentration of absorbing samples. d is the thickness of the absorbing samples.[9]

Microwave plasma atomic emission spectroscopy (MP-AES) is widely used to detect the amount of the chemical composition. When the atoms return from an excited electronic state to the ground state, electromagnetic radiation is emitted with a characteristic pattern. The intensity of the emitted radiation can reflect the concentration of the atoms in the sample. MP-AES measurement involves nitrogen plasma to atomize the samples and excite the atoms for energy transition. The emitted radiation travels to the monochromator to generate individual wavelengths, which is followed by identification and quantification by a detector.[10]

Scanning electron microscope (SEM) is often used to confirm the morphology of materials by measuring the interaction between a beam of electrons and materials. Secondary electrons, from the outer layer of the atoms, were collected due to their sensitivity to the morphology. Energy dispersive X-ray spectroscopy (EDS) is employed to qualitatively and quantitatively analyze elemental compositions.[11] Different from the SEM, the internal structure can be presented by transition electron microscopy (TEM) by collecting the electrons that go through the specimen.[12] To observe at an atomic scale, high-angle annular dark-field-scanning transmission electron microscopy (HADDF-STEM) is usually used to achieve ultra-high resolution. Abbrreation-corrected instruments and high-angle annular dark field detectors are equipped to realize the atomic resolution.[13]

2.2 Electrochemical performance

As common methods with a certain applied voltage range, cyclic voltammetry (CV) and linear scanning voltammetry (LSV) are carried out in a three-electrode cell to evaluate the UOR catalysts. The long-term stability test is usually operated to examine the sustainability of activity via methods of chronoamperometry (CA, time-current curve) and chronopotentiometry (CP, time-potential curve). Electrochemically active surface area (ECSA) is proportional to the double-layer capacitance (C_{dl}), which is often calculated to appraise the activity of catalysts according to the equation: ECSA $= \frac{C_{dl}}{Cs}$, where Cs represents the specific capacitance of the materials. The Tafel plot is usually gained by replotting the polarization curve (Y-axis: potential, X-axis: log|current density|). The Tafel slope is thus obtained from a linear fitting plot of the Tafel plot, which can reflect the activity of the catalysts. The smaller the Tafel slope is, the higher the active the catalyst is.

Electrochemical impedance spectroscopy (EIS) is also an effective technique to assess the charge transfer resistance and solution resistance. The IR compensation (I: current flowing through the system; R: resistance) is usually conducted to exclude the solution resistance effect.[14] The solution resistance can be gained from the intersection between the Nyquist curve and the X-axis. *In situ* EIS can also be used to reveal the situation of the reaction interface. For example, as for Ni-based OER catalysts, it has been demonstrated that surface oxidation proceeds at the high-frequency interface, and OER undergoes at the low-frequency interface.

2.3 Wetting ability evaluation

With the development of bionic technology for achieving super-wetting properties surface, the (super)hydrophobic and (super)hydrophilic functional surfaces have been extensively employed for surface cleaning, oil/water separation, water droplet manipulation, and fog harvesting. The super-wetting electrodes have recently drawn attention to solving the bottleneck issues in electrochemical studies and applications. The suitable wetting properties should be first confirmed to regulate the reaction microenvironment involving the adsorption and desorption process towards reactants and intermediates. It has been verified that regulating wetting properties at the solid-water-gas phase interface can be a promising route to elevate mass transfer and stabilize intermediates.[15]

The surface morphology with tunable rough structures is an effective tool to modify the wetting properties. Incorporating varying micro-nano structures to modulate the wetting properties of electrodes has been extensively applied to empower the reaction rate for electrochemical applications. The desirable catalytic process relies on the well-designed pathways for electrons, ions, and generated or consumed gas substances. Those contributing factors would be subtly customized in terms of electrode, and electrolyte to elevate the catalytic performance.[16]

By learning from nature, such as the antifouling lotus effect and drag-reducing properties of fish scales, developing unique micro-nano architectures to obtain suitable wetting properties for gas-involved reactions can regulate the behaviors of generated or consumed gas bubbles during the electrocatalytic process. For example, the superhydrophilic-superaerophobic surface possesses a contact angle of the water (WCA) $< 10°$ and a contact angle of bubble (BCA) $> 150°$. The discontinuous contact line between solid-liquid-gas phases can accelerate the gas-releasing from the electrode surface. The lower adhesion of gas bubbles would enable reduced bubble resistance for electron transfer at the interface. Therefore, as for the reactions with gas products such as HER, OER, and UOR, superhydrophilic surfaces can enable close contact between electrolyte and electrode. Superaerophobic surfaces can enable the rapid release of gas bubbles to refresh the interface immediately.[17]

Additionally, superhydrophobic-superaerophilic surface with WCA $> 150°$ and BCA $< 10°$ is more favorable for gas-consumed reactions such as carbon dioxides reduction reaction (CO_2RR). This is due to the rapid gas diffusion process that enables the abundant gas reactants to spread on the catalytic layer. Meanwhile, superhydrophobic properties can decrease the water activity to inhibit HER.[18]

The contact lines of the solid-water-gas phase can be described with Young’s equation under ideal conditions with a smooth surface (Equation 2.4) to confirm the hydrophilicity and hydrophobicity. Identically, using “gas bubbles” to replace “liquid droplets” can illustrate the aerophobicity and aerophilicity of bubbles underwater. The model can be modified as shown in Equation 2.5.

$$\gamma_{SG} = \gamma_{SL} + \gamma_{LG} \cos\theta \tag{2.4}$$

$$\gamma_{SL} = \gamma_{SG} + \gamma_{LG} \cos\alpha \tag{2.5}$$

Where γ_{SG}, γ_{SL} and γ_{LG} are the interface tension of solid-gas, solid-liquid, and liquid-gas, respectively. θ and α are the intrinsic contact angles of the materials.

Moreover, the Wenzel equation and Cassie-Baxter equation are further proposed (Equation 2.6 and 2.7) to identify superaerophilicity and superaerophobicity when considering the practical situations of the surface with the micro-nano rough structures.

$$\cos\alpha^* = r\cos\alpha \tag{2.6}$$

$$\cos\alpha^* = -1 + f_S(\cos\alpha + 1) \tag{2.7}$$

Where α is the apparent contact angle, α^* is the apparent contact angle on the structured surface, r is the factor of surface roughness, and f_S is the solid fraction of the interface.

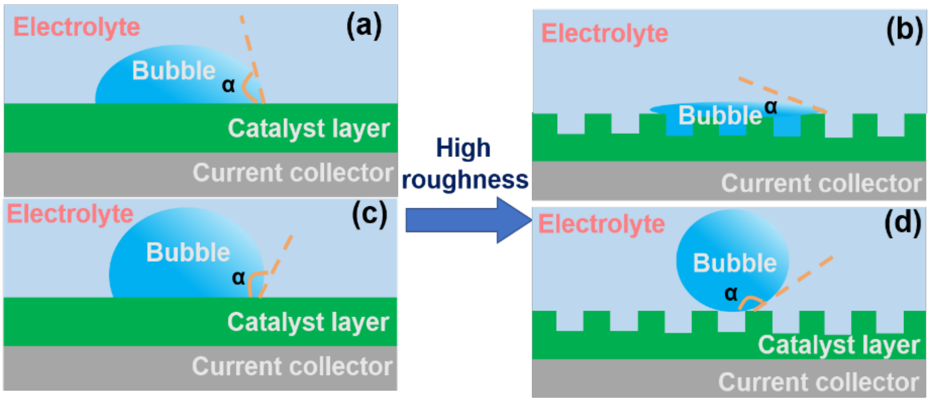

Figure 2.1. Schematic illustration of aerophilic and aerophobic properties with and without micro-nano structures.

As shown in Figure 2.1 a and b, the intrinsic aerophilic substrate can exhibit more gas bubble-affinities after incorporating high roughness with micro-nano structures. When immersing superhydrophobic surfaces in aqueous media, the liquid would be expelled due to water-proof properties. The bursting state with BCA close to 0° could be presented and the spreading of the gas reactant on the surface can ensure a continuous and abundant supply for consumption. Therefore, superaerophilic property is conducive to gas-consumption reactions.

As shown in Figure 2.1 c and d, the intrinsic aerophobic surface can be more gas bubble-aversion after incorporating high roughness with micro-nano structures. When immersing superhydrophilic surfaces in aqueous media, the liquid would go into the rough structures, thus hindering the gas bubble from further getting in. The low adhesion between the generated gas bubble and the surface can ensure the rapid gas release to refresh the interface immediately. Therefore, superaerophobic property with BCA > 150° is desirable for gas-evolution reactions.

As mentioned above, the UOR process proceeds in aqueous electrolyte and involves gas product formation, thus leveraging superhydrophilic-superaerophobic properties with high roughness structures can optimize the reaction microenvironments during the UOR process to obtain the well-designed pathways for electrons, ions, and generated gas substances.[19]

2.4 Reference

1. H. Khan; A. S. Yerramilli; A. D'Oliveira; T. L. Alford; D. C. Boffito*, et al. Can. J. Chem. Eng.*, **2020**, *98*, 1255-1266.

2. G. Surekha; K. V. Krishnaiah; N. Ravi; R. Padma Suvarna. *J. Phys. Conf. Ser.*, **2020**, *1495*, 012012.

3. D. N. G. Krishna; J. Philip. *Appl. Surf. Sci. Adv.*, **2022**, *12*, 100332.

4. M. A. Isaacs; J. Davies-Jones; P. R. Davies; S. Guan; R. Lee*, et al. Mater. Chem. Front.*, **2021**, *5*, 7931-7963.

5. L. Fang; S. Seifert; R. E. Winans; T. Li. *Small*, **2022**, *18*, e2106017.

6. D. Eggart; X. Huang; A. Zimina; J. Yang; Y. Pan*, et al. ACS Catal.*, **2022**, *12*, 3897-3908.

7. N. Diklić; A. H. Clark; J. Herranz; J. S. Diercks; D. Aegerter*, et al. ACS Energy Lett.*, **2022**, *7*, 1735-1740.

8. Y. Qi; D. Hu; Y. Jiang; Z. Wu; M. Zheng*, et al. Adv. Opt. Mater.*, **2023**, *11*, 2203104.

9. C. Liao; M. Zhu; D. E. Jiang; X. Li. *Chem Sci*, **2023**, *14*, 4666-4671.

10. V. Balaram. *Microchem. J.*, **2020**, *159*, 105483.

11. Y. Sargam; K. Wang. *Cem. Concr. Res.*, **2021**, *147*, 106524.

12. J. Cui; H. Zheng; K. He. *Adv Mater*, **2021**, *33*, e2000699.

13. H. Liu; H. Qin; J. Kang; L. Ma; G. Chen*, et al. Chem. Eng. J.*, **2022**, *435*, 134898.

14. H. Duan; C. Wang; R. Yu; W. Li; J. Fu*, et al. Adv. Energy Mater.*, **2023**, *13*, 2300815.

15. W. Xu; Z. Lu; X. Sun; L. Jiang; X. Duan. *Acc Chem Res*, **2018**, *51*, 1590-1598.

16. D. Zhou; P. Li; X. Lin; A. McKinley; Y. Kuang*, et al. Chem Soc Rev*, **2021**, *50*, 8790-8817.

17. X. Shan; J. Liu; H. Mu; Y. Xiao; B. Mei*, et al. Angew Chem Int Ed Engl*, **2020**, *59*, 1659-1665.

18. G. Liu; W. S. Y. Wong; M. Kraft; J. W. Ager; D. Vollmer*, et al. Chem Soc Rev*, **2021**, *50*, 10674-10699.

19. T. H. Shen; L. Spillane; J. Peng; Y. Shao-Horn; V. Tileli. *Nat Catal*, **2022**, *5*, 30-36.

Chapter 3. Non-noble metal doped Ni catalysts

3.1 Acknowledgement

I acknowledged Xuedan Song and Qing Zhang for the DFT calculations and analysis as well as the help from Liqun Kang and Longxiang Liu about the XAS spectrum analysis. Besides, I also acknowledged Jiexin Zhu, Dan J.L. Brett, Paul R. Shearing, Liqiang Mai, Ivan P. Parkin, Guanjie He for their useful suggestion. The work described in this chapter was published in the journal of Chem Catalysis (DOI: 10.1016/j.checat.2022.09.023) and I was the first author. The contents including the images reproduced from this paper were with permission from the publisher, Elsevier.

3.2 Introduction

The wide application of water electrolysis is mainly impeded by the large overpotential of the OER catalysts.[1-3] UOR has been verified as a promising route to replace OER and realize the urea-bearing water treatment.[4-7] A relatively lower theoretical potential of 0.37 V *vs.* RHE and sufficient sources from human urine can enable UOR as the competitive choice among other small molecular oxidation such as methanol and ethanol oxidation reactions (MOR and EOR).[8]

The alkaline UOR process encompasses multifarious and sophisticated C or N-intermediates adsorption and desorption. Moreover, numerous electron transfer steps further result in high overpotential. To replace the noble metal-based catalysts due to their expensive price and the limited amount of access, the exploration of suitable non-noble metal-based catalysts draws attention among the research community.[9-11]

The Ni-based materials, as extensively employed UOR electrocatalysts, can generate high NiOOH active sites during the electrochemical step for urea dehydrogenation.[12] Ni hydroxides are usually leveraged to be proof-of-concept to explore the reaction microenvironment during the UOR process due to their well-defined layer structures.[13] Additionally, the high valence transition metals with partially filled d orbital electrons exhibit the potential to stabilize the intermediates and regulate the electronic structure of active sites. Therefore, incorporating the heteroatom doping strategy to modify the Ni hydroxides is considered an effective route to elevate electrochemical performance during the UOR process.[14]

Despite the numerous studies focusing on introducing high valence transition metals to modify the electronic structure,[15-17] UOR performance still requires to be improved. Additionally, dopants can leach into electrolytes during surface oxidation processes according to the Pourbaix diagram. This is often overlooked in investigating the stability issues of dopant structure (Figure 3.1 a), thus leading to uncontrollable structure reconstruction and undesirable collapse of bulk structures. The altered physicochemical properties at the electrochemical interface can also lead to difficulties in mechanism exploration or even achieving an unreliable reaction mechanism.[18] Therefore, the *in situ* characterization method is also required to disclose the dopant leaching process within a wide range of applied potentials.

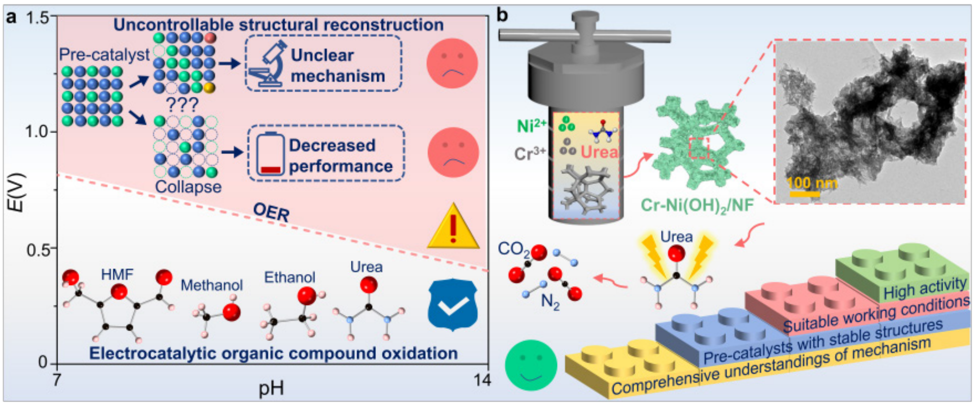

Figure 3.1. (a) Issues of small molecule oxidation reactions in the alkaline electrolytes. (b) Schematic illustration of the $Cr-Ni(OH)_2$ electrocatalysts synthesis and its highlights for UOR.

In this chapter, $Cr-Ni(OH)_2$ electrocatalyst was synthesized via the hydrothermal method (Figure 3.1 b). The co-precipitation of Ni and Cr precursors under alkaline media could lead to the formation of hydroxide with micro-nano structures, thus resulting in superhdrophilic-superaerophobic properties to achieve suitable pathways for electrons, ions, and generated gas substances. Moreover, according to the results of *in situ* Raman measurement combined with DFT calculations, Cr dopants can effectively elevate UOR performance with a desirable electrochemical interface, involving accelerated mass and electron transfer. The urea molecules would preferentially adsorb on the surface to inhibit the Cr leaching to form chromate anion. The investigation of the Cr leaching process at the electrochemical interface opens a new avenue for the exploration of stability issues of dopant structure, inspiring the subsequent design of Ni-based UOR catalysts and other small molecule oxidation reactions.

3.3 Experimental Section

3.3.1 Synthesis of Cr-$Ni(OH)_2$ catalysts

The Cr-$Ni(OH)_2$ electrocatalyst was synthesized *via* a facile hydrothermal method. Briefly, the Ni and Cr precursors were 1 mmol $Ni(NO_3)_2{\cdot}6H_2O$ and 0.25 mmol $Cr(NO_3)_3{\cdot}9H_2O$, respectively. 0.2 g urea was further leveraged to create an alkaline condition during the hydrothermal process. The above chemical reagents were subsequently dissolved in 25 mL of deionized water (DIW). Pre-cleaned NF (4 cm x 2 cm, thickness of 1 mm) was placed in a Teflon-lined stainless-steel autoclave and the above solution was then added to immerse the NF. The temperature and hydrothermal time were 120 °C and 12 hours respectively.

The Cr-$Ni(OH)_2$ electrocatalysts were finally obtained after cleaning and drying at 60 °C for 10 h. The powder samples were obtained from centrifugation of the precipitates and freeze-drying processes. The Cr-$Ni(OH)_2$ catalyst with different feed ratios of Cr was synthesized with a similar process. As for $Ni(OH)_2$ catalyst without Cr, the $Cr(NO_3)_3{\cdot}9H_2O$ was not added. The mass loading was calculated by analyzing the weight before and after synthesis.

3.3.2 Characterizations

XPS, Thermo scientific K-alpha photoelectron spectrometer, was used to analyze the chemical composition. The 284.8 eV for C 1s was first used for calibration before estimating the chemical states. XRD patterns were collected by STOE SEIFERT diffractometer with the radiation of the Mo source. The morphology and microstructures of samples were evaluated with scanning electron microscope (SEM, JEOL LSM 6701) and transmission electron microscope (JEOL, JEM-2100).

The FTA1000B drop-shape analyzer was used to analyze the contact angle. UV-vis spectra were collected from Shimadzu UV 2600 to estimate the electrolyte composition of chromate after the UOR and OER process. *In situ* spectroscopic studies of Raman measurement were performed to reveal the reaction microenvironment during the UOR and OER process. The laser wavelength of 532 nm (DXR Raman Microscope) and the cell for the Raman test (Beijing Science Star Technology Co., Ltd, China) were used.

As for the XAS test, the ink containing 1mg Cr-Ni(OH)$_2$ catalyst, 200 μL ethanol, 100 μL DI water, and 10 μL 5%wt Nafion solution was dropped on the pre-cleaned carbon paper (CP) and dried in air. The Cr-Ni(OH)$_2$/CP was used for XAS measurement to exclude the effect of Ni substrate. The NEXAFS study was performed at the B07-B beamline at the Diamond Light Source. The incident beam was sourced from a bending magnet and monochromatized *via* a plane grating monochromator (PGM). The beam spot size at the sample position was approx. 200 μm × 200 μm (H×V). During this commissioning beamtime, the ultra-high vacuum system for pumping the specimen chamber was not in full operation. Therefore, the NEXAFS spectra were collected at 1.0×10^{-6} mbar in Helium under room temperature, and the signal-to-noise ratio was slightly compromised. NEXAFS spectra at $L_{3,2}$-edge of Cr and Ni were acquired in total electron yield (TEY) mode with the ES-2 endstation (designed for ambient pressure NEXAFS measurement). The energy range for Cr $L_{3,2}$-edge and Ni $L_{3,2}$-edge were 570-605 eV and 845-885 eV, respectively. The scan step was set to 0.1 eV for both Cr and Ni. Four samples were investigated in total, including fresh Ni(OH)$_2$ catalyst, fresh Cr-Ni(OH)$_2$ catalyst, Cr-Ni(OH)$_2$ catalyst after OER, and Cr-Ni(OH)$_2$ catalyst after UOR. In addition, commercial Ni(OH)$_2$, NiO, Cr_2O_3, and K_2CrO_4 were measured as reference materials. The catalyst powder and reference materials were dispersed on indium film by pressing, which enabled good conductivity while preventing sample contamination. For each sample at each absorption edge, three to five scans were collected and merged to improve the overall signal-to-noise ratio. NEXAFS spectra were analyzed using the *xraylarch* package (version 0.9.58) for energy calibration, background subtraction, and normalization. Cr K-edge and Ni K-edge were collected at the B18 beamline of Diamond Light Source during a Blocked Allocation Group (BAG) beamtime for UK CatalysisHub (proposal number: SP29271). A fast-scanning Si (111) double crystal monochromator (DCM) was used to perform XAFS measurement in QEXAFS mode. A couple of Pt-coated harmonic rejection mirrors were inserted to suppress the high-order harmonics. Four catalysts supported on carbon paper (as working electrodes) were measured, including fresh $Ni(OH)_2$ catalyst, fresh Cr-$Ni(OH)_2$ catalyst, Cr-$Ni(OH)_2$ catalyst after UOR, and Cr-$Ni(OH)_2$ catalyst after OER. Due to the relatively lower concentration of Cr than Ni in these samples, the Cr K-edge XAFS spectra were acquired in fluorescence mode using 36-element Ge solid-state detector, while the Ni K-edge XAFS spectra were collected in transmission mode through ionization chambers. In addition, four reference samples including commercial NiO, $Ni(OH)_2$, Cr_2O_3, and K_2CrO_4 were measured in transmission mode (diluted by boron nitride and pressed into an 8 mm diameter pellet). Three scans of each sample at each absorption edge were acquired and merged to improve the signal-to-noise ratio. The XAFS scan energy range was 5789-6839 eV (step size = 0.25 eV, k_{max} = 14.9) for Cr K-edge and 8133-9833 eV (step size = 0.25 eV, k_{max} = 14.8) for Ni K-edge respectively. XAFS spectra of standard samples NiOOH, Ni_2O_3, and $Cr(OH)_3$ are retrieved from the Spring-8 BL14B2 XAFS database. XAFS data were analyzed using the Demeter software package. The Athena software was used to calibrate the energy, subtract the background, and normalize the EXAFS spectrum. Energy calibration of Cr K-edge XAFS was realized by shifting the maximum in the first derivative of the Cr foil XANES spectrum to 5989 eV, corresponding to the absorption edge position of metallic chromium. Similarly, Ni K-edge XAFS was calibrated by shifting the absorption edge of Ni foil XANES to 8333 eV. The k^2-weighted $\chi(k)$ data were Fourier transformed (FT) to R space using a Hanning window function ($3 < k < 12.5$, $\Delta k = 1$). The FT k^2-weighted R-space EXAFS spectra were fitted using Artemis software ($1 < R < 3.3$). The amplitude reduction factor for Cr K-edge EXAFS was calculated to be 0.67 through the fitting of the Cr foil EXAFS spectrum, and this value was employed as a constant for the EXAFS fitting of all the Cr K-edge EXAFS. The amplitude reduction factor for Ni K-edge EXAFS was determined to be 0.9 based on Ni foil through the same protocol.

3.3.3 Electrochemical measurement

An electrochemical cell configuration was used to evaluate the UOR performance. 1 M KOH solution with and without 0.33 M urea was utilized as the electrolyte for UOR and OER respectively. The Cr-$Ni(OH)_2$ catalyst on NF was employed as the working electrode. The carbon rod was used as the counter electrode. As for the reference electrode, an Ag/AgCl electrode filled with saturated KCl solution was used.

Potentiostat (Gamry Interface 1000) was used to set up varying electrochemical test modes. Cyclic voltammetry (CV) was performed to observe the oxidation and reduction peaks. The linear sweep voltammetry (LSV) was carried out at a scan rate of 5 mV s^{-1} to estimate the potential. The potential conversion was operated according to $E_{RHE} = E_{Ag/AgCl} + 0.197 + 0.059\ pH$. The Tafel plot was gained by replotting the polarization curve (Y-axis: potential, X-axis: log|current density|). The Tafel slope was thus obtained from a linear fitting of the Tafel plot.

A chronopotentiometry test with a constant current density was performed to observe the performance degradation over the long-term operation. LSV measurements were presented with IR compensation. The CV within a non-Faradaic potential from 0.02 - 0.12 V *vs.* Ag/AgCl was performed to measure the electrochemical double-layer capacitance (C_{dl}), which is a positive correlation to the electrochemically active surface area (ECSA).

3.3.4 DFT calculation

The DFT calculations were carried out by the software of Vienna ab initio simulation package (VASP) with the projector augmented wave (PAW) pseudopotential. The exchange and correlation interactions were presented by Generalized gradient approximation (GGA) of Perdew-Burke-Ernzerhof (PBE) functional. The empirical correction of the Grimme's scheme (DFT-D3), the cut-off energies of 500 eV, and the *k*-point grid of 3×3×1 were used for all calculations.

The adsorption energy (E_{ads}) was obtained by the equation as follows:

$$E_{ads} = E_{adsorbate/sub} - (E_{adsorbate} + E_{sub})$$

where $E_{adsorbate/sub}$, $E_{adsorbate}$, and E_{sub} denote the total energies for the adsorbate with the substrate, the isolated adsorbate, and the clean substrate, respectively.

3.4 Results and Discussion

3.4.1 Cr-Ni(OH)$_2$ catalysts

The Cr-Ni(OH)$_2$ catalyst was first fabricated on NF by a facile hydrothermal method. The TEM image presented the lattice fringes of (101), (015), and (018) facets of α-Ni(OH)$_2$ (Figure 3.2a). The EDS mapping was performed to unearth the distribution of elements of Ni, O, and Cr (Figure 3.2b). XRD patterns (Figure 3.3) and Raman spectra (Figure 3.4) were further collected to analyze the crystal phase.

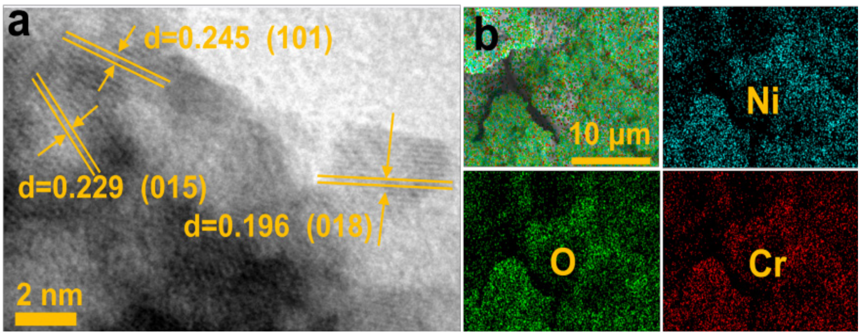

Figure 3.2. Morphologies of Cr-Ni(OH)$_2$. (a) HRTEM images and corresponding lattice spacings. (b) SEM-EDS results of Cr-Ni(OH)$_2$: Ni (cyan), O (green), Cr (red).

The single phase of α-Ni(OH)$_2$ is well-identified according to PDF card No. 38-0715. As compared to the sample without Cr, the intensity of the single phase of α-Ni(OH)$_2$, especially at the low angle range of 2θ, exhibits a significantly weaker signal, which might be attributed to structural defects of $Ni(OH)_2$ brought by Cr incorporation. To further characterize structural defects in Cr-$Ni(OH)_2$, Raman spectra were collected. The peak at ~ 460 cm^{-1} can be identified as the lattice vibration of $Ni(OH)_2$.[19] The Ni-O vibration peaks of structural defects in $Ni(OH)_2$ are found at ~ 490 and 536 cm^{-1}.[20] The peak at ~ 548 cm^{-1} is ascribed to Cr-O vibration mode of Cr_2O_3.[21] Therefore, it could be discovered that Cr dopants could lead to structural defects formation on $Ni(OH)_2$ substrates.

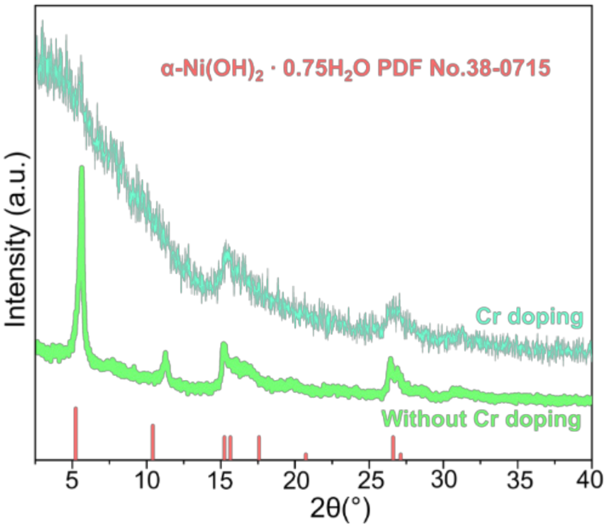

Figure 3.3. XRD pattern of $Ni(OH)_2$ with and without Cr.

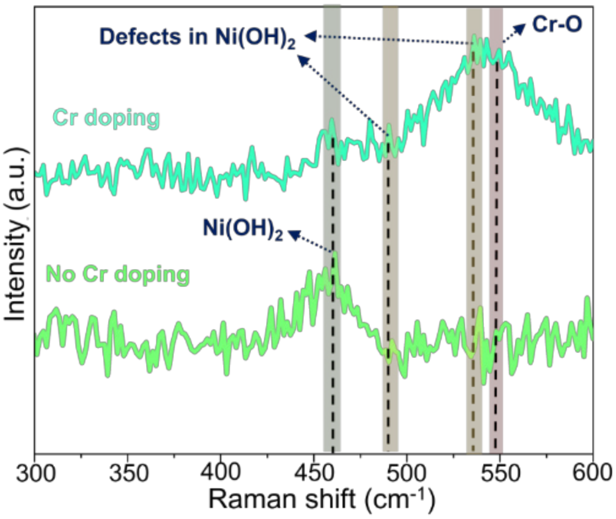

Figure 3.4. Raman spectra of $Ni(OH)_2$ with and without Cr.

To confirm the metal contents of prepared catalysts, the loading masses of as-prepared samples with varying molar ratios of Ni and Cr, including Ni_1Cr_1,

$Ni_1Cr_{0.5}$, $Ni_1Cr_{0.25}$, and $Ni_1Cr_{0.125}$, were calculated by differences of mass before and after synthesis (Figure 3.5). The loading mass of Ni_1Cr_1, $Ni_1Cr_{0.5}$, $Ni_1Cr_{0.25}$, and $Ni_1Cr_{0.125}$ were 7.5, 3.2, 1.7, and 1.1 mg cm^{-2}, respectively. The XRD patterns of Ni_1Cr_1, $Ni_1Cr_{0.5}$, and $Ni_1Cr_{0.125}$ (Figure 3.6) were further collected. The single phase of α-$Ni(OH)_2$ with structural defects could be found.

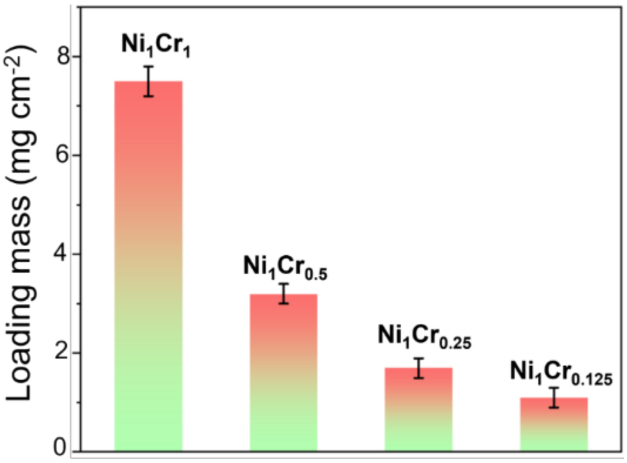

Figure 3.5. Loading mass of different molar ratios of Ni and Cr.

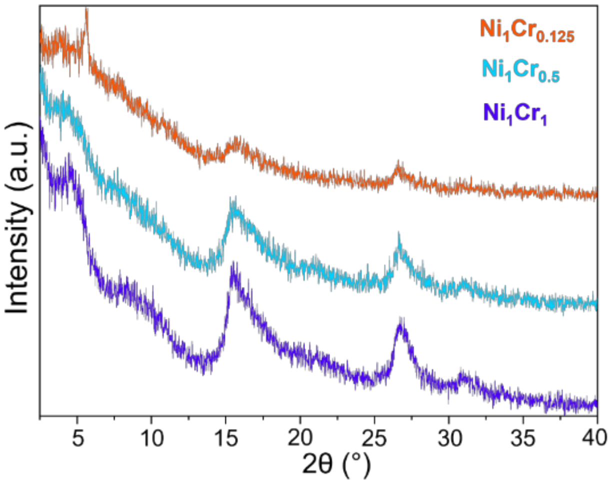

Figure 3.6. XRD pattern of other molar ratios of Ni and Cr.

Furthermore, the electronic and geometric structures of as-prepared electrocatalysts were unveiled by NEXAFS and XAFS. Ni $L_{3,2}$-edge spectra from NEXAFS presented features of high-spin Ni (II) in an octahedral geometry for Ni hydroxide with and without Cr doping (Figure 3.7 a). The absorption peak at 856.5 eV and ~858.2 eV corresponded to dipole-allowed electron transition from Ni $2p_{3/2}$ to Ni 3d e_g orbitals.

According to Ni K-edge spectra from XANES for Ni hydroxide with and without Cr doping, the pre-edge energy position of $Ni(OH)_2$ and Cr-$Ni(OH)_2$ located at 8333.5 eV was in line with commercial NiO and $Ni(OH)_2$ with Ni (II) valence state. The pre-edge energy positions situated at 8334.6 eV and 8335.0 eV corresponded to Ni_2O_3 and NiOOH with Ni (III) valence state, respectively (Figure 3.8 a).

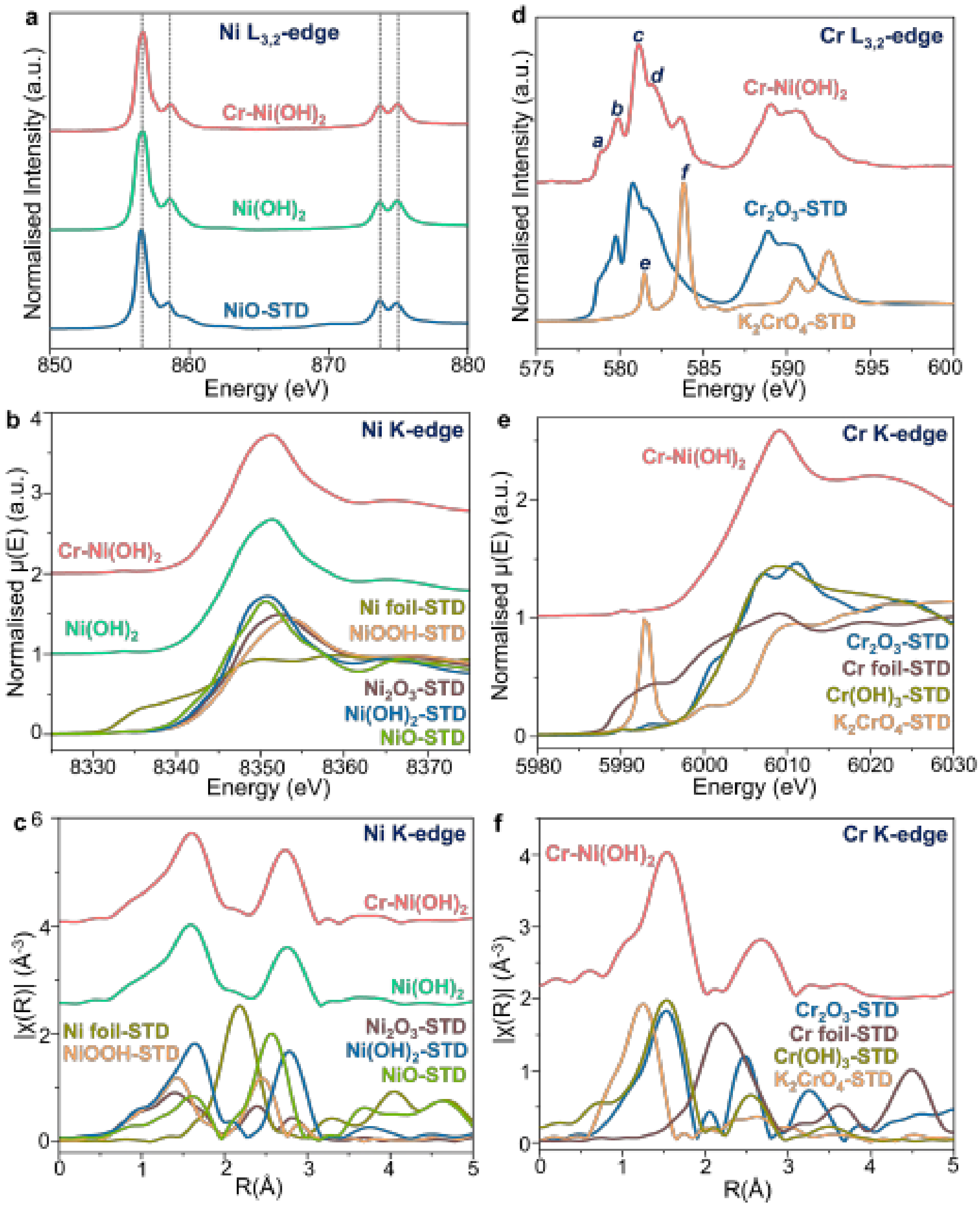

Figure 3.7. (a) Ni $L_{3,2}$-edge from NEXAFS. (b) Ni K-edge from XANES. (c) Ni K-edge from EXAFS. (d) Cr $L_{3,2}$-edge from NEXAFS. (e) Cr K-edge from XANES. (f) Cr K-edge from EXAFS.

Meanwhile, the energy position from the main absorption edge of Ni hydroxide with and without Cr doping was also lower than that of the Ni_2O_3 and NiOOH with Ni (III) valence state (Figure 3.7 b). This finding matched with the Ni L-edge spectra from NEXAFS, indicating that the dominant Ni species was Ni (II) for $Ni(OH)_2$ and $Cr\text{-}Ni(OH)_2$ catalysts.

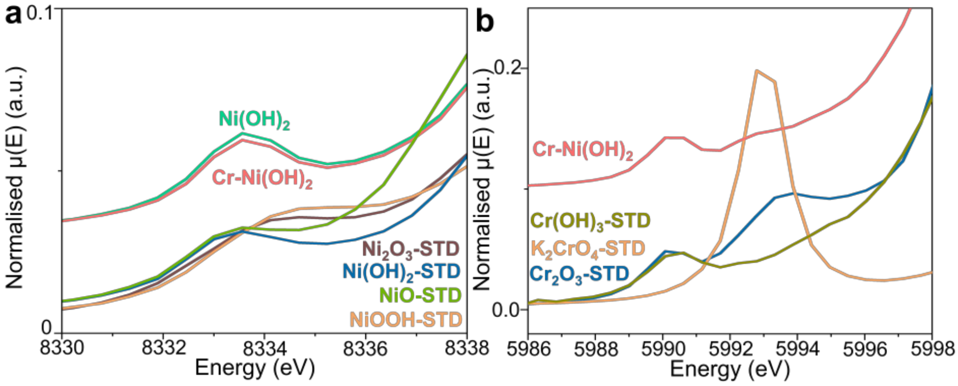

Figure 3.8. The pre-edge of XANES Ni K-edge (a) and Cr K-edge (b).

The coordination configuration of Ni species in Ni hydroxide with and without Cr doping was disclosed by fitting Fourier Transformed EXAFS spectra (FT-EXAFS) (Figure 3.7 c and 3.9).

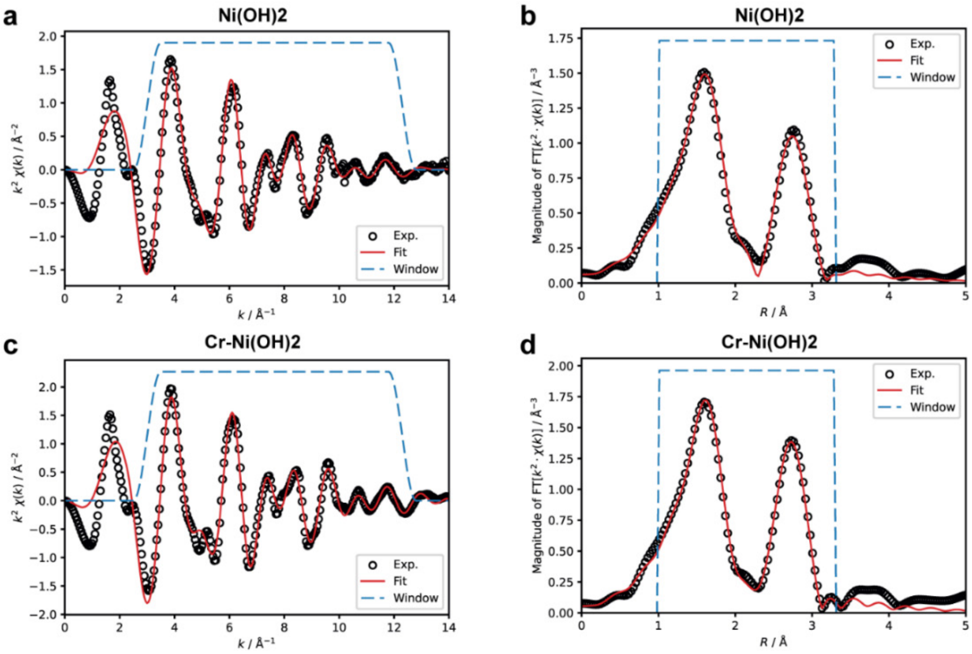

Figure 3.9. EXAFS fitting. (a)-(b) The fitting analysis of Ni K-edged EXAFS measurement of $Ni(OH)_2$. (c)-(d) Ni K-edged EXAFS measurement of $Cr\text{-}Ni(OH)_2$.

According to the fitting results of FT-EXAFS spectra of the $Ni(OH)_2$ and $Cr-Ni(OH)_2$ catalysts, no notable variance in the coordination configuration between Ni hydroxide with and without Cr doping could be found. As shown in Table 3.1, it could be discovered that the first shell of 6-coordinated Ni-O and a second shell of 6-coordinated Ni-Ni/Cr possessed almost identical interatomic distances (Ni-O: 2.06 ± 0.01 Å and Ni-Ni/Cr: 3.09 ± 0.01 Å).

Table 3.1. Fitting results of Ni K-edge EXAFS.

Sample	Scattering Path	C.N.	R(Å)
$Ni(OH)_2$	Ni-O	5.8 ± 0.5	2.04 ± 0.01
	Ni-Ni	6.2 ± 1.1	3.10 ± 0.01
$Cr-Ni(OH)_2$	Ni-O	6.2 ± 0.3	2.06 ± 0.01
	Ni-Cr/Ni	6.2 ± 0.7	3.09 ± 0.01
$Cr-Ni(OH)_2$-OER	Ni-O	6.0 ± 0.6	2.05 ± 0.01
	Ni-Cr/Ni	6.3 ± 1.4	3.08 ± 0.01
$Cr-Ni(OH)_2$-UOR	Ni-O	6.2 ± 0.3	2.05 ± 0.01
	Ni-Cr/Ni	5.8 ± 0.8	3.08±0.01

C.N. = coordination number; R = interatomic distance.

The Cr $L_{3,2}$-edge and K-edge for Ni hydroxide with Cr doping were subsequently unearthed by NEXAFS and XAFS to investigate the electronic structures and geometric structures. As compared to high-spin octahedrally coordinated Cr (III) and tetrahedrally coordinated Cr (VI) of the reference samples including Cr_2O_3 and K_2CrO_4, the Cr $L_{3,2}$-edge spectra of $Cr-Ni(OH)_2$ catalysts possessed four peaks from a-d as shown in Figure 3.7 d. The peaks a-d were assigned to the octahedrally coordinated Cr (III), and the peaks e and f were ascribed to tetrahedrally coordinated Cr (VI). It should be noted that all peaks a-f could be discerned for Ni hydroxide with Cr doping. The as-obtained findings implied that the Cr (III) and Cr (VI) species could be both observed on the surface of $Cr-Ni(OH)_2$ catalysts.

The Cr K-edge from XAFS was further used to reveal the bulk situations. In contrast to the results from the surface studies, Cr (III) was identified as the dominant species. Only a peak at 5990.1 eV could be discerned from the pre-edge region, which was in line with the energy position of the Cr (III) references. The energy position at 5992.8 eV for Cr (VI) references could not be observed from the pre-edge absorption peak for Ni hydroxide with Cr doping (Figure 3.8 b). Moreover, the peak position from the main absorption edge matched with Cr (III) references (Figure 3.7 e). Based on the above analysis from the Cr $L_{3,2}$-edge and K-edge, Cr (III) was the main Cr species from both surface and bulk, with partial oxidation of Cr to form Cr (VI).

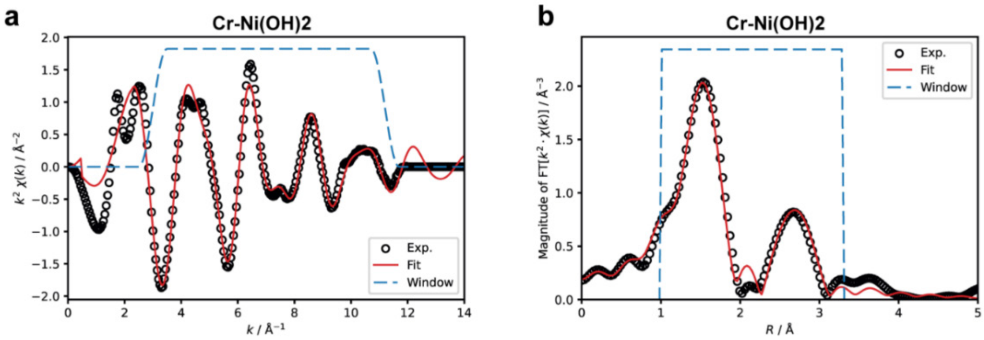

Figure 3.10. EXAFS fitting. (a)-(b) The fitting analysis of Cr K-edged EXAFS measurement of $Ni(OH)_2$.

Table 3.2. Fitting results of Cr K-edge EXAFS.

Sample	**Scattering Path**	**C.N.**	**R(Å)**
$Cr-Ni(OH)_2$	Cr-O	6.0 ± 0.6	1.97 ± 0.01
	Cr-Cr/Ni	5.7 ± 1.1	3.06 ± 0.01
$Cr-Ni(OH)_2$-OER	Cr-O	5.9 ± 0.7	1.97 ± 0.01
	Cr-Cr/Ni	5.7 ± 1.6	3.06 ± 0.02
$Cr-Ni(OH)_2$-UOR	Cr-O	5.8 ± 0.5	1.97 ± 0.01
	Cr-Cr/Ni	5.7 ± 1.3	3.06 ± 0.02

C.N. = coordination number; R = interatomic distance.

The geometric coordination details of the bulk Cr species were further disclosed by EXAFS analysis (Figure 3.7 f and 3.10). It should be noted that 6-coordinated Cr-O with the interatomic distance of 1.97 ± 0.01Å from the first shell exhibited shorter than that of the Ni-O bond (2.06 ± 0.01 Å). The interatomic distance of the Cr-Cr/Ni from the second shell possessed 3.06 ± 0.01 Å, which was close to the Ni-Cr/Ni length (3.09 ± 0.01 Å). In addition, the coordination number was also close to 6 as shown in Table 3.2. As discovered from the above characterization of XRD, Raman, and Ni K-edge EXAFS, the Cr sites with defects nearby were successfully incorporated into the $Ni(OH)_2$ substrate.

Except for the experimental results based on the spectroscopic studies, the role of Cr was further revealed by DFT calculations. The optimized structures of Ni hydroxide with and without Cr doping with defects, including 3-fold, 5-fold, and 6-fold coordinated metal atoms were first constructed. As shown in Figure 3.11, the Bader charge of the corresponding atoms was calculated.

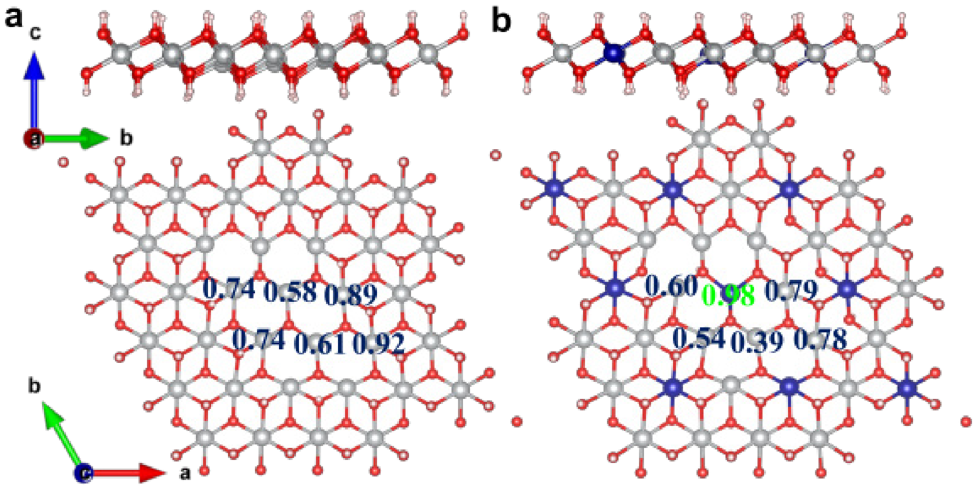

Figure 3.11. (a)-(b) The Bader charge details for $Ni(OH)_2$ and Cr-$Ni(OH)_2$.

It could be discovered that the Cr atoms exhibit more loss charges of 0.98 e^- than those of the Ni atoms at the same position in $Ni(OH)_2$. Moreover, the atomic partial density of states (PDOS) of Ni hydroxide with Cr doping near the Fermi level implied a significant elevation of electrical conductivity as compared to the $Ni(OH)_2$ catalyst (Figure. 3.12).

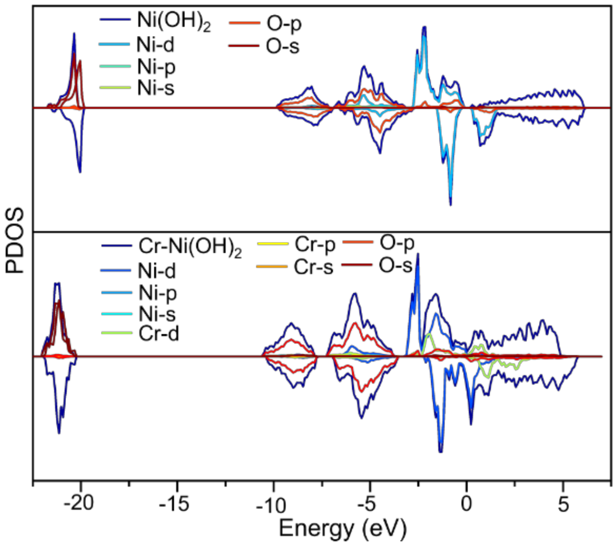

Figure 3.12. PDOS of $Ni(OH)_2$ with and without Cr.

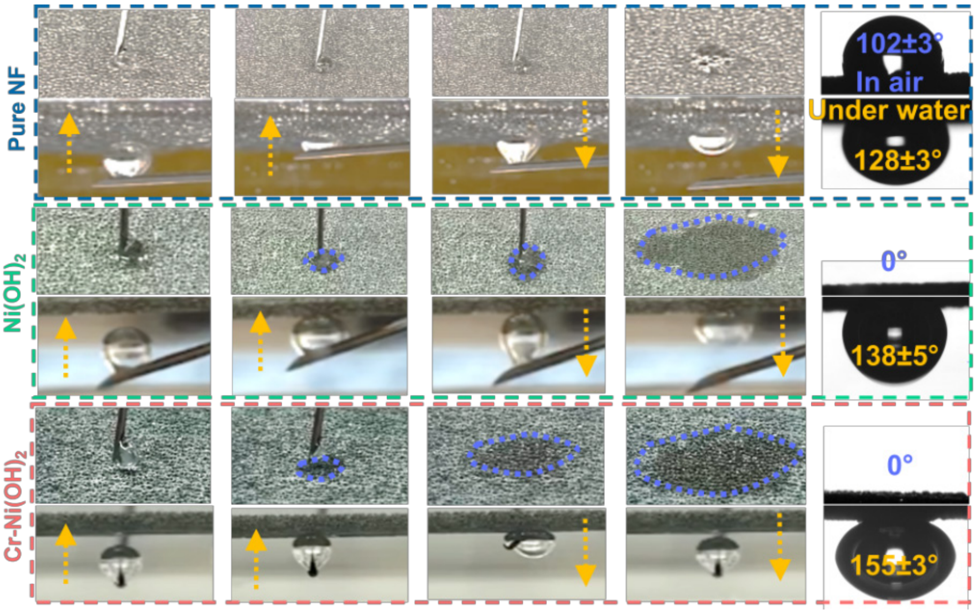

Figure 3.13. Wetting properties measurement for NF, Ni hydroxide with and without Cr doping.

The modulation of the wetting property within the solid-liquid-gas phase is considered an effective tool for achieving well-designed pathways for electrons, ions, and generated or consumed gas substances. To elevate the electrocatalytic performance for gas-evolution reactions, the superhydrophilic-superaerophobic interface can enable good contact between the electrode and electrolyte. In addition, the immediate refreshing of gas bubbles at the interface could be obtained to accelerate the mass transfer and electron transfer. Therefore, to figure out the influence of wetting property on the reaction microenvironment during the UOR process, contact angle measurements were conducted to investigate the behaviors of water droplets in air and gas bubbles underwater (Figure 3.13).

When depositing a 5 μL of water droplet on the surface of Ni hydroxide with Cr doping, the droplet could spread immediately and be absorbed by the surface with WCA of 0°. When depositing a gas bubble on the surface underwater, low adhesion between the gas bubble and electrode could be observed with a BCA of 155°. However, a significant variance in the behavior of water droplets in air and gas bubbles underwater could be witnessed on the surface of NF and Ni hydroxide electrodes. The superhydrophilicity in air and superaerophobicity underwater for Ni hydroxide with Cr doping could optimize the reaction interface with elevated electrochemical performance. Varying molar ratios of Ni_1Cr_1, $Ni_1Cr_{0.5}$, and $Ni_1Cr_{0.125}$ possessed WCA of 0° and BCA of 161 ± 3°, 156 ± 3°, 152 ± 4°, respectively, showing superaerophobic property underwater (Figure 3.14 and 15).

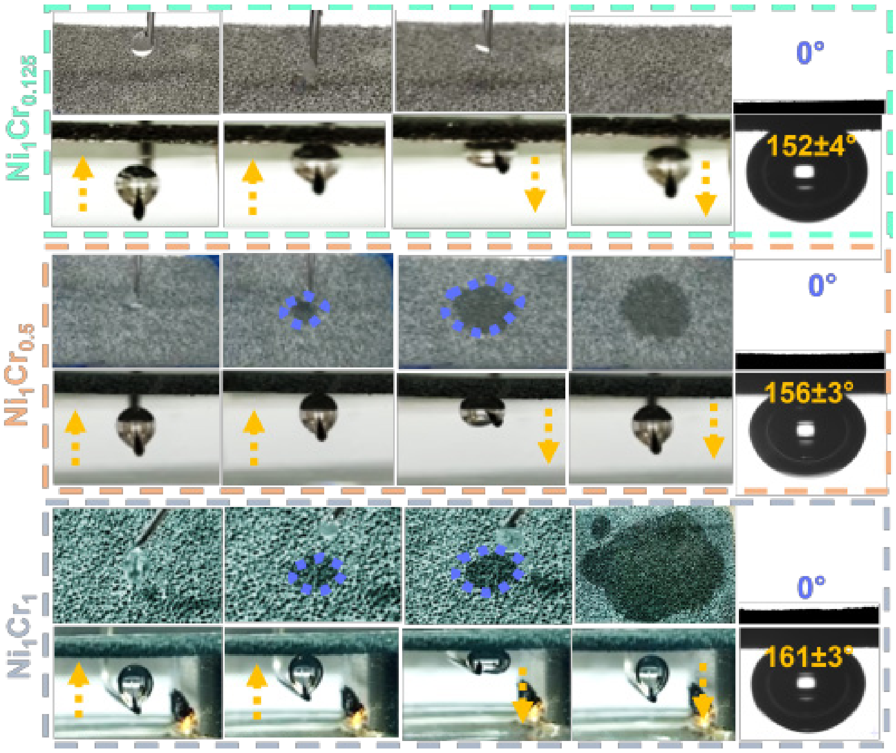

Figure 3.14. The wetting properties of Ni_1Cr_1, $Ni_1Cr_{0.5}$, and $Ni_1Cr_{0.125}$.

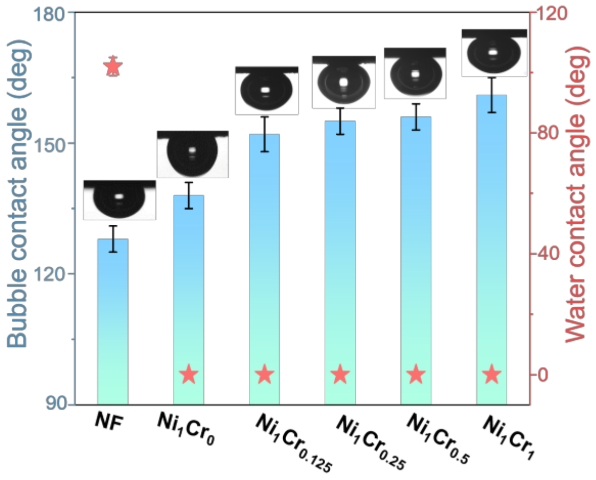

Figure 3.15. BCA underwater and WCA in the air.

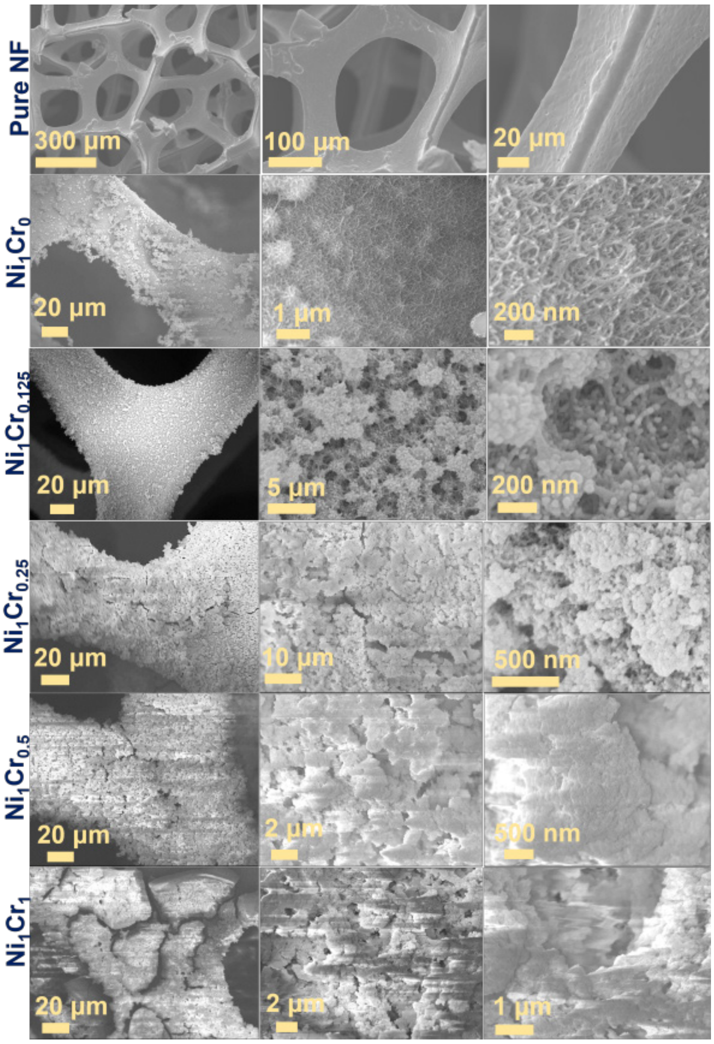

Figure 3.16. SEM images of the morphology of as-prepared catalysts. After incorporating Cr, the rougher hierarchical micro-nano structures were achieved.

As shown in Figure 3.16, micro-nano hierarchical morphologies could be discerned with different feed ratios between Ni and Cr. This was probably because of the co-precipitation of Ni and Cr precursors under alkaline media. During the hydrothermal process, the formation of hydroxide at a varying rate leads to the morphology difference. The micro-nano structure is considered an effective contributing factor to the modulation of wetting properties to elevate the UOR performance.

3.4.2 Electrocatalytic performance

The UOR performances were first evaluated by CV measurement with a wide range of applied potential between 0 - 0.8 V vs. Ag/AgCl. It was found that the oxidation peak of Ni^{2+} to form Ni^{3+} overlapped with the UOR region due to the nearly identical onset potential for the electrochemical step and UOR. The variance in reduction peaks of Ni^{3+} to Ni^{2+} could be discovered. Ni hydroxide with Cr doping possessed a relatively negative shift and higher intensity after the cycle CV measurements. Sufficient Ni^{3+} active sites would form during the electrochemical step due to the optimized reaction interface after incorporating Cr dopants (Figure 3.17).

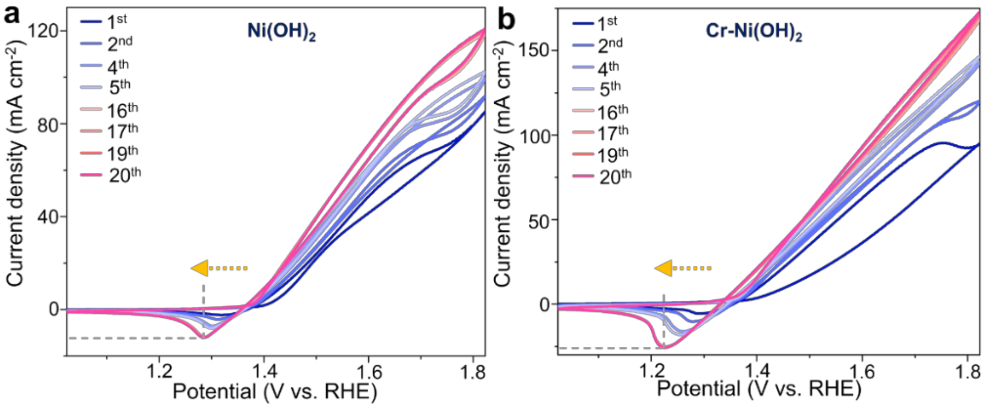

Figure 3.17. Cyclic voltammetry (CV) plots. (a) $Ni(OH)_2$; (b) Cr-$Ni(OH)_2$.

LSV curves were subsequently collected to estimate the potential at varying current densities. It was observed that Ni hydroxide with Cr doping ($Ni_1Cr_{0.25}$) possessed elevated activity as compared to control samples. Only 1.38 V *vs.* RHE was required to drive UOR at 100 mA cm^{-2} (Figure 3.18 a and b). As shown in Figure 3.18 c, a lower Tafel slope (14 mV dec^{-1}) for Ni hydroxide with Cr doping could be found, showing a higher UOR kinetics.

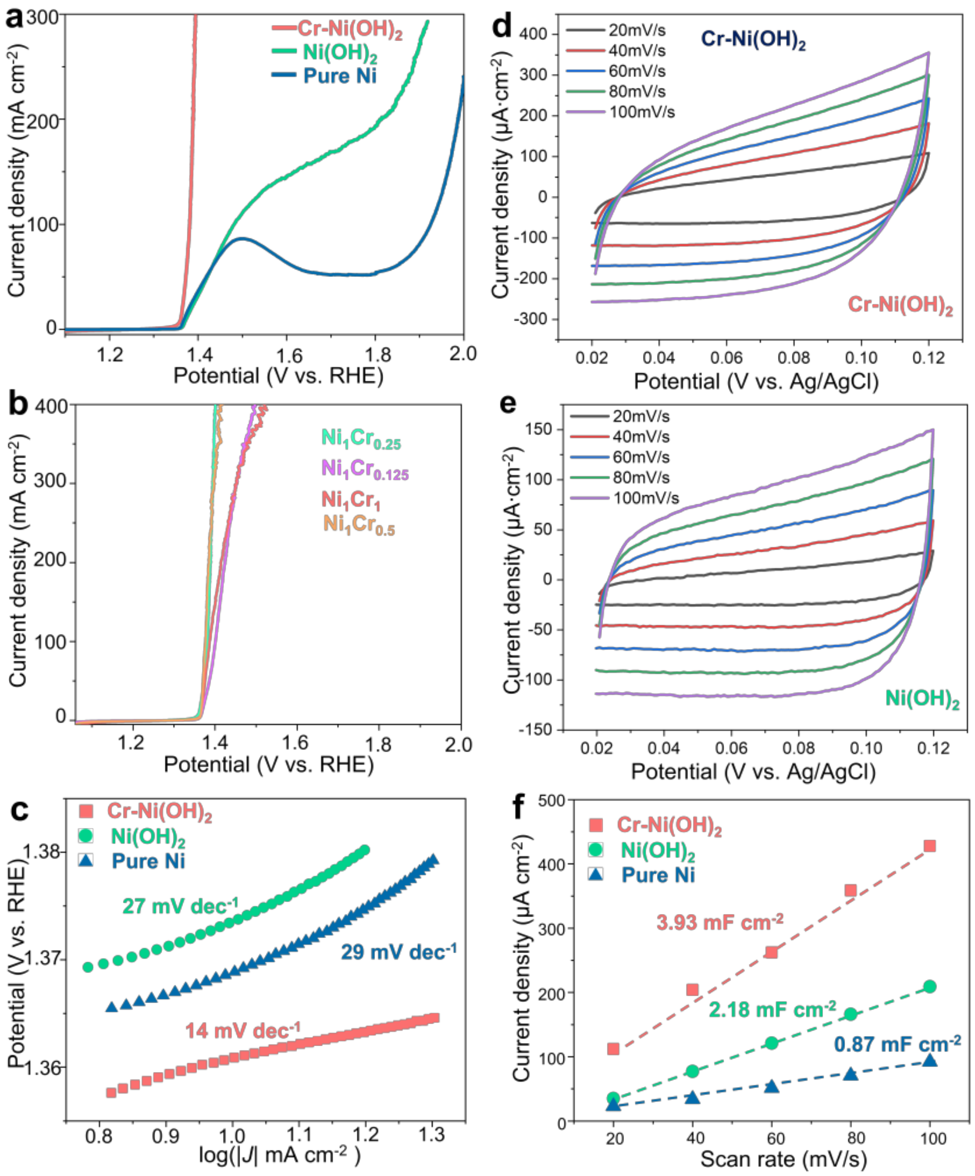

Figure 3.18. Electrochemical performance. (a)-(b) Polarization curves (c) Tafel slopes. CV curves at different scan rates, including 20, 40, 60, 80, and 100 mV/s. (d) Cr-Ni(OH)$_2$; (e) Ni(OH)$_2$. (f) Double-layer capacitances.

As shown in Figure 3.18 d-f, the C_{dl} was measured by the CV test at varying scan rates. The Ni hydroxide with Cr doping possessed the highest C_{dl} value of 3.93 mF cm^{-2}, demonstrating sufficient active sites. Moreover, the activity degradation over a long-term operation test was performed. The chronopotentiometry test with a fixed current density of 10 mA cm^{-2} over 200 hours was conducted to evaluate the stability of as-prepared catalysts (Figure 3.19). almost no notable increase in potential could be observed during the durability test.

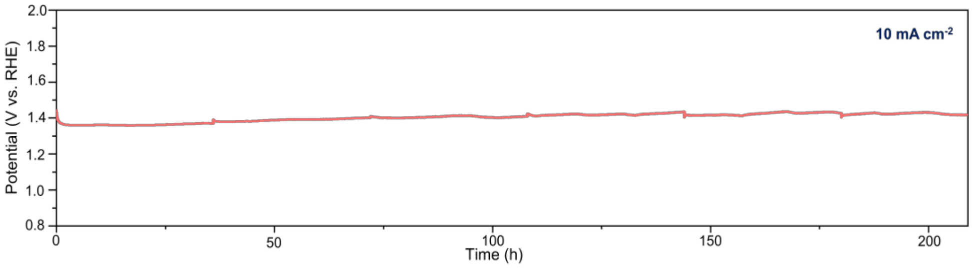

Figure 3.19. Durability test over 200 hours at 10 mA cm^{-2}. The fresh electrolyte was added every 36 hours

Therefore, Ni hydroxide with Cr doping can enable suitable wetting properties to obtain optimal pathways for electrons, ions, and generated gas substances, thus facilitating the enrichment of active sites and rapid reaction kinetics to elevate the UOR performance.

3.4.3 Identification of structure-performance relationship

To probe the structure-performance relationship, the variation in the OER and UOR processes was first compared.

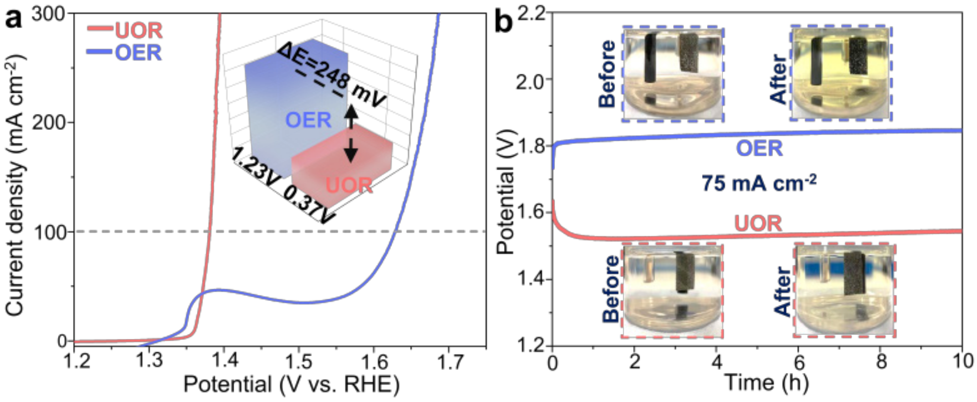

Figure 3.20. (a) LSV curves for OER and UOR. (b) Durability test for OER and UOR at 75 mA cm^{-2}.

The variance in potential at 100 mA cm^{-2} for OER and UOR was discerned with a negative shift of 248 mV as shown in Figure 3.20 a. 10 hours of chronopotentiometry tests for OER and UOR at a fixed current density of 75 mA cm^{-2} was carried out. It could be perceived that the colour of the electrolyte turned yellow after OER (Figure 3.20 b). However, as for UOR, the colour of the electrolyte maintains no notable changes. When the current density was further elevated to 200 mA cm^{-2}, the colour of the electrolyte also turned yellow with increased potential (Figure 3.21).

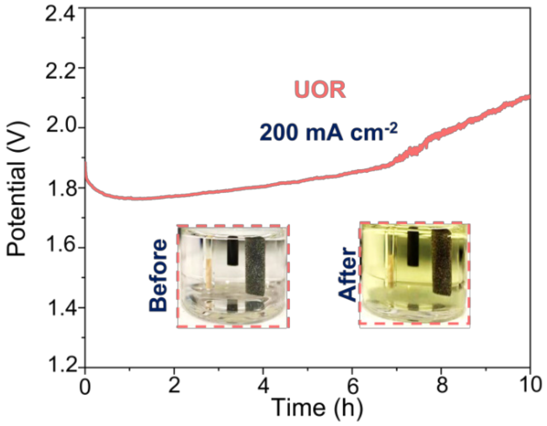

Figure 3.21. Durability test for UOR at 200 mA cm^{-2}.

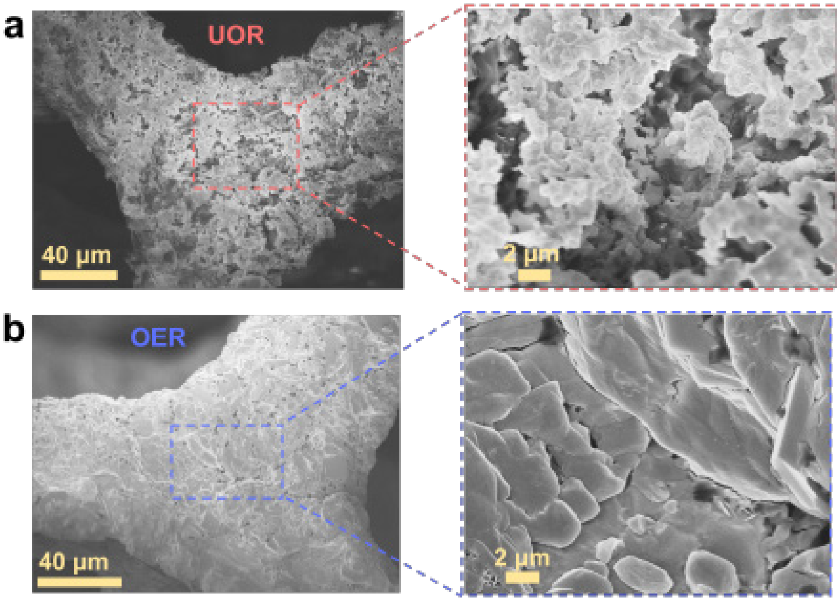

Figure 3.22. Comparison between OER and UOR after durability test.

As shown in Figure 3.22, hierarchical micro-nanostructures were maintained after UOR. However, those structures were damaged during the OER process, thus resulting in a smoother surface.

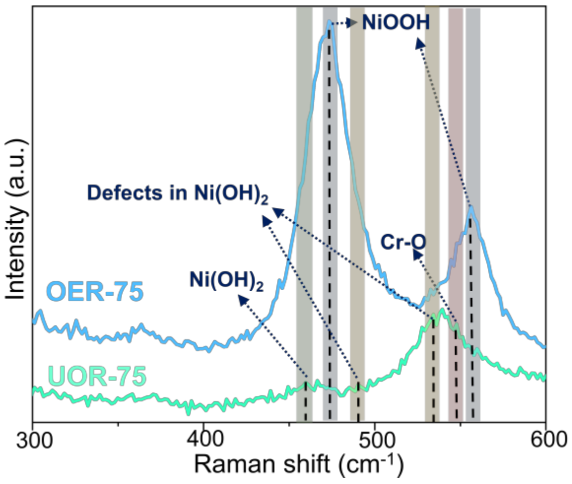

Figure 3.23. Raman spectra of samples of post-UOR and post-OER.

Raman measurement was subsequently conducted to detect the variation of surface. As shown in Figure 3.23, peaks located at 480 and 558 cm^{-1} could be observed after OER, which corresponded to the Ni-O vibration of Ni^{3+} species. As for the Ni hydroxide with Cr doping after UOR, the characterized peaks involving the defective $Ni(OH)_2$ and the Cr-O vibration of Cr (III) species could be maintained after UOR.

As shown in Figure 3.24, XPS measurements were further performed to reveal the variance in Ni active sites after UOR and OER.

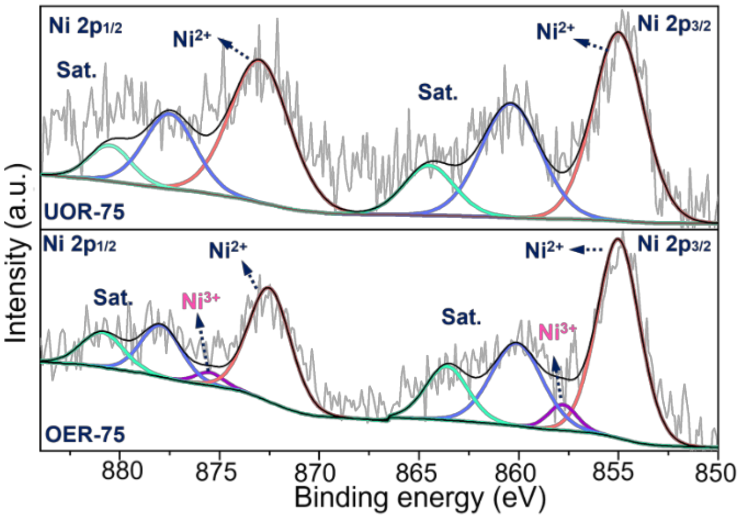

Figure 3.24. XPS spectra of Ni 2p for samples of post-UOR and post-OER

The peaks situated at ~ 855 eV and ~ 873 eV were ascribed to Ni^{2+}. The peaks located at ~ 857.8 eV and ~ 875.5 eV could be discerned after OER, which corresponded to Ni^{3+}. The findings matched with the above observation from Raman spectra.

The electrolytes after one hour of electrolysis at 75 mA cm^{-2} for OER and UOR were further collected to figure out the metal dissolution with the measurement of the UV-vis method as shown in Figure 3.25.

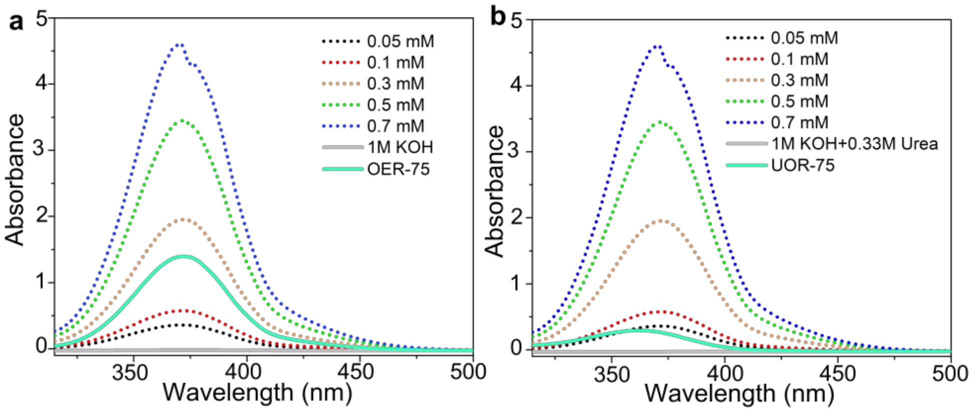

Figure 3.25. UV-vis spectra. (a) The electrolyte after one hour of water electrolysis at 75 mA cm^{-2}. (b) The electrolyte after one hour of urea electrolysis at 75 mA cm^{-2}.

The varying concentrations of 0.05 mM, 0.1 mM, 0.3 mM, 0.5 mM, and 0.7 mM K_2CrO_4 were first prepared as the reference. The peak located at 372 nm could be discerned, which was ascribed to chromate anion (CrO_4^{2-}). The concentration of CrO_4^{2-} from the electrolyte collected after UOR was lower than that of the electrolyte collected after UOR.

Based on the variation in terms of micro-nano structures, chemical compositions, and metal dopant dissolution into electrolytes, it could be noted that Cr dopant leaching would proceed according to the Pourbaix diagram of Cr. As the increase of the applied potential, the Cr (III) species would transit to form CrO_4^{2-} in a strongly alkaline medium. This fundamental theory could be leveraged to explain the Cr leaching issues at the interface during the OER process. The undesirable dopant dissolution is considered the contributing factor in damaging the stability over long-term operation. As compared to the OER process, the Cr leaching could be inhibited during the urea dehydrogenation process.

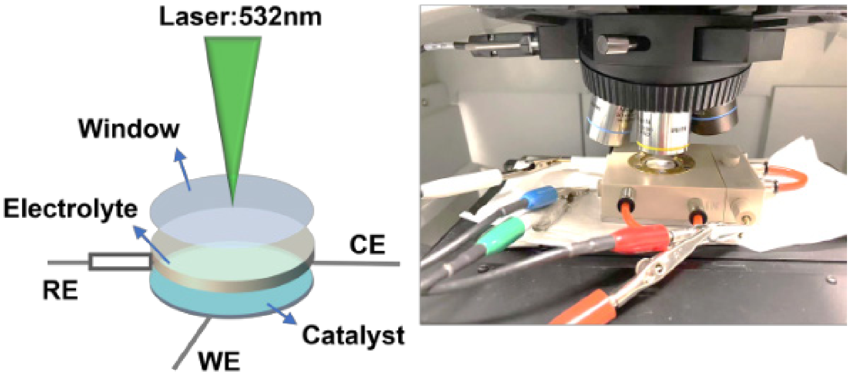

Figure 3.26. Schematic illustrations of *in-situ* Raman measurement for UOR and OER. The ink containing 5 mg catalyst, 200 μL ethanol and 100 μL DI water, 30 μL 5% Nation solution was prepared and 2 μL of ink was then dropped on the glass carbon. The counter electrode was Pt wire and the reference electrode was Ag/AgCl (sat. KCl) electrode. 1 M KOH with and without 0.33 M urea was selected as the electrolyte for OER and UOR, respectively.

To unearth the reaction microenvironments during the OER and UOR process and obtain real-time evolution from the electrochemical interface, *In situ* Raman measurement with a laser wavelength of 532 nm was carried out to figure out the dynamic Cr leaching process. A wide range of applied potential from 1.12 to 1.67 V *vs.* RHE was leveraged to detect the variance in Cr leaching (Figure 3.26).

As shown in Figure 3.27 a, the peak located at 846 cm^{-1} could be discerned from Raman spectra at the potential of 1.52 V *vs.* RHE during the OER process, which corresponded to the symmetric modes of vibration of tetrahedrally coordinated CrO_4^{2-}. However, the potential to detect the emergence of CrO_4^{2-} increased to 1.67 V *vs.* RHE during the UOR process (Figure 3.27 b). The varying applied potential fixed at 1.52 V, 1.62 V, and 1.67 V *vs.* RHE were further employed to obtain a detailed understanding of the Cr leaching process.

The variance in Cr leaching at the potential of 1.52 V *vs.* RHE between OER and UOR could be found. After around 20 mins, the characterized peak of CrO_4^{2-} emerged as shown in Figure 3.27 c. However, no notable peaks of

CrO_4^{2-} could be discerned during the UOR process (Figure 3.27 d). When further increasing the applied potential to 1.62 V *vs.* RHE, the Cr leaching process was still not discovered as shown in Figure 3.27 e. After around 40 mins at the potential of 1. 67 V *vs.* RHE, the notable peak of CrO_4^{2-} emerged (Figure 3.27 f). According to the Raman spectra for OER and UOR under varying applied potentials, Cr leaching issues could be inhibited during the urea dehydrogenation process. It should be noted that the Cr leaching could still happen at a higher potential.

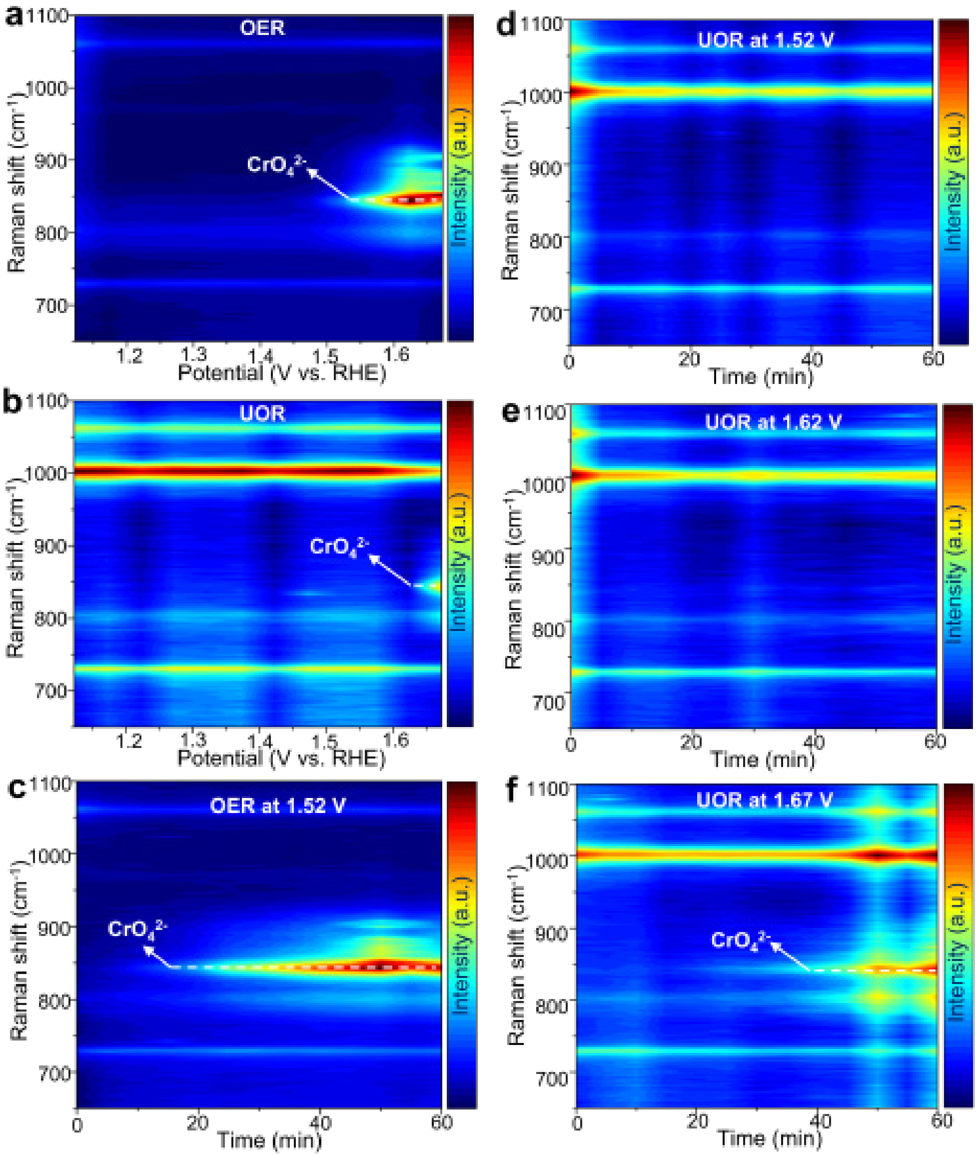

Figure 3.27. (a) In situ Raman measurement during OER under a wide range of applied potentials. (b) In situ Raman measurement during UOR under a wide range of applied voltages. (c) One-hour Raman measurement at 1.52 V

vs. RHE during OER. (d) One-hour Raman measurement at 1.52 V *vs.* RHE during UOR. (e) One-hour Raman measurement at 1.62 V *vs.* RHE during UOR. (f) One-hour Raman measurement at 1.67 V *vs.* RHE during UOR.

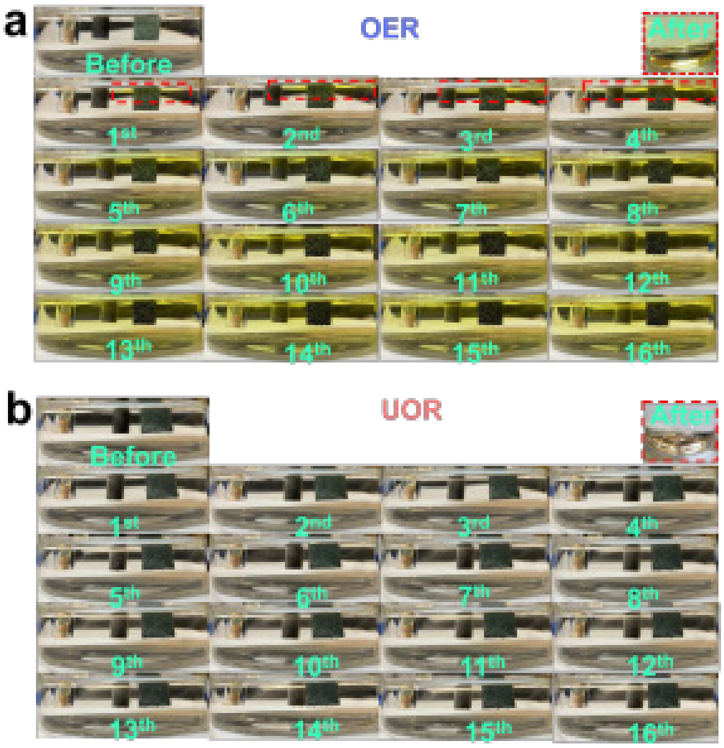

Figure 3.28. Cycle test of LSV for UOR and OER processes conducted with potential ranging from 0 - 0.8 V vs. Ag/AgCl.

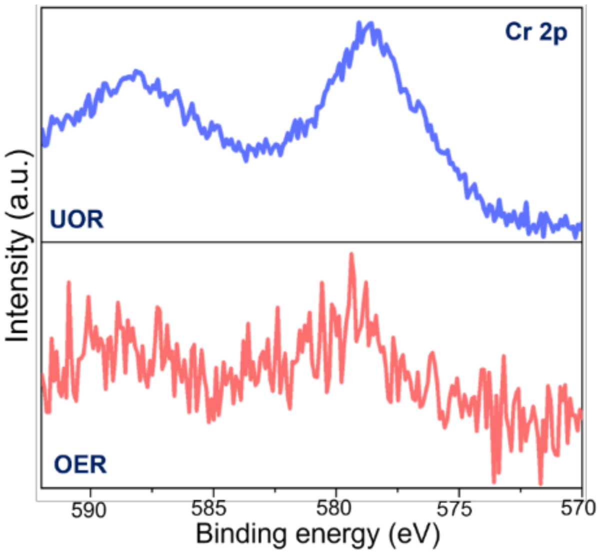

Figure 3.29. XPS spectra of Cr 2p to validate the variation of the dopant stability after OER and UOR, respectively.

The cycle test of LSV was further carried out to intuitively reveal the metal dissolution process. The yellow colour change of the electrolyte around the electrode was discerned and gradually dispersed to the whole electrolyte as the cycle number increased during the OER process (Figure 3.28 a) As shown in Figure 3.28 b, no notable colour change was observed during the UOR process. XPS measurement was conducted to probe the stability of Cr dopants. According to the high-resolution XPS spectra of Cr 2p, the lower intensity of Cr after OER demonstrated serious Cr leaching from the electrode as compared to the UOR process (Figure 3.29).

NEXAFS and XAFS of Ni hydroxide with Cr doping after OER and UOR were measured in terms of both surface and bulk to obtain a reliable understanding of the structure-performance relationship at the electrochemical interface.

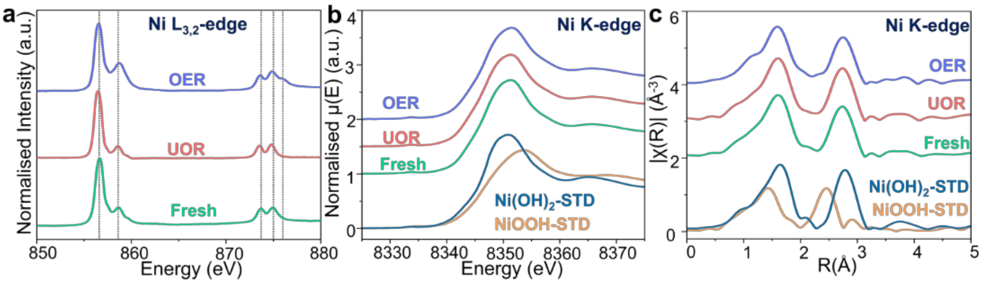

Figure 3.30. (a) Ni $L_{3,2}$-edge from NEXAFS. (b) Ni K-edge from XANES. (c) Ni K-edge from EXAFS.

As shown in Figure 3.30, the higher peak intensity situated at 858.2 eV was discerned after OER according to the Ni L_3-edge spectra from NEXAFS. Moreover, the additional peak located at 876.0 eV was found, which corresponded to Ni^{3+} species on the electrode surface after OER. However, the Ni^{2+} was verified as the dominant species with imperceptible Ni^{3+} fingerprints after UOR. This finding matched with the above detection of Raman spectra and XPS measurement. As compared to the process of urea dehydrogenation, the Ni^{3+} was the dominant species on the electrode surface after OER. Except for the analysis of the surface, the bulk situations were further disclosed. The Ni K-edge spectra presented no notable discrepancies in XANES edge positions and pre-edge features (Figure 3.30 b and 3.31). Moreover, the coordination configurations of Ni hydroxide with Cr doping after OER and UOR exhibited no significant variance (Figure 3.30 c, Figure 3.32, and Table 3.1).

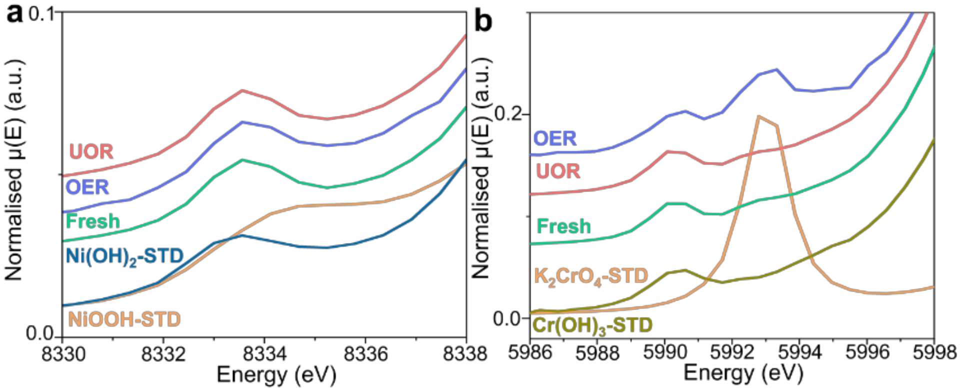

Figure 3.31. The pre-edge of XANES Ni K-edge (a) and Cr K-edge (b).

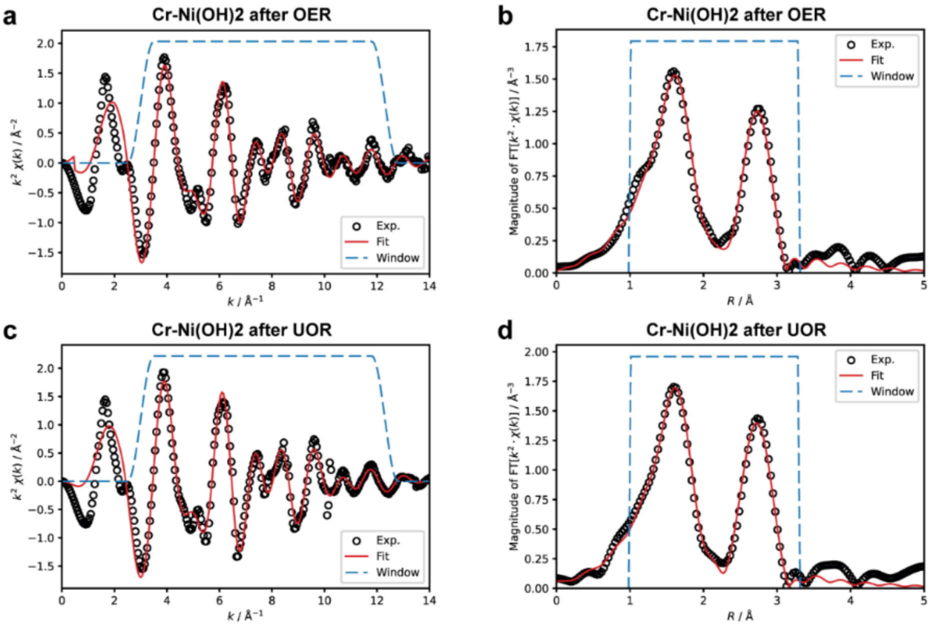

Figure 3.32. EXAFS fitting. (a)-(b) The fitting analysis of Ni K-edged EXAFS measurement of the post-OER sample. (c)-(d) Ni K-edged EXAFS measurement of the post-UOR sample.

It should be noted that adsorption and desorption of reactants and intermediates during the OER and UOR process usually proceed on the interface between the electrode and electrolyte with mass and electron transfer. This is the reason that the Ni^{3+} species could be found on the surface after OER. In addition, as shown in Figure 3.33, Cr^{6+} species were discerned from the Cr $L_{3,2}$-edge NEXAFS on the surface of Ni hydroxide with Cr doping after OER and UOR. However, Cr K-edge spectra in XANES edge positions and pre-edge features exhibited that Cr^{6+} could only be observed for the electrode after OER (Figure 3.33 b and 3.31 b). This finding was in line with the previous analysis of the Cr leaching process with the oxidation of Cr (III) to form Cr (VI) during the OER process. In contrast, the Cr dissolution to the electrolyte was significantly inhibited during the UOR process.

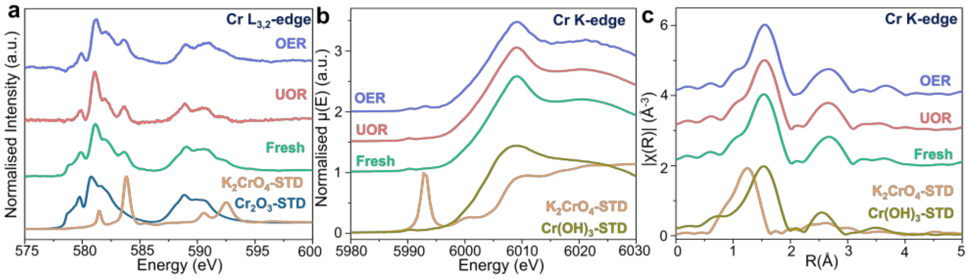

Figure 3.33. EXAFS fitting. (a) Cr $L_{3,2}$-edge from NEXAFS; (b) Cr K-edge from XANES of; (c) Cr K-edge from EXAFS.

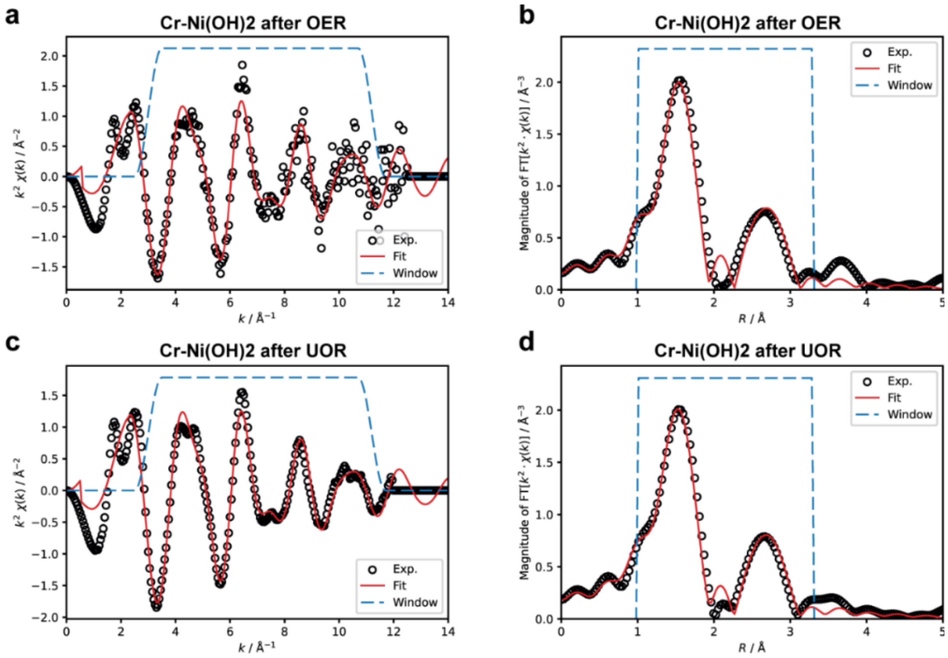

Figure 3.34. EXAFS fitting. (a)-(b) The fitting analysis of Cr K-edged EXAFS measurement of the post-OER sample. (c)-(d) Cr K-edged EXAFS measurement of the post-UOR sample.

Furthermore, DFT calculations were carried out to figure out the Cr leaching process from the adsorption energy. The adsorption configurations of urea and hydroxide ions were constructed with the model of NiOOH and Cr-

NiOOH. This is due to the fact that the real active site is NiOOH for urea dehydrogenation.

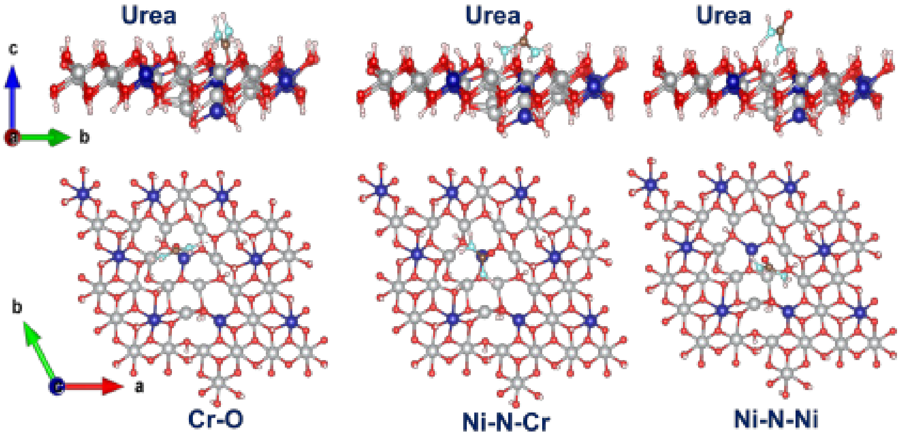

Figure 3.35. The adsorption configurations include the interaction between the O atom and N atom in urea and the Ni atom and Cr atom in the Cr-NiOOH, which were described as Cr-O, Ni-N-Cr, and Ni-N-Ni.

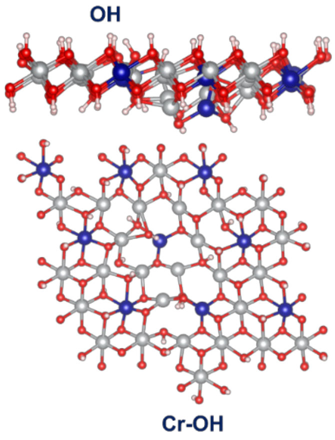

Figure 3.36. The adsorption configurations include the interaction between the OH and the Cr atom in the Cr-NiOOH, which was described as Cr-OH.

As shown in Figure 3.35, the urea adsorption configurations involving Cr-O, Ni-N-Cr, and Ni-N-Ni were incorporated into the model of Cr-NiOOH. The configuration of Cr-O possessed the lowest adsorption energy of -1.30 eV among other configurations (Table 3.3).

The *OH adsorption configuration of Cr-OH on Cr-NiOOH was employed to analyze the OER process (Figure 3.36). It was discerned that the positive adsorption energy of 0.23 eV was higher than all the configurations for urea adsorption. This result can be used to explain the reason why Cr leaching is inhibited during the urea dehydrogenation process. The urea molecules would favorably adsorb on the surface of Cr-NiOOH to suppress the Cr dopant leaching.

Table 3.3. The adsorption energies of urea on NiOOH and Cr-NiOOH and *OH on Cr-NiOOH after structural optimization.

Reaction	Structure	Eads/eV
UOR	NiOOH (Ni-O)	-0.69
	NiOOH (Ni-N-Ni)	-1.05
	Cr-NiOOH (Cr-O)	-1.30
	Cr-NiOOH (Ni-N-Ni)	-0.96
	Cr-NiOOH (Ni-N-Cr)	-1.03
OER	Cr-NiOOH (Cr-OH)	0.23

To validate the ability of urea-assisted water electrolysis, LSV curves were collected by the two-electrode electrolyzers. The notable variance in current density at varying applied cell voltage of 1.4 V, 1.6 V, and 1.8 V could be found, which was 4.5-fold, 4.8-fold, and 5-fold higher than that of HER-OER (Figure 3.37 a).

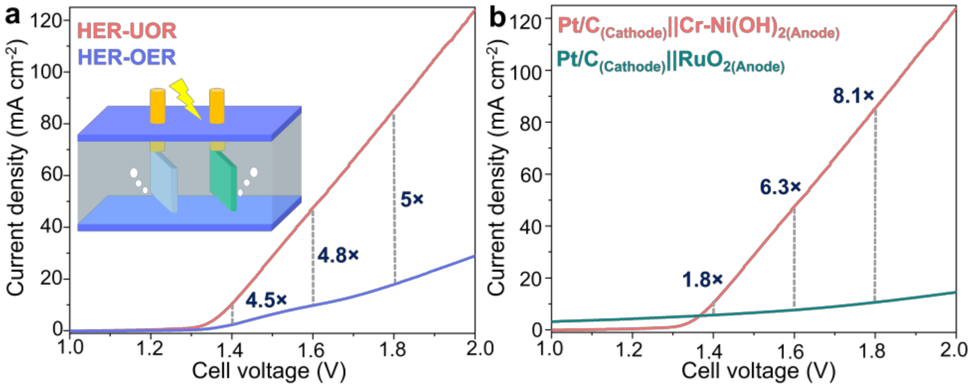

Figure 3.37. (a) LSV curves for two-electrode electrolysis for urea and water. Using commercial Pt/C (loading mass of 0.5 mg cm^{-2}) as a catalyst drop-casted on carbon paper. (b) Comparison of LSV curves between the as-prepared catalysts and the benchmark of noble metals. Using commercial Pt/C and RuO_2 (loading mass of 0.5 mg cm^{-2}) as the cathode and anode.

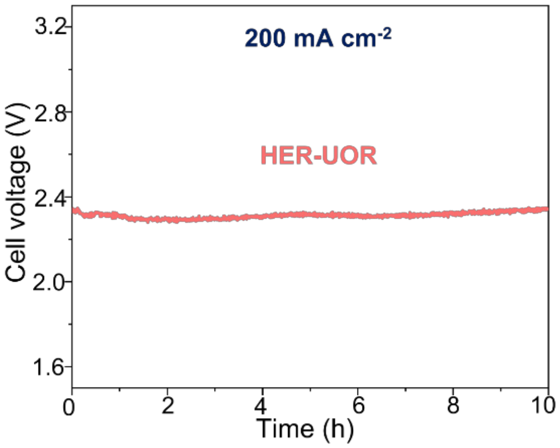

Figure 3.38. Durability test at 200 mA cm^{-2}.

Moreover, as shown in Figure 3.37 b, the current density exhibited 1.8-fold, 6.3-fold, and 8.1-fold higher than that of the benchmark catalysts (Pt/C and RuO_2). Furthermore, a durability test was conducted to evaluate the stability of urea-assisted water electrolysis. No notable increase in cell voltage over 10 h at 200 mA cm^{-2} could be found (Figure 3.38).

3.5. Conclusion

In this chapter, the non-noble metal doped Ni catalysts were first synthesized with the hydrothermal method and further used as the proof-of-concept to verify the stability of dopant structures during oxidation reactions. By combining the *in situ* spectroscopic observation and DFT calculations, the Cr leaching issues were revealed during the process of OER and UOR, respectively. The urea molecules would preferentially adsorb on the surface to suppress the Cr leaching into the electrolytes with the formation of chromate. Additionally, the co-precipitation of different feed ratios between Ni and Cr precursors under alkaline media could lead to the formation of hydroxide with different morphologies, thus enabling modulation of wetting properties to obtain well-designed pathways for electrons, ions, and generated gas substances. The superhydrophilic-superaerophobic properties could facilitate mass and electron transfer, thus elevating the UOR performance. Only a potential of 1.38 V (*vs.* RHE) is required at 100 mA cm^{-2}. The investigation of the Cr leaching process at the electrochemical interface opens a new avenue for the exploration of stability issues of dopant structure, inspiring the subsequent design of high-performance Ni-based UOR catalysts and other small molecule oxidation reactions. The discoveries in this chapter also empower the development of electrocatalysts to meet the requirements of industrial applications.

3.6. References

1. Q. Xu; J. Zhang; H. Zhang; L. Zhang; L. Chen*, et al. Energy Environ. Sci.*, **2021**, *14*, 5228-5259.

2. L. Gao; X. Cui; C. D. Sewell; J. Li; Z. Lin. *Chem Soc Rev*, **2021**, *50*, 8428-8469.

3. X. Wu; Y. Wang; Z.-S. Wu. *Chem*, **2022**, *8*, 2594-2629.

4. R. Luo; Y. Li; L. Xing; N. Wang; R. Zhong*, et al. Appl. Catal., B*, **2022**, *311*, 121357.

5. Y. Lu; T. Liu; C. L. Dong; Y. C. Huang; Y. Li*, et al. Adv Mater*, **2021**, *33*, e2007056.

6. W.-J. Liu; Z. Xu; D. Zhao; X.-Q. Pan; H.-C. Li*, et al. Nat. Commun.*, **2020**, *11*, 265.

7. S. Bai; Y. Xu; K. Cao; X. Huang. *Adv Mater*, **2021**, *33*, 2005767.

8. L. Wang; Y. Zhu; Y. Wen; S. Li; C. Cui*, et al. Angew Chem Int Ed Engl*, **2021**, *60*, 10577-10582.

9. Y. Xu; X. Chai; T. Ren; S. Yu; H. Yu*, et al. Chem Commun (Camb)*, **2020**, *56*, 2151-2154.

10. A. T. Miller; B. L. Hassler; G. G. Botte. *J. Appl. Electrochem.*, **2012**, *42*, 925-934.

11. Y. Xu; T. Ren; K. Ren; S. Yu; M. Liu*, et al. Chem. Eng. J.*, **2021**, *408*, 127308.

12. W. Chen; L. Xu; X. Zhu; Y. C. Huang; W. Zhou*, et al. Angew Chem Int Ed Engl*, **2021**, *60*, 7297-7307.

13. W. Xu; Z. Lu; X. Sun; L. Jiang; X. Duan. *Acc Chem Res*, **2018**, *51*, 1590-1598.

14. W. Sun; J. Li; W. Gao; L. Kang; F. Lei*, et al. Chem Commun (Camb)*, **2022**, *58*, 2430-2442.

15. Y. Duan; J. Y. Lee; S. Xi; Y. Sun; J. Ge*, et al. Angew Chem Int Ed Engl*, **2021**, *60*, 7418-7425.

16. G. Solomon; A. Landström; R. Mazzaro; M. Jugovac; P. Moras*, et al. Adv. Energy Mater.*, **2021**, *11*, 2101324.

17. H. Jiang; M. Sun; S. Wu; B. Huang; C. S. Lee*, et al. Adv. Funct. Mater.*, **2021**, *31*, 2104951.

18. J. Sun; H. Xue; Y. Zhang; X. L. Zhang; N. Guo*, et al. Nano Lett*, **2022**, *22*, 3503-3511.

19. S. Klaus; Y. Cai; M. W. Louie; L. Trotochaud; A. T. Bell. *J. Phys. Chem. C*, **2015**, *119*, 7243-7254.

20. C. Sun; Q. Song; J. Lei; D. Li; L. Li*, et al. ACS Appl. Energy Mater.*, **2021**, *4*, 8791-8800.

21. M. Mohammadtaheri; Q. Yang; Y. Li; J. Corona-Gomez. *Coatings*, **2018**, *8*, 111.

Chapter 4. Single atomic noble metal modified Ni Catalysts

4.1 Acknowledgement

I acknowledged Xuedan Song and Qing Zhang for the DFT calculations and analysis as well as the help from Liqun Kang and Longxiang Liu about the XAS spectrum analysis. Besides, I also acknowledged Jiexin Zhu, Fei Guo, Kaiqi Li, Jianrui Feng, Lixue Xia, Lei Lv, Wei Zong, Dan J.L. Brett, Paul R. Shearing, Liqiang Mai, Ivan P. Parkin, Guanjie He for their useful suggestion. The work described in this chapter was published in the journal of Energy Environ. Sci. (DOI: 10.1039/d3ee03258b) and I was the first author. The contents including the images reproduced from this paper were with permission from the publisher, Royal Society of Chemistry.

4.2 Introduction

The organic compound oxidation reactions display promising routes in varying energy conversion scenarios[1-3]. Among those reactions, UOR possesses sufficient resources from urea-bearing wastewater and relatively lower theoretical potential, thus gaining wide attention from the research community[4]. It should be noted that tons of untreated wastewater containing urea from industrial or domestic sources are directly discharged, thereby seriously destroying the ecosystem[5, 6]. On the condition that we directly leverage urea-bearing wastewater as the reactant source for the UOR and pair with HER or other cathodic reactions with high-value product generation, a sustainable and energy-saving vision could be achieved. Meanwhile, water treatment is realized.

The Ni-based materials, as widely used UOR electrocatalysts, can generate high NiOOH active sites during the electrochemical step for urea dehydrogenation[7]. With the assistance of further modification, the elevated UOR performance could be obtained by incorporating abundant Ni^{3+} active sites. The UOR pathway usually includes two steps. Urea dehydrogenation occurs after the electrochemical step to form dynamic active Ni^{3+} sites[8, 9]. Reduction of NiOOH proceeds subsequently during the urea dehydrogenation process. It was claimed by Qiao's group that the $Ni_2Fe(CN)_6$ catalyst was proposed with a unique UOR pathway. This Ni-Fe cyanide material can catalyze the UOR with the potential before the electrochemical step for Ni^{3+} formation[10]. Wang's group also reported the Ru-Co/NiO catalyst that can lead to a low potential to drive UOR before the electrochemical step for Ni^{3+} formation[11]. With the continuous development of Ni-based UOR electrocatalysts, the Ni site can still form NiOOH species as the applied potential increases over long-term operation. The reliable reaction pathway should be applicable within a wide range of reaction conditions.

Moreover, considering the urea concentration in human urine is around 0.33 M, the majority of studies are working based on this specific concentration or within a low urea concentration ($C_{urea} < C_{KOH}$=1 M)[12]. However, the urea dehydrogenation process plays a crucial role in influencing the Ni active sites due to the reduction effect. The situation of high urea concentrations ($C_{urea} > C_{KOH}$ =1 M) from some industrial urea-bearing wastewater, is often overlooked by the research community to obtain a thorough understanding of the structure-performance relationship.

Insufficient Ni^{3+} active sites can lead to passivation issues with the competition between OER and UOR. As demonstrated by Wang's group[13, 14], Ni oxide/hydroxide undergoes the self-oxidation process. However, the potential-dependent process of the electrochemical step to form Ni^{3+} active species would cause the accumulation of NiOOH species with the increase of applied potential. The limited mass transfer would also result in the high valence state of Ni not being promptly reduced. It should be noted that the NiOOH is considered the shared active site for OER and UOR. Therefore, the abundant active NiOOH species play a key role in ameliorating the passivation issues (Figure 4.1 a). As reported by previous studies[15], the passivation issues with current depletion could be fixed by enabling abundant active Ni^{3+} sites by pre-activation of electrochemical step to generate NiOOH species.

In addition, the formation of Ni^{3+} active sites can be inhibited during the urea dehydrogenation process due to the reduction of Ni^{3+} to Ni^{2+}. Particularly, the high urea concentrations would lead to sufficient urea molecules at the interface, thus imposing difficulties in maintaining the sustained efficiency of high UOR activity. Furthermore, despite numerous studies working on modifying Ni-based materials to regulate the dynamic active Ni^{3+} sites, the reaction microenvironment during the UOR process still requires an effective tool to reveal the structure-performance relationship.

The atomic heterostructure engineering strategy is a promising method to regulate the electronic structure and stabilize the intermediate. Single atom catalysts (SACs) possess well-defined atom coordination and tunable electronic structures [16, 17], which is an effective route to improve atom utilization efficiency for noble metals with low loading mass to reduce the cost. However, SAC is rarely reported to catalyze UOR and the origin of activity remains ambiguous[18-20].

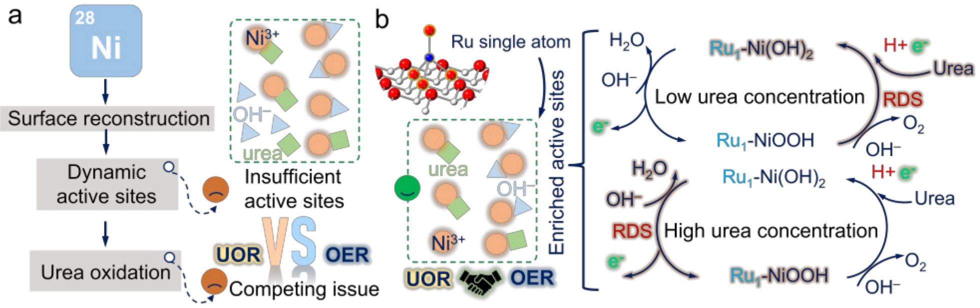

Figure 4.1. Current issues of Ni-based UOR catalysts. (a) Competition between OER and UOR due to insufficient active sites. (b) The highlight of Ru atomic sites into $Ni(OH)_2$.

In this chapter, motivated by the above analysis, an atomic heterostructure engineering strategy was leveraged to synthesize an atomic Ruthenium (Ru) catalyst anchored on Ni hydroxide (Ru_1-$Ni(OH)_2$). Ru has partially filled electrons in d orbitals and a wide range of oxidation states, which possess a high potential to modify the Ni-based catalyst to form sufficient Ni^{3+} active sites. However, the high cost of Ru hinders the practical application. Therefore, Ru-O_4 coordinated configuration anchored on Ni hydroxide was obtained by hydrothermal method to facilitate the adsorption of OH^- to boost the electrochemical step to form abundant NiOOH species. In addition, the critical roles of urea dehydrogenation and Ni oxidation in both low and high urea concentrations were unveiled by *in situ* spectroscopy observation (Figure 4.1 b).

4.3 Electrocatalytic performance

4.3.1 Synthesis of Ru_1-$Ni(OH)_2$ catalysts

The modified hydrothermal method was used to synthesize Ru_1-$Ni(OH)_2$. Specifically, The Ni and Ru precursors including 365 mg $Ni(NO_3)_2 \cdot 6H_2O$ and 10 mg $RuCl_3 \cdot xH_2O$ were first dissolved in 30 mL DIW. 240 mg urea was then added to create an alkaline medium during the hydrothermal process. The pre-cleaned NF (4 cm x 2 cm, thickness of 1 mm) was immersed in the above solutions, which was followed by a hydrothermal process with a temperature of 120 °C and lasted for 12 h.

The Ru_1-$Ni(OH)_2$ electrocatalysts were finally obtained after cleaning and drying at 60 °C for 10 h. The powder samples were obtained from centrifugation of the precipitates and dried at 60 °C for 10 h. The Ru_1-$Ni(OH)_2$ catalyst with different feed ratios of Ru was synthesized with a similar process. The $Ni(OH)_2$ catalyst was fabricated according to the work in Chapter 2 without adding the Ru precursor. To avoid the effect of NF substrate, the ink containing 4 mg Ru_1-$Ni(OH)_2$ powder catalysts, 20 μL Nafion, and 300 μL ethanol was drop-casted on carbon paper (CP).

Ru_1-$Ni(OH)_2$ was further phosphorized to obtain P-Ru_1-$Ni(OH)_2$ catalysts. The phosphorization process involved the first step of pre-flushing with N_2 for 10 min with the pre-samples and 1 g NaH_2PO_2 placed on the upstream side in the tube furnace. The second step required heating treatment at 300 °C with a ramping rate of 10 °C min^{-1}. The time for the phosphorization process lasted for 1 h. The P-Ru_1-$Ni(OH)_2$ was finally obtained when the temperature was decreased from 300 °C to 25 °C.

To obtain benchmark electrodes for HER, the ink containing 1 mg commercial Pt/C, 300 μL ethanol, and 20 μL Nafion was drop-casted on CP and dried at room temperature. The RuO_2 was leveraged as the anodic benchmark electrode with an identical preparation process. The RuO_2 electrode was used for the electrochemical performance comparison with the Ru_1-$Ni(OH)_2$ catalyst.

4.3.2 Characterizations

XPS, Thermo scientific K-alpha photoelectron spectrometer, was used to analyze the chemical composition. The 284.8 eV for C 1s was first used for calibration before estimating the chemical states. XRD patterns were collected by STOE SEIFERT diffractometer with the radiation of the Mo source. The morphology and microstructures of samples were evaluated with scanning electron microscope (SEM, JEOL LSM 7600) and transmission electron microscope (JEOL, JEM-2100). MP-AES (Agilent 4210) was leveraged to confirm the Ru loading mass.

STEM images were collected by a probe-corrected (CEOS) JEOL ARM300CF electron microscope (JEOL, Japan) at the electron Physical Science Imaging Centre (ePSIC) E02 beamline of Diamond Light Source (UK).

The XAFS characterizations were conducted to obtain Ru K-edge and Ni K-edge spectra at P65 beamline of PETRA III (Germany). The XAFS spectra at both Ru K-edge and Ni K-edge were collected in transmission mode, and the intensity of the incident beam (I_0) and the transmitted beam (I_t) was monitored by ionization chambers. Ru foil or Ni foil was measured simultaneously for each sample as the reference for energy calibration.

The *In situ* Raman measurement was used to reflect the real-time situation in the reaction microenvironment with the usage of Bruker Senterra Raman spectrometer. The wavelengths and laser power were set to 532 nm and 12.5 mW. The working electrode was the Ru_1-$Ni(OH)_2$ prepared on NF. The counter electrode was Pt wire and the reference electrode was Ag/AgCl (sat. KCl) electrode. 1 M KOH with and without 0.33 M urea was selected as the electrolyte for OER and UOR respectively.

4.3.3 Electrochemical measurement

An electrochemical cell configuration was used to evaluate the UOR performance. 1 M KOH solution with and without 0.33 M urea was utilized as the electrolyte for UOR and OER, respectively. The Ru_1-$Ni(OH)_2$ catalyst on NF was employed as the working electrode. The carbon rod was used as the counter electrode. As for the reference electrode, an Ag/AgCl electrode filled with saturated KCl solution was used. Potentiostat (Gamry Interface 1000) was used to set up varying electrochemical test modes. Cyclic voltammetry (CV) was performed to observe the oxidation and reduction peaks. The linear sweep voltammetry (LSV) was carried out at a scan rate of 5 mV s^{-1} to estimate the potential at varying applied potentials. The potential conversion was operated according to $E_{RHE}= E_{Ag/AgCl} + 0.197 + 0.059$ pH. The Tafel plot was gained by replotting the polarization curve (Y-axis: potential, X-axis: log|current density|). The Tafel slope was thus obtained from a linear fitting of the Tafel plot. A durability test with a constant current density was performed to observe the performance degradation over the long-term operation. LSV measurements were presented with IR compensation. The CV within a non-Faradaic potential from 0.02 - 0.12 V *vs.* Ag/AgCl was performed to measure the C_{dl}.

In situ EIS measurements were carried out to figure out the potential-dependent interfacial electron charge transfer behavior in varying phases. The frequency ranging from 10^{-2} to 10^{5} Hz was leveraged.

Zn-air and Zn-urea-air battery tests were performed to evaluate the applicability of UOR to replace OER. The polished Zn plate was used as the negative electrode. and The positive electrode was prepared by drop-casting catalysts ink including 1 mg Ru_1-$Ni(OH)_2$ and 1 mg Pt/C, 20 μL Nafion, and 300 μL ethanol on CP. To reduce the effect of continuous urea consumption on activity, fresh electrolyte was added every 10 hours.

MEA test was carried out to evaluate urea-assisted water electrolysis under large current density. The setup of two stainless steel plates that have circular serpentine channels (1 cm^{-2}) was utilized. The anodic electrode was the Ru_1-$Ni(OH)_2$ and the cathodic electrode was the P-Ru_1-$Ni(OH)_2$. The anion exchange membrane (Sustainion X37-50 Grade 60) was used to separate the anode and cathode. The electrolyte was 1M KOH and 2M urea.

4.3.4 DFT calculation

The DFT calculations were carried out by the software of Vienna ab initio simulation package (VASP) with the projector augmented wave (PAW) pseudopotential. The exchange and correlation interactions were presented by Generalized gradient approximation (GGA) of Perdew-Burke-Ernzerhof (PBE) functional. The empirical correction of the Grimme's scheme (DFT-D3), the cut-off energies of 500 eV, and the *k*-point grid of 3×3×1 were used for all calculations.

4.4 Results and discussion

4.4.1 Ru_1-$Ni(OH)_2$ catalysts

XRD measurements of Ni hydroxide with varying feed amounts of Ru precursors were conducted and only a single bulk phase of α-$Ni(OH)_2$ (PDF No. 38-0715) could be observed as shown in Figure 4.2 a. No notable variance in XRD spectra could be observed between Ni hydroxide with varying feed amounts of Ru precursors.

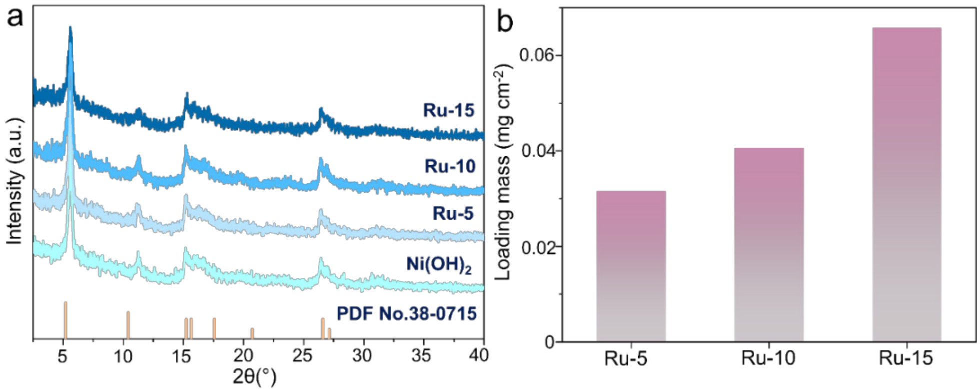

Figure 4.2. (a) XRD patterns of $Ni(OH)_2$ and Ru_1-$Ni(OH)_2$ catalysts with diverse feed amounts of Ru, including 5, 10, and 15 mg $RuCl_3$ H_2O. (b) the loading mass of Ru species quantified by MP-AES.

With the assistance of MP-AES, the loading mass of varying Ru precursors on NF was measured to be 31.6, 40.6, and 65.8 μg cm^{-2} for 5 mg, 10 mg, and

15 mg Ru precursor used for hydrothermal process, respectively (Figure 4.2 b). As shown in Figure 4.3, To identify the variation in morphology after the hydrothermal process, SEM images for Ni hydroxide with varying feed amounts of Ru precursors were obtained, respectively. It could be discovered that nanosheets were densely and uniformly distributed on the NF substrate, which could facilitate the mass and electron transfer.

As shown in Figure 4.4 a, HRTEM images were further obtained to identify the nanosheet-like morphology and SAED was also conducted to detect the $Ni(OH)_2$ phase, which matched with XRD spectra.

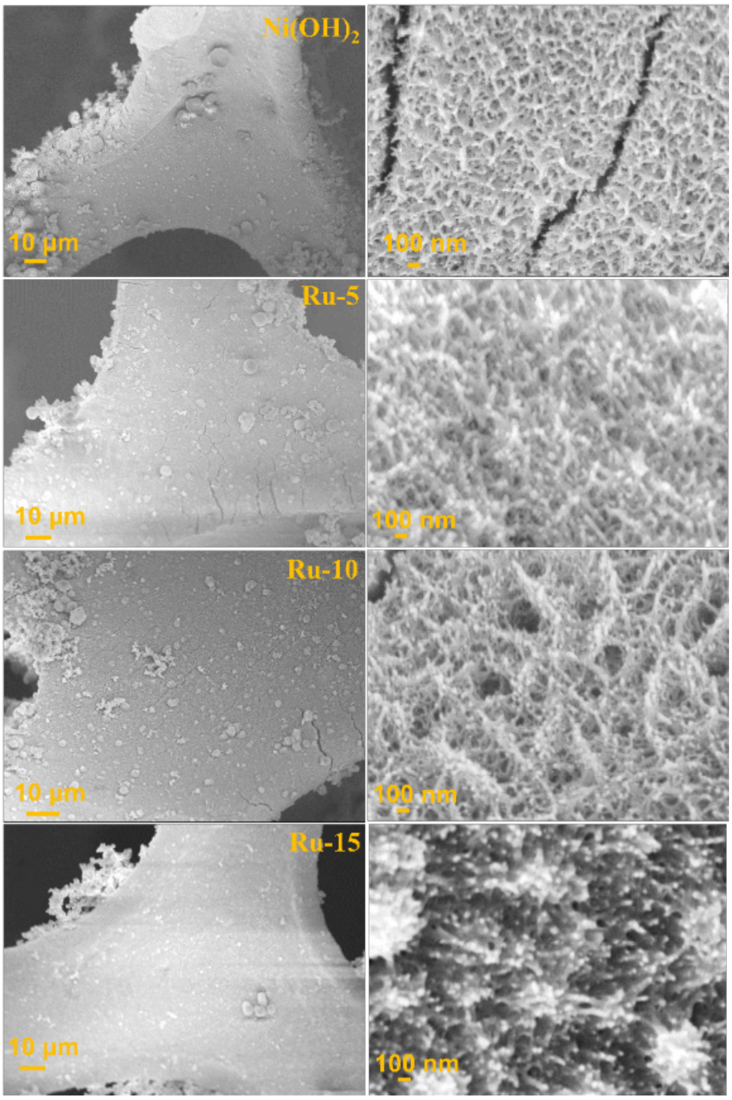

Figure 4.3. Morphologies of $Ni(OH)_2$ and Ru_1-$Ni(OH)_2$ with different feed amounts of Ru source, including 5, 10, and 15 mg $RuCl_3$ H_2O, labelled as Ru-5, Ru-10, and Ru-15, respectively.

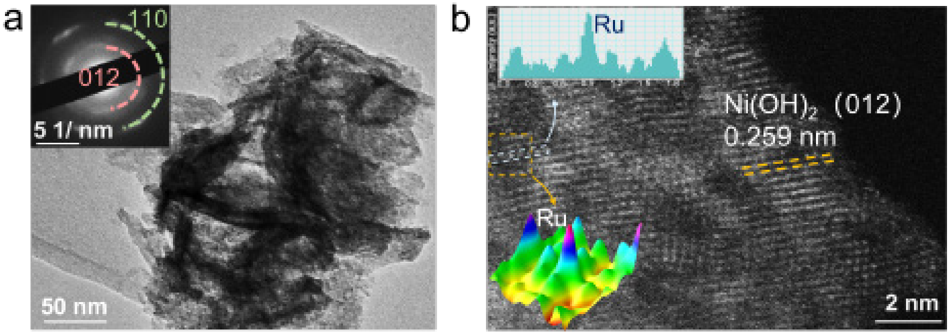

Figure 4.4. (a) Morphology features of Ru$_1$-Ni(OH)$_2$ revealed by HRTEM and corresponding SAED. (b) The HAADF-STEM image of Ru$_1$-Ni(OH)$_2$.

HAADF-STEM was further conducted to identify the Ru site. The lattice spacing distance of 0.259 nm of Ni(OH)$_2$ was first observed (Figure 4.4 b). In addition, the Ru species at the atomic level could be visualized by the local intensity profiles from HAADF-STEM images. The atomically dispersed Ru with higher Z-contrast exhibited brighter spots, which is due to a stronger scattering ability to incident electrons than Ni atoms. The EDS mapping was also performed. The uniform distribution of Ru, Ni, and O elements in Ni hydroxide with atomic Ru site could be discerned (Figure 4.5).

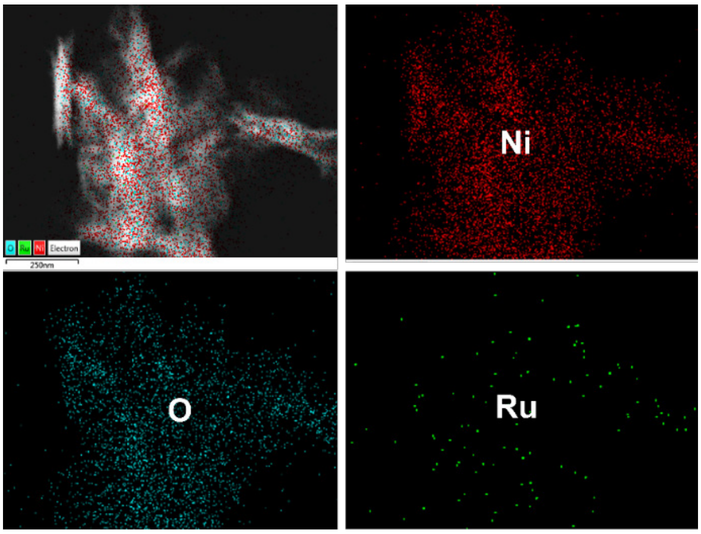

Figure 4.5. EDS mapping of the Ru$_1$-Ni(OH)$_2$ catalyst, including elements of Ni, O, and Ru.

To identify the chemical state and electronic structure, XANES and EXAFS were measured. As shown in Figure 4.6 a, no notable discrepancies in absorption edge position from the Ni K-edge XANES were exhibited between

Ni hydroxide with atomic Ru site and $Ni(OH)_2$ reference. An identical result was also discerned from the EXAFS spectrum (Figure 4.6 b). The above analysis demonstrated that Ni (II) in the form of $Ni(OH)_2$ was the bulk phase of Ni species.

As shown in Figure 4.6 c, the edge peak positions from the Ru K-edge XANES were matched with that of the RuO_2 reference. Ru (IV) was considered the dominant species in Ni hydroxide with atomic Ru site. According to the EXAFS fitting results, the Ru-O scattering distance was 2.05 ± 0.01 Å from the first coordination shell for Ni hydroxide with atomic Ru site (Figure 4.6 d, Figure 4.7, and Table 4.1). It should be noted that this distance was longer than those in the RuO_2 (2 Ru-O bonds with a distance of 1.94 Å and 4 elongated Ru-O with a distance of 1.99 Å). In addition, the coordination number for this Ru-O scattering path was only 4.1 ± 0.3. The above results implied that the Ru species were not in the typical 6-coordinated octahedral coordination geometry.

As for the second coordination shell, as shown in Figure 4.8, the peak position in the Wavelet-transformed EXAFS (WT-EXAFS) for Ni hydroxide with atomic Ru site was located around $k = 7.5$ $Å^{-1}$, while typical Ru-Ru coordination was situated at the k range between 9 - 12 $Å^{-1}$. This finding indicated that the backscatter in this coordination shell should be a lighter atom than Ru.

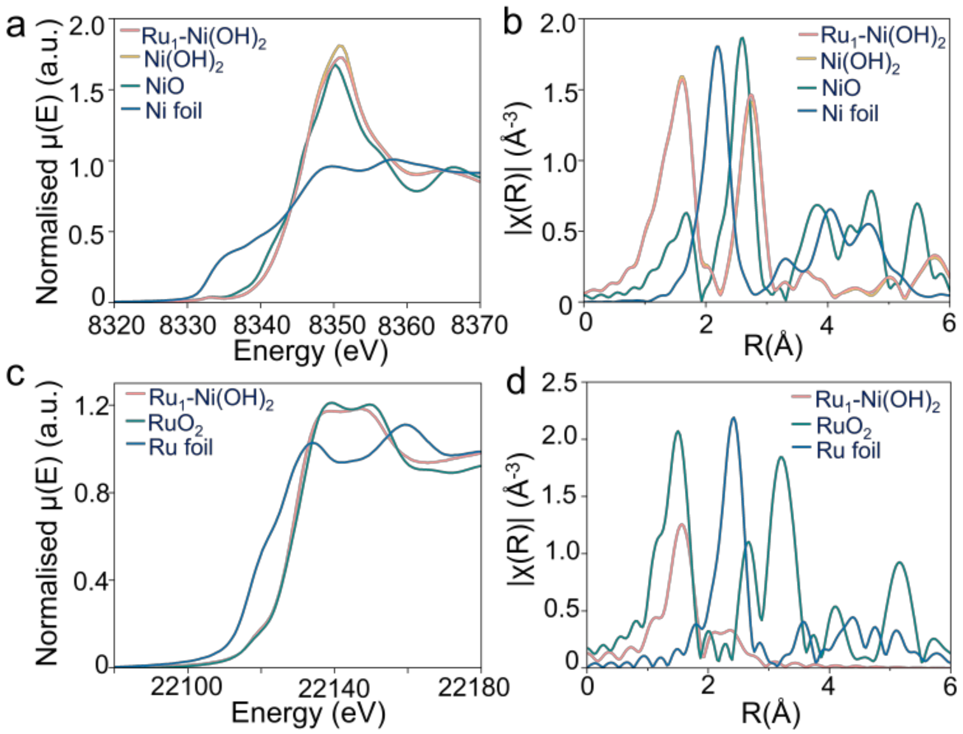

Figure 4.6. Normalized XANES of Ni K-edge for Ru_1-$Ni(OH)_2$, $Ni(OH)_2$, NiO, and Ni foil. d EXAFS of Ni K-edge k^2-weighted R-space for Ru1-$Ni(OH)_2$, $Ni(OH)_2$, NiO (plotted as 1/3 intensity) and Ni foil (plotted as 1/3 intensity). e Normalized XANES of Ru K-edge for Ru_1-$Ni(OH)_2$, RuO_2 and Ru foil. f EXAFS of Ru K-edge k^2-weighted R-space for Ru1-$Ni(OH)_2$, RuO_2 and Ru foil (plotted as 1/2 intensity).

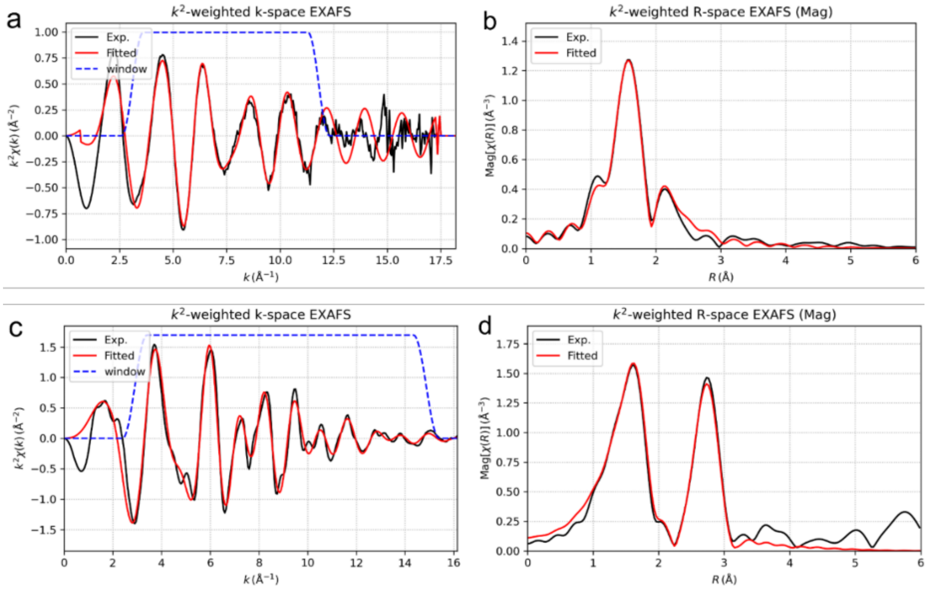

Figure 4.7. Ru K-edge and Ni-K EXAFS fitting results of Ru_1-$Ni(OH)_2$: (a) k^2-weighted k-space EXAFS. (b) k^2-weighted R-space (magnitude) EXAFS.

The experimental data is plotted in black, while the fitted spectrum is plotted in red. Ni-K EXAFS fitting results of Ru_1-$Ni(OH)_2$: (c) k^2-weighted k-space EXAFS. (d) k^2-weighted R-space (magnitude) EXAFS. The experimental data is plotted in black, while the fitted spectrum is plotted in red.

Table 4.1. Fitting results of Ni and Ru K-edge for Ru_1-$Ni(OH)_2$.

Sample	Absorption Edge	Scattering Path	C.N.	R(Å)
Ru_1-$Ni(OH)_2$	Ni K-edge	Ni-O	6.0 ± 0.3	2.05 ± 0.01
		Ni-Ni	6.0 ± 0.3	3.10 ± 0.01
	Ru K-edge	Ru-O	4.1 ± 0.3	2.05 ± 0.01
		Ru-Ni	3.0 ± 0.5	2.70 ± 0.02

C.N. = coordination number; R = interatomic distance.

Moreover, the coordination number of Ru-Ni based on the fitting results was close to 3, indicating that these Ru species were not randomly distributed on the surface of Ni hydroxide. Their coordination environment in the second shell was confined by the lattice structure of Ni hydroxide. According to the analysis based on the coordination number and the bond distances achieved from the spectra of Ru K-edge and Ni K-edge EXAFS, the possibility that the Ru species substitute Ni sites in the $Ni(OH)_2$ structure could be excluded. The above results from spectroscopic studies were in line with the microscopic observation. The dispersion of the atomic Ru species was verified. Therefore, according to the EXAFS results and the crystal structure of $Ni(OH)_2$, it could be deduced that the Ru atoms were anchored on top of the tetrahedral void of Ni hydroxide. In the first and second shells, it was 4 of Ru-O coordination and 3 of Ru-Ni coordination, respectively.

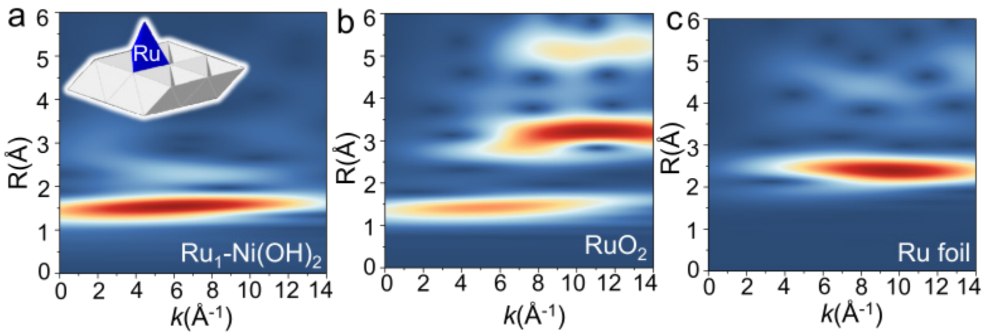

Figure 4.8. k^2-weighted WT-EXAFS for Ru_1-$Ni(OH)_2$, RuO_2 and Ru foil, respectively.

4.4.2 Electrocatalytic performance

After investigation of structural features of Ni hydroxide with atomic Ru site, the UOR performance of Ru_1-$Ni(OH)_2$ catalysts prepared on carbon paper (Ru_1-$Ni(OH)_2$-CP) was first measured in 1 M KOH with 0.33 M urea. As shown in Figure 4.9 a, the Ru_1-$Ni(OH)_2$ catalyst presented higher activity with lower onset potential according to LSV curves. The passivation phenomenon with current collapse emerged at high potentials in LSV curves for Ni hydroxide with and without atomic Ru site. To explore the potential-dependent interfacial electron charge transfer behavior in varying phases, *in situ* EIS investigation during the OER and UOR process was conducted, respectively.

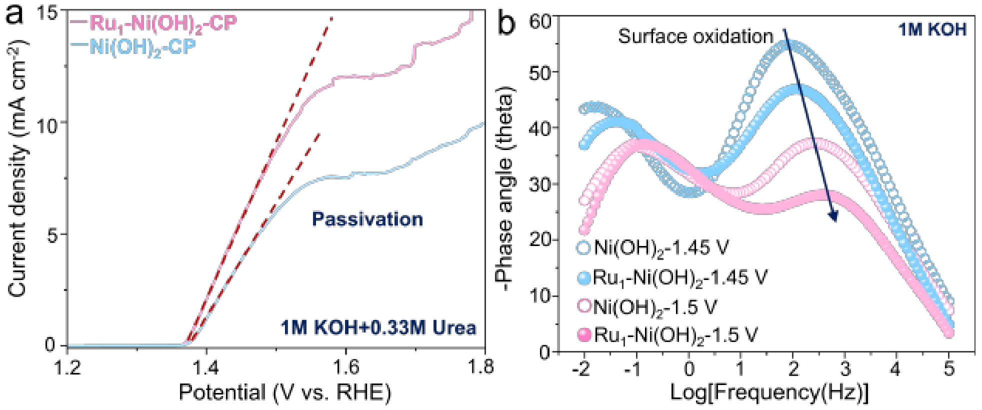

Figure 4.9. (a) LSV curves of as-prepared catalysts on carbon paper. (b) The Bode plot at varying applied potentials.

As shown in Figure 4.9 b, the electrolyte with 1 M KOH was first used to avoid the effect of urea dehydrogenation. The paired peaks from the Bode plot could be discerned at 1.45 V *vs.* RHE. It was worth noting that the phase angle that was found from the high-frequency interface significantly decreased at the potential of 1.5 V *vs.* RHE. This result was attributed to the increase in the reaction rate. The Ni hydroxide with atomic Ru site possessed a smaller phase angle than that of Ni hydroxide. In addition, the diameter of the semicircle in the Nyquist plot was also smaller than that of Ni hydroxide (Figure 4.10 a-c). According to the previous studies[13], the Ni hydroxide would be oxidized to Ni^{3+} species at high frequency during the OER process (Figure 4.11). Thus, Ni hydroxide with atomic Ru site could facilitate the Ni species oxidation reaction to form NiOOH species with a rapid charge transfer rate.

As for the UOR process (Figure 4.12), only one response emerged in the bode plot before 1.5 V *vs.* RHE. Nonetheless, when the potential increased to 1.55 V *vs.* RHE, the phase angle went higher in low frequency. This result was in line with the passivation phenomenon as reported by previous studies[13]. As compared to $Ni(OH)_2$, Ni hydroxide with atomic Ru site possessed a smaller phase angle in the low frequency at high potentials (Figure 4.10 e-h). This could be attributed to the modulation of atomic Ru sites at the electrochemical interface.

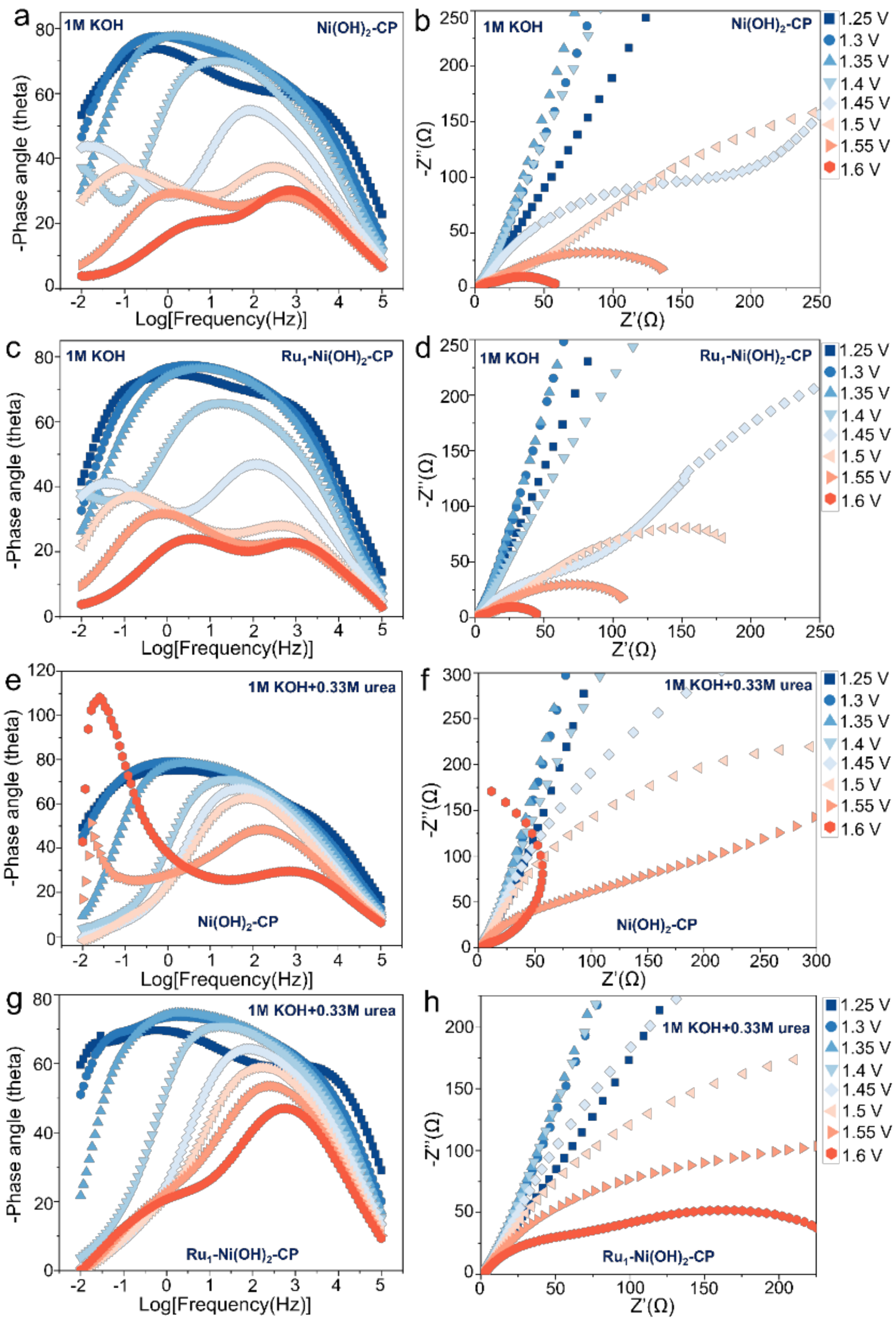

Figure 4.10. *In situ* EIS measurement under varying applied potentials for OER and UOR respectively. (a) Bode plots and (b) Nyquist plots of $Ni(OH)_2$ during the OER process. (c) Bode plots and (d) Nyquist plots for Ru_1-$Ni(OH)_2$ during the OER process. (e) Bode plots and (f) Nyquist plots of $Ni(OH)_2$ during the UOR process. (g) Bode plots and (h) Nyquist plots of Ru_1-$Ni(OH)_2$ during the UOR process.

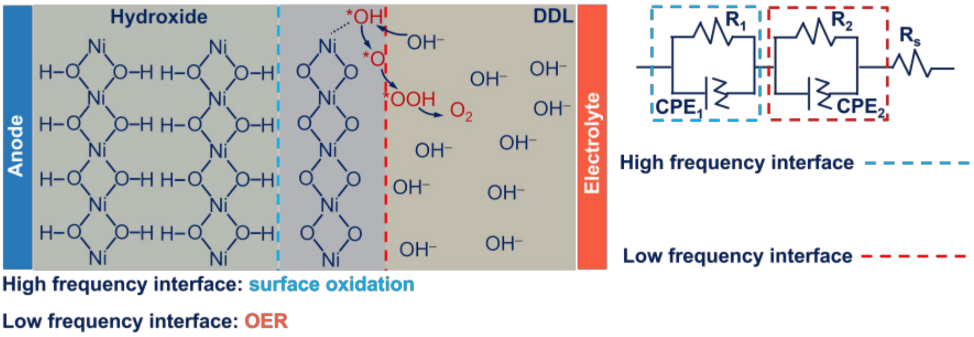

Figure 4.11. The interfacial electron charge transfer behavior in varying phases during the OER process.

Additionally, the interfacial adsorption of OH^- species could influence the electrochemical step with the formation of NiOOH species[21, 22]. It was recognized that the adsorption energy of OH^- on Ni hydroxide with atomic Ru site (-0.98 eV) is relatively higher than that of Ni hydroxide (-0.56 eV), probably indicating a strong OH^- adsorption to boost the surface oxidation process (Figure 4.13).

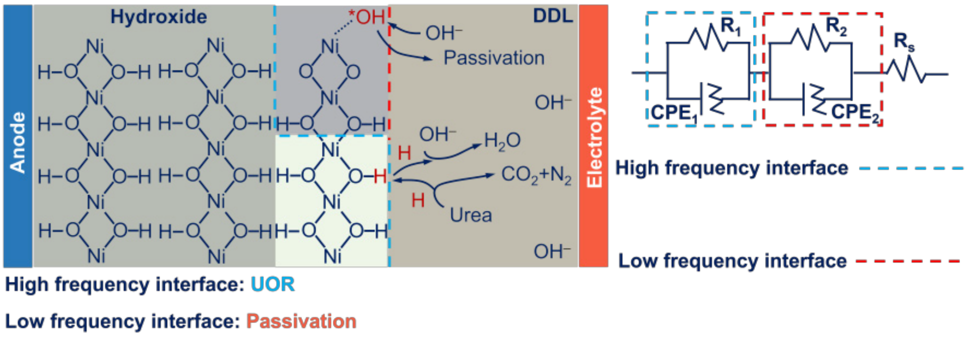

Figure 4.12. The interfacial electron charge transfer behavior in varying phases during the UOR process.

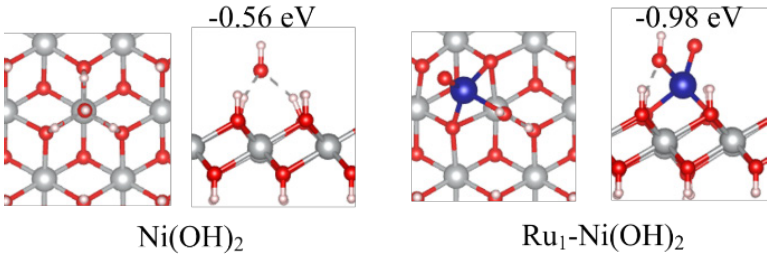

Figure 4.13. The adsorption energy of OH^- on Ni hydroxide with and without atomic Ru site.

The powder catalysts prepared on carbon paper suffered from insufficient access to the electrolyte and activity degradation due to the catalysts falling off from the substrate. Therefore, the self-standing catalyst direct synthesis on NF with 3D porous structures was used to evaluate the electrochemical performance due to more exposure to active sites. It was worth noting that the passivation phenomenon could not be discerned from the LSV curve of Ru_1-$Ni(OH)_2$ on the nickel foam (Ru_1-$Ni(OH)_2$-NF) (Figure 4.14 a). However, the passivation issues with current depletion could still be observed for $Ni(OH)_2$-NF.

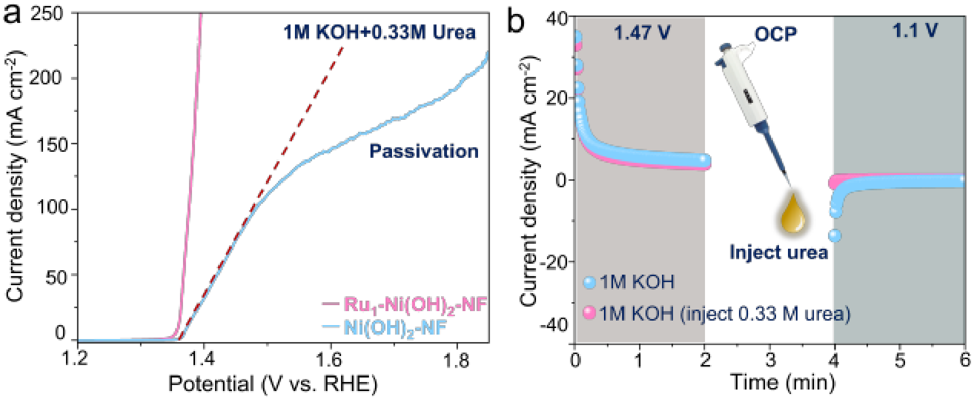

Figure 4.14. (a) Polarization curves of as-prepared catalysts on nickel foam. (b) Intermittent test under different applied potentials.

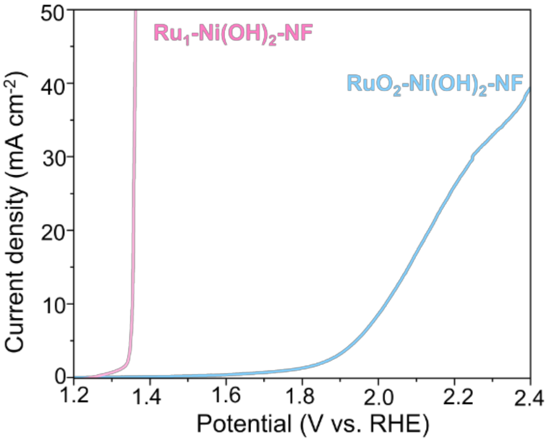

Figure 4.15. Polarization curves of Ru_1-$Ni(OH)_2$ and RuO_2-$Ni(OH)_2$ catalysts during the UOR process.

To identify the electrochemical process of the UOR, the intermittent UOR test was carried out by separating the process of electrochemical step to form

Ni^{3+} active sites and the urea dehydrogenation (Figure 4.14 b). An oxidation current related to the formation of NiOOH species was first discerned in 1M KOH at 1.47 V *vs.* RHE for 2 mins. The electrolyte containing urea was then added at open circuit potential (OCP). It could be discerned that no reduction current was observed at 1.1 V *vs.* RHE. However, a significant reduction current was found at the same applied potential when no urea was added. This result indicated that the electrogenerated NiOOH species could accept protons from urea at OCP and High Ni^{3+} would be reduced to Ni hydroxide spontaneously, and thus no reduction current could be discerned. RuO_2 with typical Ru-O_6 coordination configuration was further leveraged by drop-casting on $Ni(OH)_2$-NF as the control sample. The onset potential of Ru-O_6/$Ni(OH)_2$-NF to drive UOR was 1.8 V *vs.* RHE, which possessed poor UOR activity compared to Ru_1-$Ni(OH)_2$-NF (Figure 4.15).

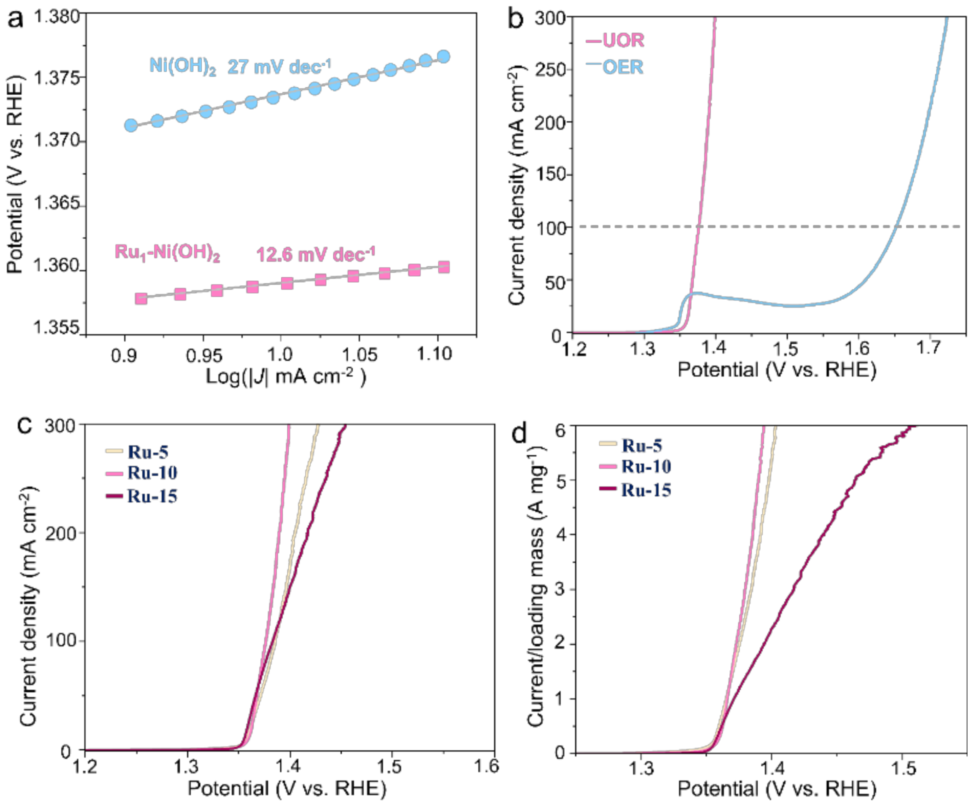

Figure 4.16. (a) Tafel slopes. (b) LSV curves of Ru_1-$Ni(OH)_2$ catalysts during UOR and OER. (c) LSV curves of Ru_1-$Ni(OH)_2$ with different amounts of Ru source. (d) The ratios between current and loading mass of different feed amounts of Ru source.

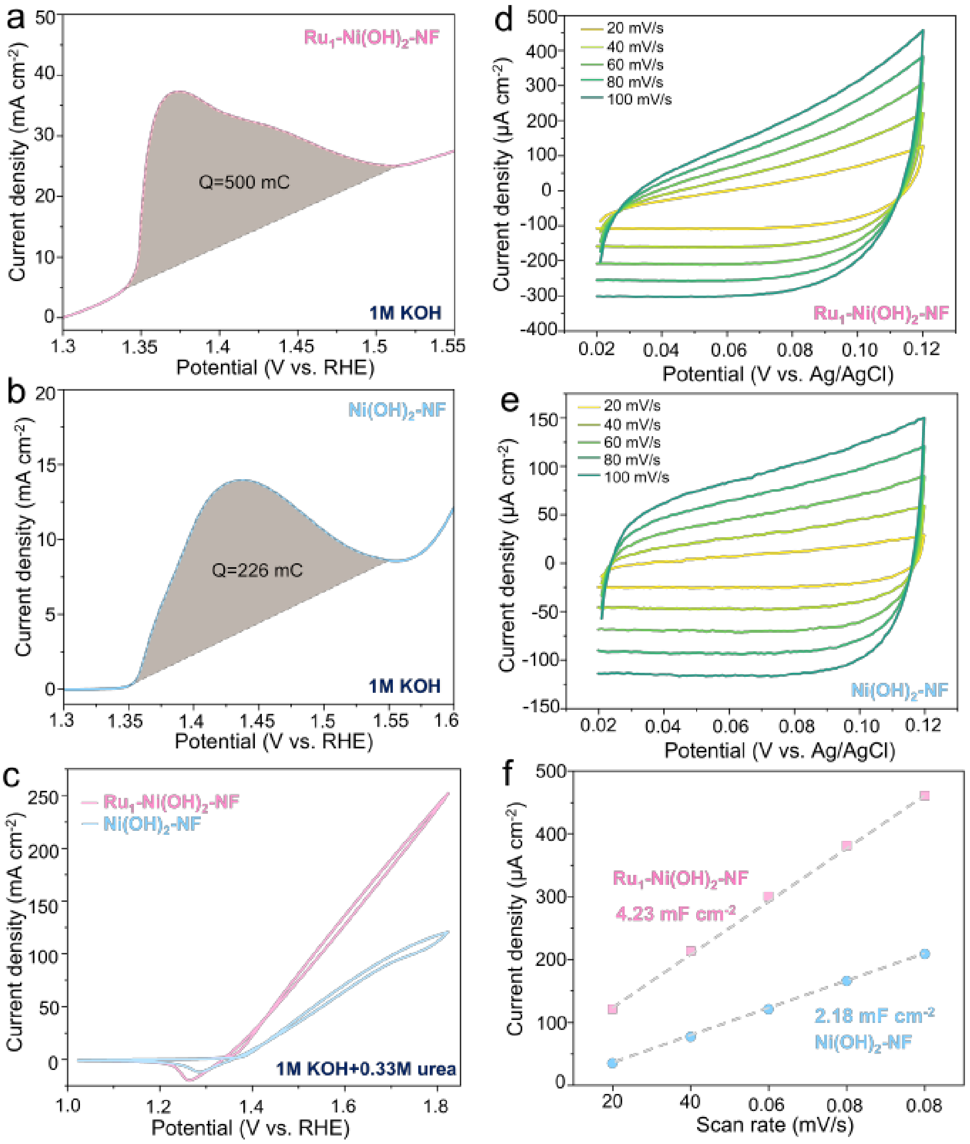

Figure 4.17. The investigation of the dynamic Ni^{3+} active site generation ability. (a-b) integrated Ni^{2+} to Ni^{3+} oxidation peak of Ru_1-$Ni(OH)_2$-NF and $Ni(OH)_2$-NF, respectively. Q is the faradaic charge transfer of Ni^{2+} to Ni^{3+} and the value can be calculated by the equation: $Q = S/v$, where S represents the integrated mathematical area (yellow shadow), v is the scan rate (5 mV/s). (c) CV curve of Ru_1-$Ni(OH)_2$ and $Ni(OH)_2$ catalysts on nickel foam in the electrolyte of 1M KOH +0.33M urea. (d-e) CV scanning curves at various scan rates in the non-Faradaic potential region. (f) Capacity current density at 0.07 V vs. Ag/AgCl as functional of scan rate (data obtained from d and e).

Only 1.37 V *vs.* RHE was required to drive 100 mA cm^{-2} for the Ru_1-$Ni(OH)_2$-NF catalysts. In addition, a much smaller Tafel slope of 12.6 mV dec^{-1} was discerned, indicating favorable UOR kinetics (Figure 4.16 a). Moreover, the potential at 100 mA cm^{-2} was negatively shifted by 282 mV as compared to the OER as shown in Figure 4.16 b. The feed amount of Ru precursor (10 mg) exhibited the optimal ratio between current and loading mass, which was 6 A mg^{-1} at 1.39 V *vs.* RHE (Figure 4.16 c and d), indicating a high potential for practical applications.

To unearth the effect of atomic Ru sites on Ni^{3+} active species formation, the faradaic charge transfer for Ni^{2+} to Ni^{3+} was investigated in 1 M KOH to avoid the impact of urea dehydrogenation (Figure 4.17 a and b). The Ni hydroxide with atomic Ru site possessed a higher faradaic charge of Ni^{3+} generation as compared to Ni(OH)$_2$-NF.

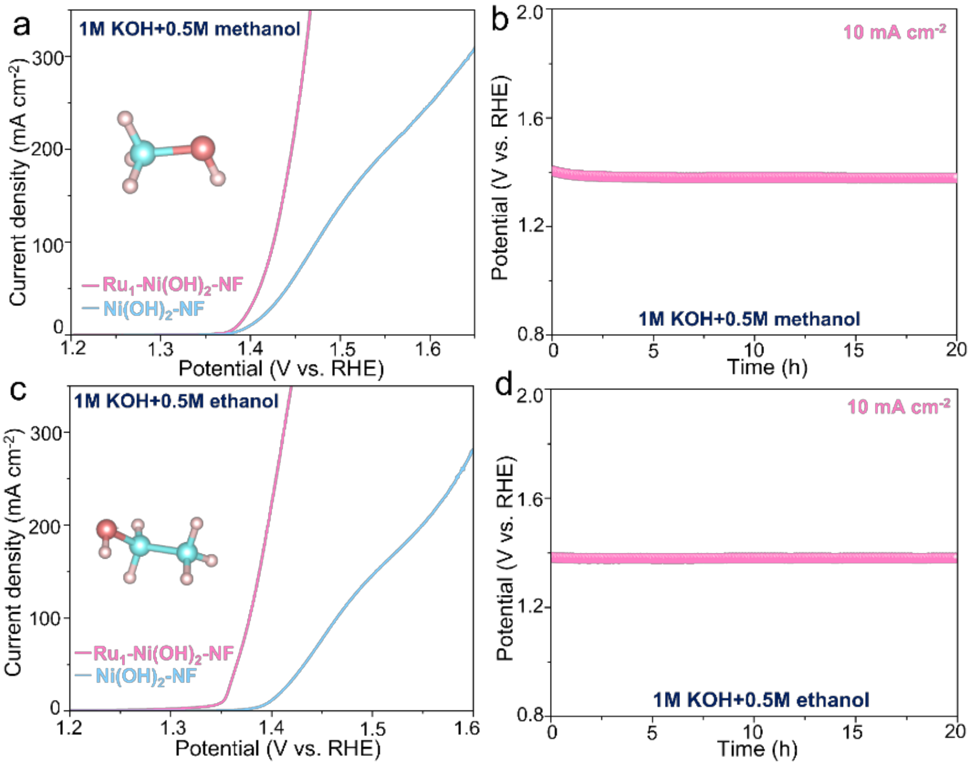

Figure 4.18. (a)-(b) Polarization curves and durability test of MOR and (c)-(d) EOR.

Moreover, It was found that the oxidation peak of Ni^{2+} to form Ni^{3+} overlapped with the UOR region due to the nearly identical onset potential for the electrochemical step and UOR. The variance in reduction peaks of Ni^{3+} to Ni^{2+} could be discovered. Ni hydroxide with atomic Ru site showed a relatively negative shift and higher intensity according to the CV plot, indicating sufficient Ni^{3+} species when introducing atomic Ru sites (Figure 4.17 c).

Furthermore, as shown in Figure 4.17 d-f, the C_{dl} of Ru_1-$Ni(OH)_2$-NF was measured with 4.23 mF cm^{-2}, almost two times higher than that of $Ni(OH)_2$-NF, indicating sufficient active sites with the incorporation of atomic Ru sites. It was worth noting that the Ni hydroxide with atomic Ru site also presented high activity and stability for other organic compound oxidation reactions, such as methanol and ethanol oxidation reactions (Figure 4.18). The durability tests at 10 and 100 mA cm^{-2} over 200 and 100 hours were carried out to evaluate the stability of as-prepared catalysts. Almost no notable increase in potential could be observed during the durability test (Figure 4.19).

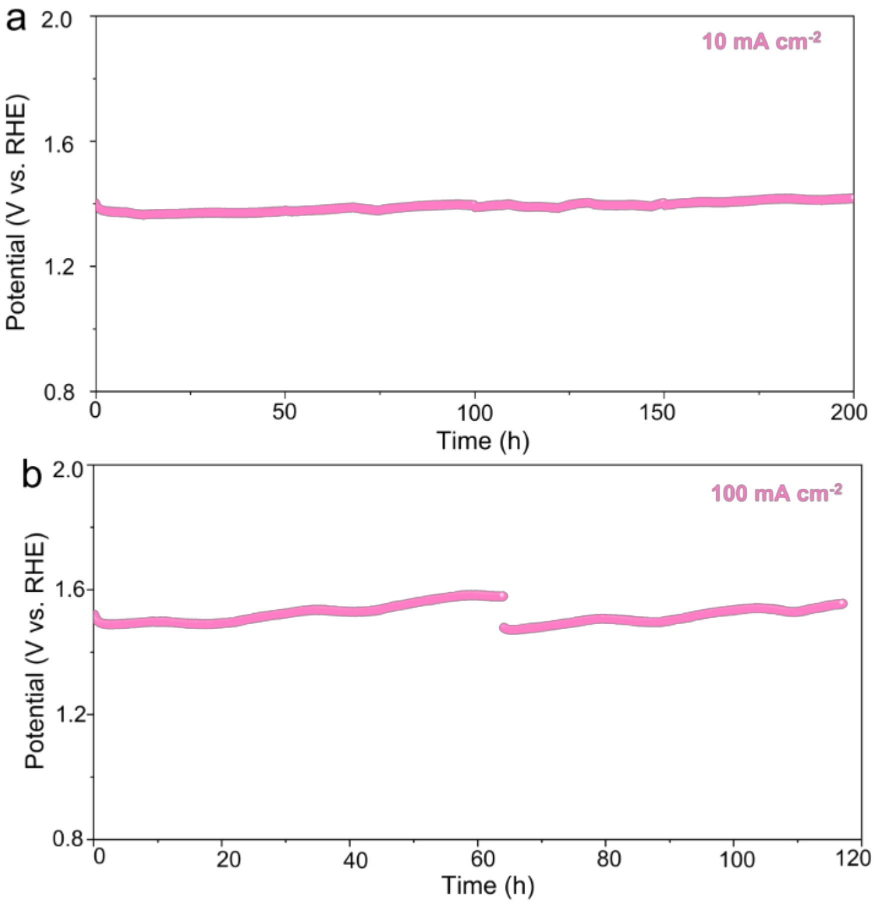

Figure 4.19. (a)-(b) Durability test at 10 and 100 mA cm^{-2} during the test over 200 and 100 hours.

4.4.3 Identification of the role of atomic Ru sites

To unearth the reaction microenvironments during the OER and UOR process and obtain real-time evolution from the electrochemical interface, *In situ* Raman measurement with a laser wavelength of 532 nm was carried out to figure out the reaction microenvironment during the UOR process (Figure 4.20).

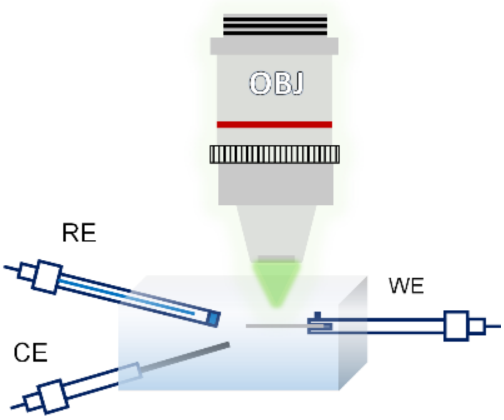

Figure 4.20. The setup of *In situ* Raman spectra measurement.

The evolution of active NiOOH species could be revealed by *in situ* Raman observations. Specifically, as shown in Figure 4.21 a and b, two peaks located at 474 and 553 cm^{-1}, were discerned at 1.42 V *vs.* RHE for Ni hydroxide with atomic Ru site, which corresponded to the bending and stretching vibration mode of Ni^{3+}–O in NiOOH active species.[23] When the applied potential went back to OCP, the peaks of Ni^{3+} species could not be found, suggesting that the NiOOH species could be reduced to Ni hydroxide by capturing protons from urea at OCP, which matched with the above results of intermittent UOR test (Figure 4.14 b). As shown in Figure 4.21 c and d, the peaks for Ni^{3+} species were discerned at 1.37 V *vs.* RHE during the OER process. It was worth noting that the peaks of Ni^{3+} species emerged until 1.42 V *vs.* RHE during the UOR process. This result implied that protons from the urea dehydrogenation reaction would intercalate into the NiOOH site and inhibit the generation of Ni^{3+} species.

As shown in Figure 4.22, a 30-minute operation test at the applied potential to 1.37 V *vs.* RHE was conducted. The accumulated Ni^{3+} species could not be promptly reduced by urea to Ni^{2+}, thus leading to the accumulation of NiOOH. Accordingly, accumulated NiOOH species could be discerned as time evolved with continuous urea consumption and limited mass transfer. Therefore, the UOR rate in low urea concentration is limited by urea dehydrogenation.

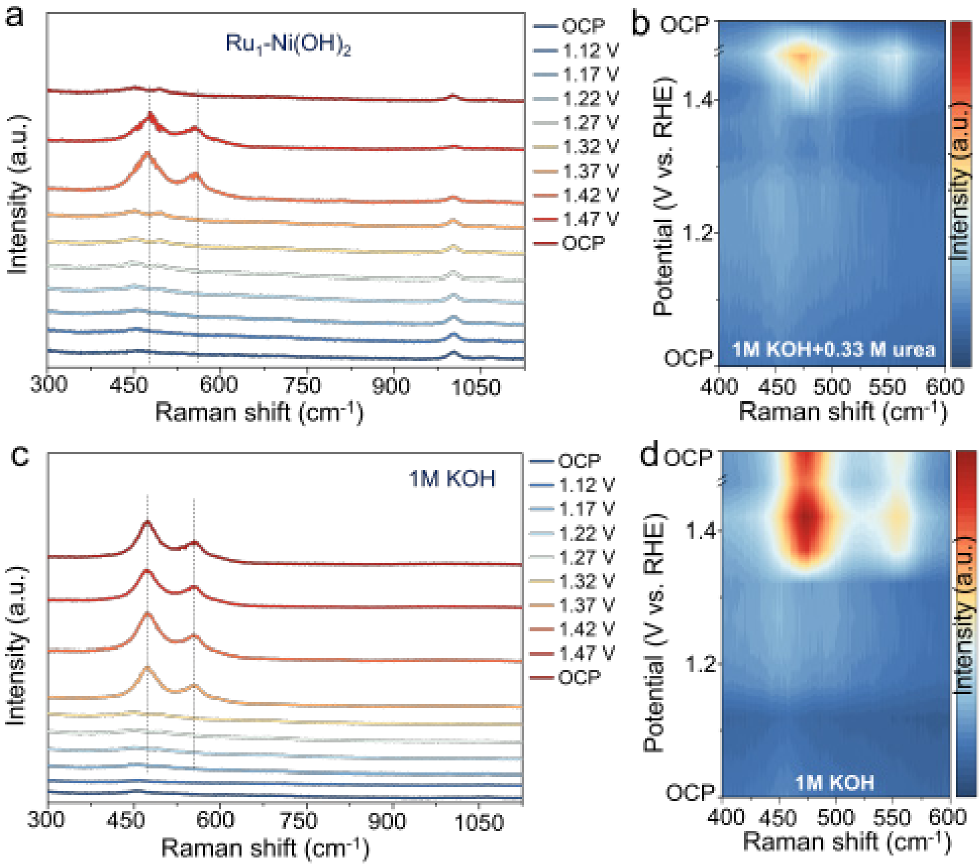

Figure 4.21. Raman measurement for UOR (a)-(b) and OER (c)-(d).

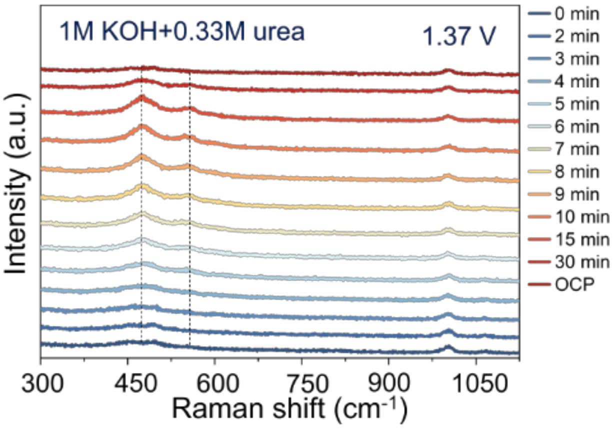

Figure 4.22. Raman spectra during the half-hour urea electrolysis at 1.37 V *vs.* RHE.

Moreover, it was discovered that the high concentration of urea (2M) could inhibit the formation of NiOOH species without the presence of peaks of

NiOOH emerging from Raman spectra throughout the applied potential window (Figure 4.23).

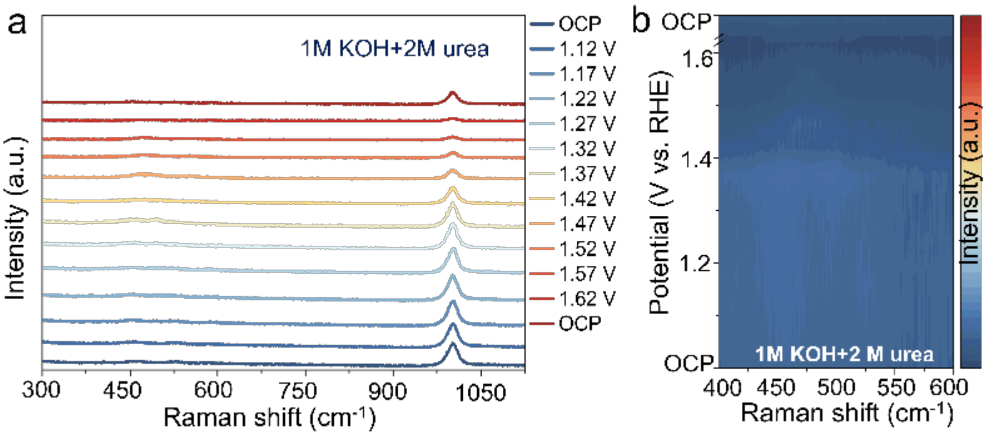

Figure 4.23. (a)-(b) Raman spectra during the UOR with a high concentration of urea (2M).

To reveal the Ni site evolution during the intermittent test, the assistance of Raman measurement was carried out. The Ni^{3+} species were first obtained from electro-generation in 1 M KOH at 1.47 *vs.* RHE over 600 s. After changing the electrolyte with 1M KOH + 2 M urea at OCP, the NiOOH species could rapidly be reduced without the characterized peak of Ni^{3+} (Figure 4.24). This result demonstrated that the accumulation of NiOOH species was inhibited, thus affecting the sustained UOR activity with the limit of the active NiOOH generation. This trend could further be verified from the Raman spectra during the methanol and ethanol oxidation reactions (Figure 4.25).

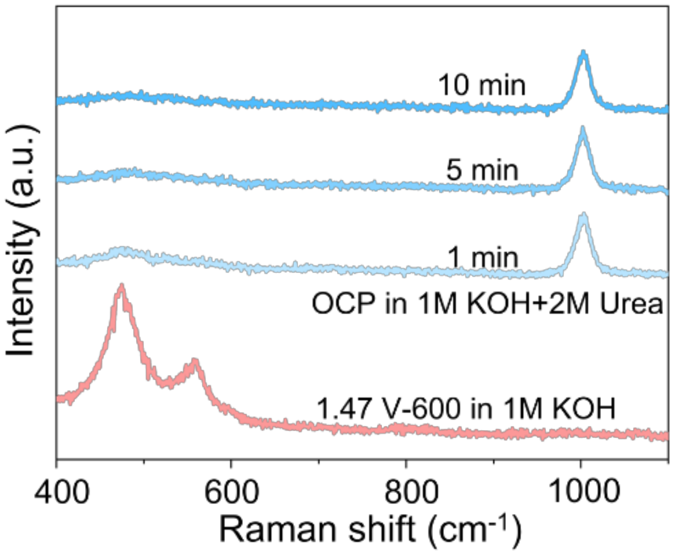

Figure 4.24. Raman spectra of the intermittent test.

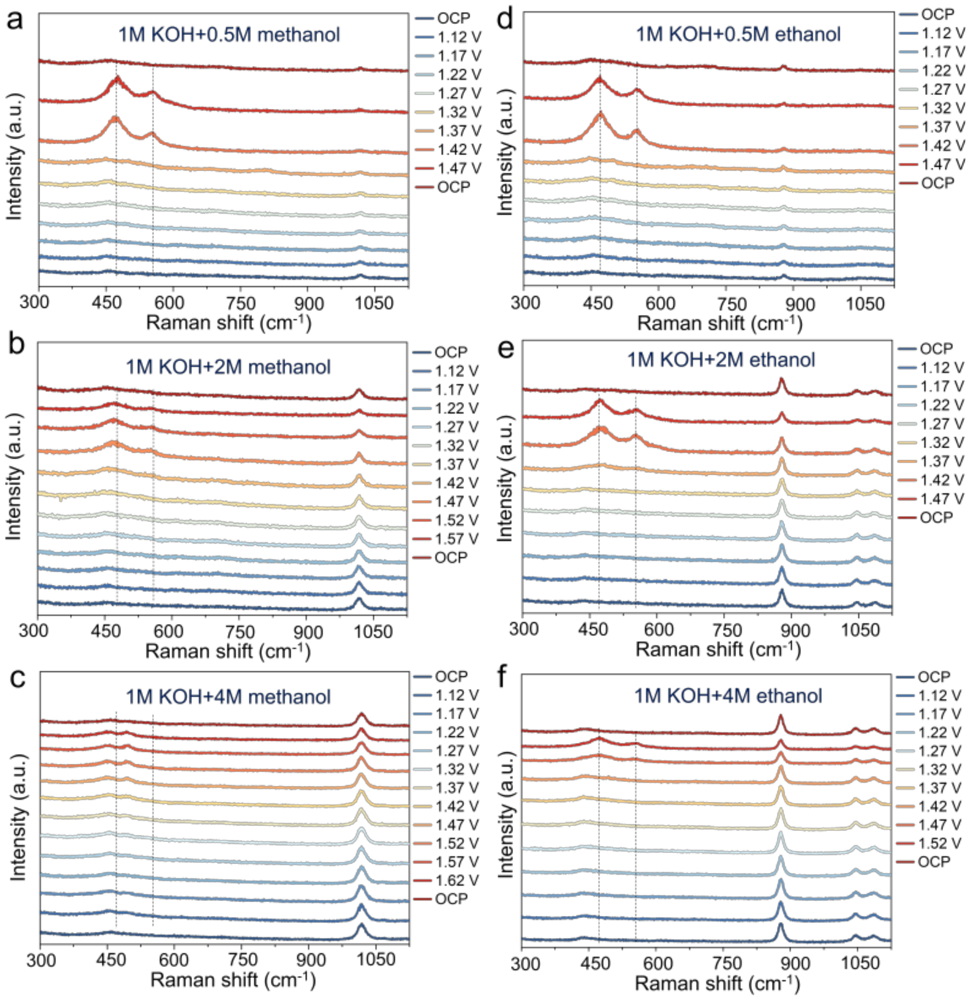

Figure 4.25. Raman spectra of MOR and EOR in different concentrations.

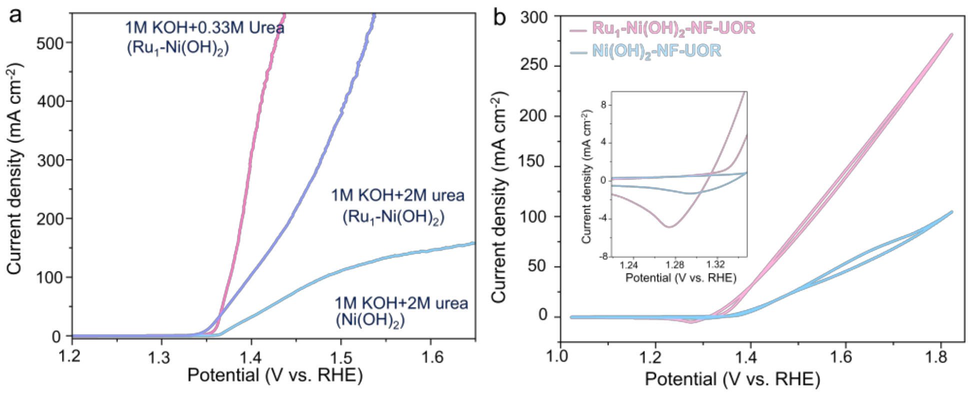

Figure 4.26. (a) LSV curves during the UOR in low and high urea concentrations. (b) CV curve of Ru_1-$Ni(OH)_2$ and $Ni(OH)_2$ catalysts on nickel foam in the electrolyte of 1M KOH + 2M urea.

As shown in Figure 4.26, Ni hydroxide with atomic Ru site still presented a lower potential to reach the current density over 100 mA cm^{-2} in high urea concentration. In addition, the variance in reduction peaks of Ni^{3+} to Ni^{2+} could be discovered. Ni hydroxide with atomic Ru site showed a relatively negative shift and higher intensity according to the CV plot, indicating that introducing atomic Ru sites could still enable the abundant Ni^{3+} species in high urea concentration. Despite the suppression of active Ni^{3+} generation in high urea concentrations, high UOR activity could still be maintained with the modification of atomic Ru sites.

To identify the stability of Ru sites after reactions, the Ni hydroxide with atomic Ru site after 20 cycles of CV during the OER and UOR process was characterized with XPS measurement, respectively (Figure 4.27 a). According to the XPS spectra of Ru $3p_{3/2}$, the peak situated at 463.2 eV can be ascribed to Ru (IV), which matched with the spectra of Ru K-edge XANES. Moreover, the lower intensity of Ru $2p_{3/2}$ after OER could be discerned as compared with pristine samples. In contrast, the Ni hydroxide with atomic Ru site characterized after UOR still exhibited a high intensity of Ru (IV) peak without significant shift as shown in Figure 4.27 b, indicating good structure stability during the UOR process.

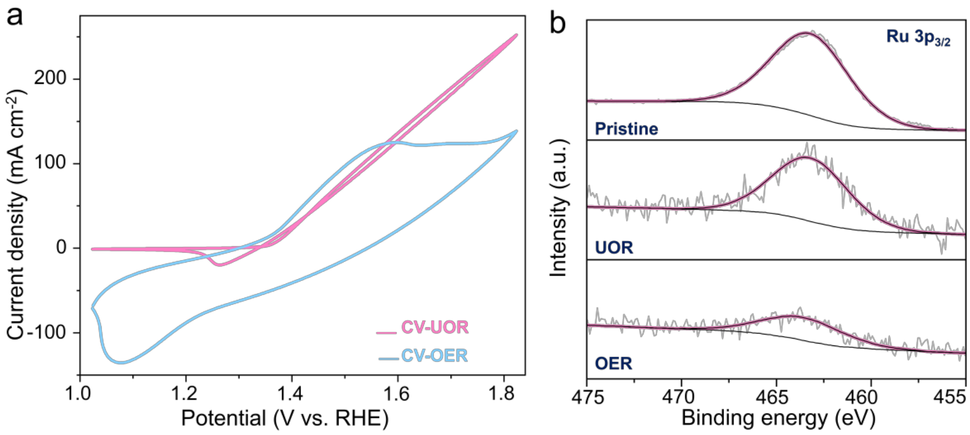

Figure 4.27. The investigation of the Ru sites after the reaction. (a) CV curves after 20 cycles. (b) XPS spectra of Ru $3p_{3/2}$.

The flower-liked spheres with the agglomeration of the nanosheets could be discovered from the morphology of the electrode that was collected after OER.

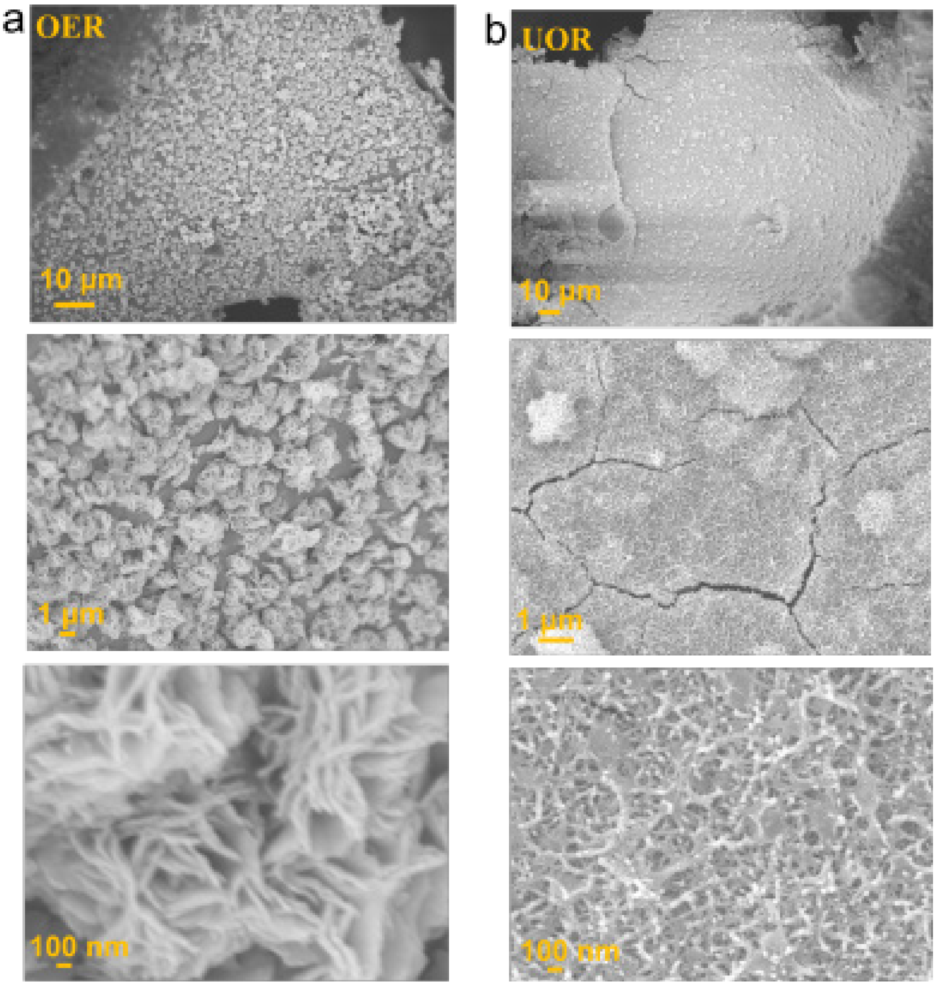

Figure 4.28. The morphology after the CV test during (a) OER and (b) UOR.

The open and porous structure could facilitate the OH^- attack on the atomic Ru sites under an alkaline medium, leading to undesirable metal dissolution. However, the morphology with nanosheet could be maintained after UOR as shown in Figure 4.28. The urea dehydrogenation process was able to suppress the continuous NiOOH accumulation, thus avoiding undesirable structural reconstruction.

Except for experimental studies, DFT calculations were carried out based on the NiOOH model to further unearth the role of single atomic Ru. Bader charge variance between the NiOOH and Ru_1-NiOOH implied that Ni atoms would be harder to lose electrons with the presence of single atomic Ru sites, thus possessing an electron-enriched state as shown in Figure 4.29. Differential charge density further exhibited an electron depletion region (green region) around the atomic Ru site. It was suggested that the positive region can facilitate the adsorption of 'electron-donating' groups (–NH_2) in urea molecules. The 'electron-withdrawing' groups (C=O) would preferentially be adsorbed on negative region[12]. Therefore, the redistributed charge density of metal sites could modulate electron transfer with the incorporation of a single atomic Ru site, which was favorable for urea dehydrogenation.

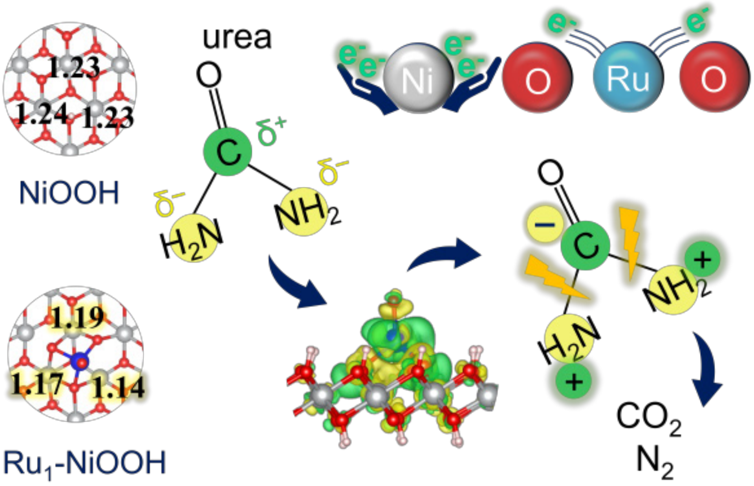

Figure 4.29. The DFT calculations include Bader charges and charge density difference for Ru_1-$Ni(OH)_2$.

4.4.4 Applications in the energy conversion system

To estimate the applicability of Ni hydroxide with atomic Ru site to replace OER with UOR in the energy conversion scenarios, the cycling test of zinc-air battery and zinc-urea-air battery was first carried out. The charging process for Zn-air batteries encompassed the OER and the reduction of Zn^{2+} in the positive and negative electrodes, respectively. As for the Zn-urea-air battery, the OER would be substituted by the UOR. As shown in Figure 4.30, the charging voltage obtained from the polarization curve could be reduced after adding urea to the electrolyte. Moreover, the stability test conducted with the cycling measurement over 100 hours showed about a 200 mV reduction in the charging voltage than that of the Zn-air battery (Figure 4.31).

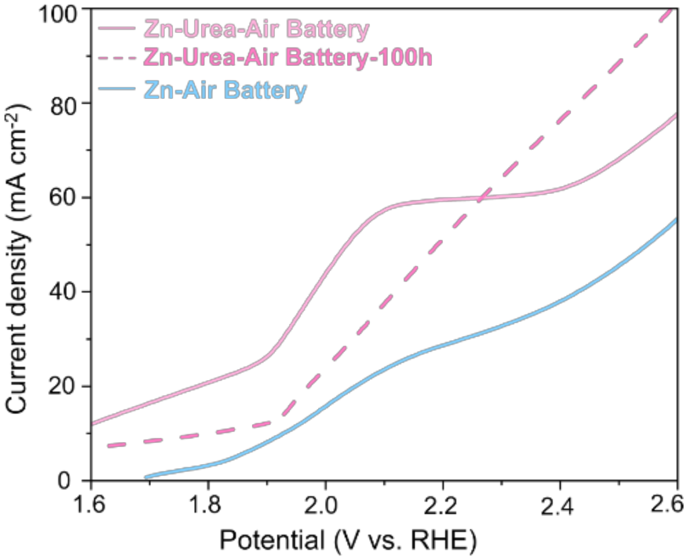

Figure 4.30. Charging curves of the Zn-battery and Zn-urea-air battery before and after the 100-hour test.

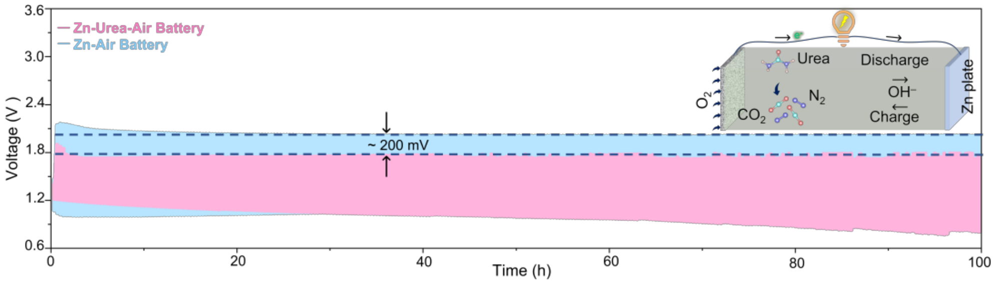

Figure 4.31. Electrochemical measurement for Zn-air battery and Zn-urea-air battery under the current density of 5 mA cm^{-2}.

In addition, LSV curves were collected by the two-electrode electrolyzers to validate the ability of urea-assisted water electrolysis. To prepare suitable HER electrodes, Ni hydroxide with atomic Ru site was further phosphorized to form heterogeneous Ni phosphides to elevate the electrical conductivity. As shown in Figure 4.32, the heterogeneous Ni phosphide catalyst was obtained, including two phases of Ni_2P and $Ni_2P_4O_{12}$. Promising HER performance with high activity and stability could be detected as compared to the commercial Pt/C benchmark electrode (Figure 4.33 and 4.34).

LSV curves were collected by the two-electrode electrolyzers (Figure 4.35). The notable variance in current density at varying applied cell voltage of 1.5 V, 1.6 V, and 1.8 V could be found, which was 2.2-fold, 2.5-fold, and 2.2-fold higher than that of HER-OER.

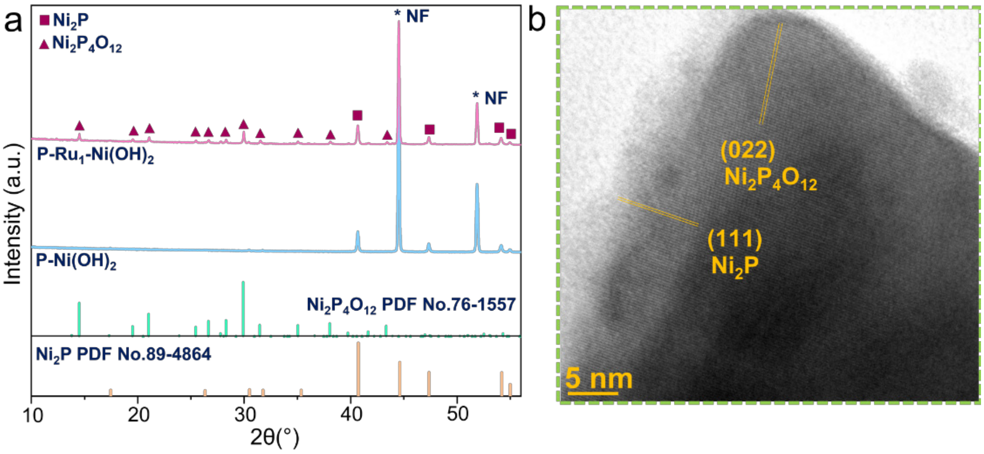

Figure 4.32. (a) The XRD pattern of as-synthesized heterogeneous Ni phosphides. (b) HR-TEM image.

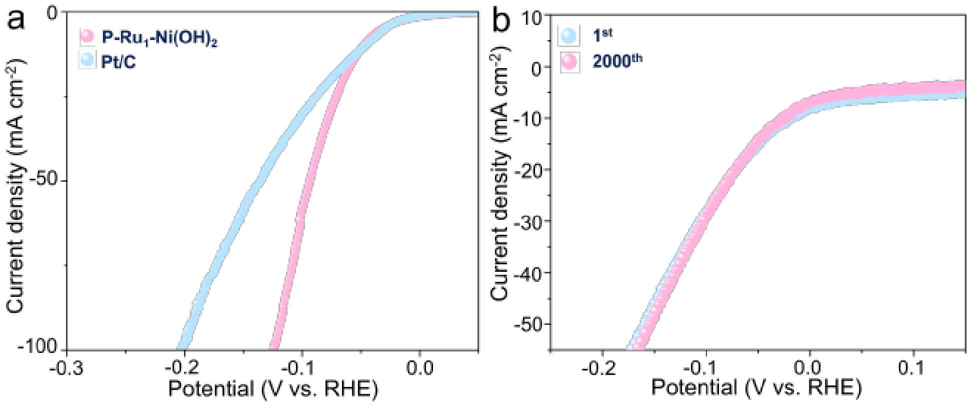

Figure 4.33. HER performance of the heterogeneous catalysts of Ni phosphides catalysts. (a) LSV curves. (b) LSV curves after 2000th cycling.

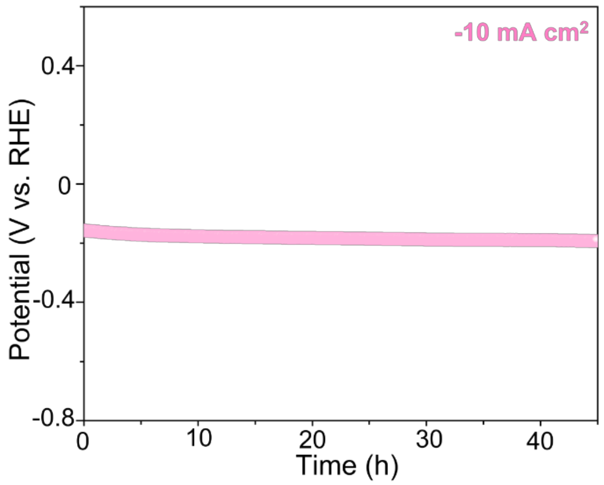

Figure 4.34. Stability test over 45 hours.

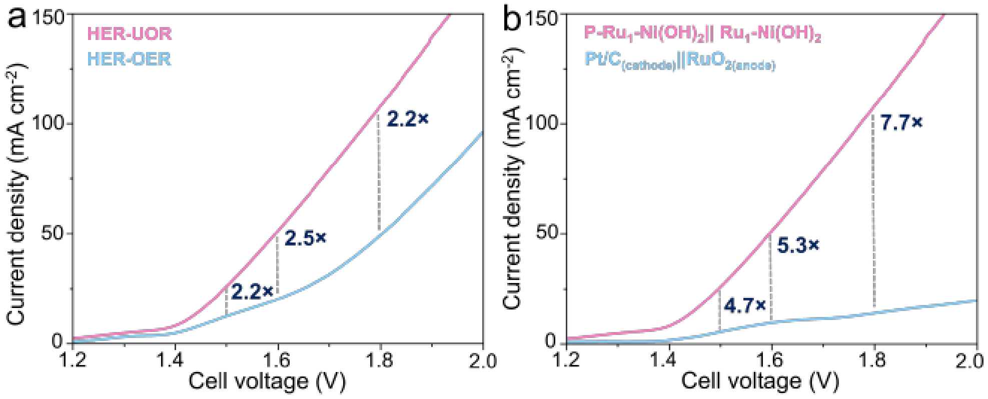

Figure 4.35. (a) LSV curves of two-electrode for HER-UOR and HER-OER. (b) LSV curves of two-electrode for comparison with the benchmark.

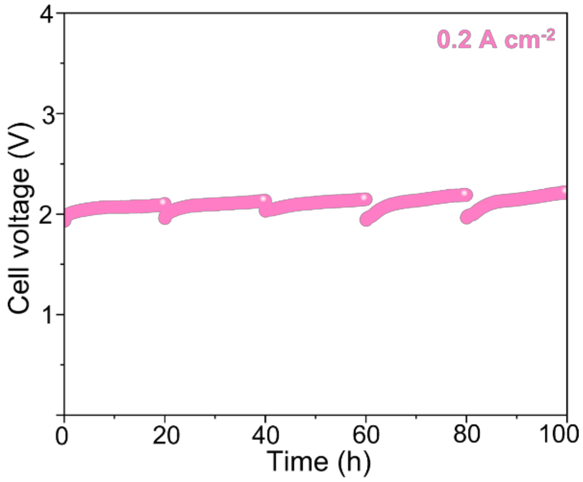

Figure 4.36. Stability test under 0.2 A cm^{-2} over 100 h (adding fresh electrolyte every 20 h).

The current density exhibited 4.7-fold, 5.3-fold, and 7.7-fold higher than that of the benchmark catalysts (Pt/C and RuO_2). Furthermore, a durability test was conducted to evaluate the stability of urea-assisted water electrolysis. No notable increase in cell voltage over 10 h at 200 mA cm^{-2} could be found (Figure 4.36).

The MEA test was carried out to estimate the applicability of urea-assisted water electrolysis under varying industrial-level current densities. The durability test was performed at 0.2, 0.5, and 1A cm^{-2} for over 400 h. It was worth noting that no notable activation degradation could be discerned (Figure 4.37).

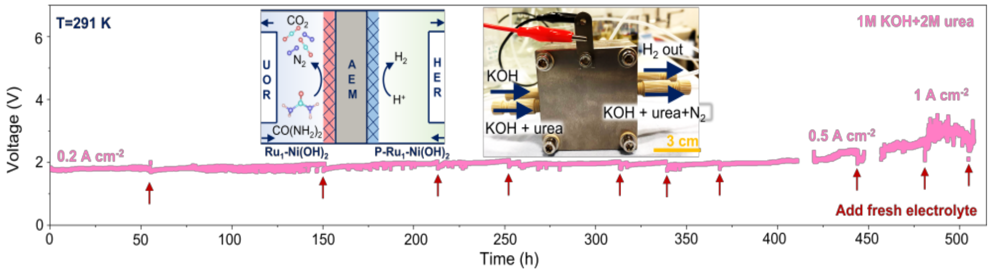

Figure 4.37. MEA system test to validate urea-assisted water electrolysis under varying current densities.

4.5 Conclusion

The noble metal-doped Ni catalysts were proposed with an atomic heterostructure engineering strategy. To modify the Ni-based catalyst to generate abundant active sites, a Ru-O_4 coordinated configuration anchored on Ni hydroxide catalysts with a low Ru loading mass of 40.6 μg cm^{-2} was proposed by hydrothermal method to facilitate the adsorption of OH^- to boost the electrochemical step to form abundant Ni^{3+} active sites. In addition, the critical roles of urea dehydrogenation and Ni oxidation in both low and high urea concentrations were unveiled by *in situ* spectroscopy observation and DFT calculations. Under the condition of low urea concentration, the electrochemical step for NiOOH species formation proceeded more rapidly than the urea dehydrogenation process. As for high urea concentration, the accumulation of NiOOH species was inhibited. Ni hydroxide with atomic Ru site could still maintain higher activity with sufficient Ni^{3+} species than Ni hydroxide. The 100 h Zn-urea-air battery operation and over 400 h urea-assisted water electrolysis in MEA test under varying industrial-level current densities demonstrated a high potential for UOR to replace OER in various energy conversion scenarios. The modulation brought by the atomic Ru sites at the electrochemical interface opens a new avenue for the modification of Ni-based materials, inspiring the subsequent design of high-performance Ni-based UOR catalysts and other organic compound oxidation reactions. The discoveries in this chapter also empower the development of electrocatalysts for practical applications.

4.6 References

1. X. Wu; Y. Wang; Z.-S. Wu. *Chem*, **2022**, *8*, 2594-2629.
2. J. Li; H. Li; K. Fan; J. Y. Lee; W. Xie, *et al. Chem Catal*, **2023**, *3*, 100638.
3. B. Zhu; B. Dong; F. Wang; Q. Yang; Y. He, *et al. Nat Commun*, **2023**, *14*, 1686.
4. X. Xu; Q. Deng; H.-C. Chen; M. Humayun; D. Duan, *et al. Research*, **2022**, *2022*, 7124.
5. Y. Zhu; C. Liu; S. Cui; Z. Lu; J. Ye, *et al. Adv Mater*, **2023**, *35*, e2301549.
6. M. Cai; Q. Zhu; X. Wang; Z. Shao; L. Yao, *et al. Adv Mater*, **2023**, *35*, e2209338.
7. P. Wang; X. Bai; H. Jin; X. Gao; K. Davey, *et al. Adv. Funct. Mater.*, **2023**. *33*, 2300687.
8. W. K. Han; J. X. Wei; K. Xiao; T. Ouyang; X. Peng, *et al. Angew Chem Int Ed Engl*, **2022**, *61*, e202206050.
9. L. Zhang; L. Wang; H. Lin; Y. Liu; J. Ye, *et al. Angew Chem Int Ed Engl*, **2019**, *58*, 16820-16825.
10. S.-K. Geng; Y. Zheng; S.-Q. Li; H. Su; X. Zhao, *et al. Nat. Energy*, **2021**, *6*, 904-912.
11. X. Zheng; J. Yang; P. Li; Z. Jiang; P. Zhu, *et al. Angew Chem Int Ed Engl*, **2023**, *62*, e202217449.
12. L. Wang; Y. Zhu; Y. Wen; S. Li; C. Cui, *et al. Angew Chem Int Ed Engl*, **2021**, *60*, 10577-10582.

13. W. Chen; C. Xie; Y. Wang; Y. Zou; C.-L. Dong*, et al. Chem*, **2020**, *6*, 2974-2993.

14. W. Chen; L. Xu; X. Zhu; Y. C. Huang; W. Zhou*, et al. Angew Chem Int Ed Engl*, **2021**, *60*, 7297-7307.

15. R. Lin; L. Kang; T. Zhao; J. Feng; V. Celorrio*, et al. Energy Environ. Sci.*, **2022**, *15*, 2386-2396.

16. Y. Wang; X. Zheng; D. Wang. *Nano Res.*, **2021**, *15*, 1730-1752.

17. Y. Gao; B. Liu; D. Wang. *Adv Mater*, **2023**, *35*, e2209654.

18. T. Sun; W. Zang; J. Sun; C. Li; J. Fan*, et al. Adv. Funct. Mater.*, **2023**, *33*, 2301526.

19. Y. Liu; C. Li; C. Tan; Z. Pei; T. Yang*, et al. Nat Commun*, **2023**, *14*, 2475.

20. X. Mu; X. Gu; S. Dai; J. Chen; Y. Cui*, et al. Energy Environ. Sci.*, **2022**, *15*, 4048-4057.

21. Q. Qian; X. He; Z. Li; Y. Chen; Y. Feng*, et al. Adv Mater*, **2023**, *35*, e2300935.

22. S. Sun; X. Zhou; B. Cong; W. Hong; G. Chen. *ACS Catal.*, **2020**, *10*, 9086-9097.

23. Y. Qi; Y. Zhang; L. Yang; Y. Zhao; Y. Zhu*, et al. Nat Commun*, **2022**, *13*, 4602.

Chapter 5. Bifunctional Ni phosphide catalysts for urea-assisted water electrolysis

5.1 Acknowledgement

I acknowledged Jianrui Feng for the DFT calculations and analysis Besides, I also acknowledged Jiexin Zhu, Liqun Kang, Longxiang Liu, Fei Guo, Jing Li, Kaiqi Li, Jie Chen, Wei Zong, Mingqiang Liu, Ruwei Chen, Liqiang Mai, Ivan P. Parkin, Guanjie He for their useful suggestion. The work described in this chapter was in submission and I was the first author.

5.2 Introduction

The electrochemical oxidation of small molecules (methanol, ethanol, hydrazine, and urea, etc.), with significantly lower thermodynamic potential, exhibits promising routes to replace the OER in various energy conversion applications.[1-3] Among those small molecule reactants, urea (non-toxicity and non-flammability), can be easily accessed from domestic wastewater (*e.g.* human urine). Nickel-based catalysts have been extensively reported due to the highly active dynamic Ni^{3+} active sites for UOR.[4, 5]

As compared to widely-used nickel oxide/hydroxide catalysts, nickel phosphides, sulfides, and nitrides exhibit good metallic electrical conductivity to facilitate electron transfer.[6-8] Notably, the stronger nucleophilicity of the *in situ* formed phosphate species (HPO_4 pKa = 12.7, HSO_4 pKa = 1.99, HNO_3 pKa = -1.3) during the surface reconstruction makes it possible to facilitate the adsorption and dehydrogenation of urea molecules.[9] Nonetheless, the surface reconstruction of nickel phosphides to *in situ* generate more NiOOH species has been hindered by the electro-repulsion between phosphate and hydroxide anion, which has been recently ascertained by Qiao's group.[10] Furthermore, as revealed by previous studies,[11] due to the insufficient Ni^{3+} active sites, the competition issue between UOR and OER is another enormous challenge to overcome (Figure 5.1 a).[12-14]

Metal mediation engineering strategies have been considered an effective route to modulate the proton-coupled-electron-transfer (PCET) process during the reconstruction process.[15, 16] Despite the enormous efforts to develop the non-noble metal mediation method, Pt still possesses a higher activity and durability in numerous energy conversion systems. Pt with partially filled 5d orbitals creates the possibility of interacting with various molecules, enabling fast electron transfer around the reaction microenvironments. Additionally, avoiding separating the fabrication process and assembling single-functionality catalysts, bifunctional electrocatalysts can enable reduced overall costs by simplifying the fabrication of anode and cathode to obviate leveraging varying precursors and procedures. Due to the same composite, The cross-contamination can also be mitigated during the surface reconstruction over the long-term operation.

Motivated by the tuning ability of adsorption/desorption for reactants and intermediates from Pt sites, in this chapter, a Pt-mediated strategy was proposed to facilitate the OH^- adsorption and optimize the electron distribution around Pt-Ni sites, thus generating abundant dynamic Ni^{3+} active sites during surface reconstruction of nickel phosphides. Combined with *in situ* spectroscopic investigation and DFT calculations, it is disclosed that the notable enriched Ni^{3+} active species would accelerate urea conversion (Figure 5.1 b). Additionally, as-prepared catalysts also exhibited promising HER performance to realize the urea-assisted water electrolysis for hydrogen production, This facile and feasible mediation strategy opens a unique avenue to fix issues during UOR and is anticipated to be extended to other energy conversion scenarios.

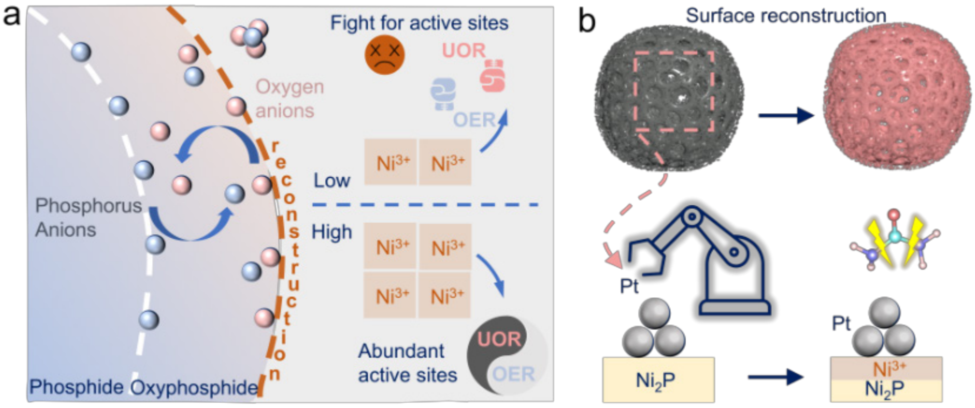

Figure 5.1. Schematic illustration of current issues and our solutions.

5.3 Experimental Section

5.3.1 Synthesis of Pt-Ni_2P catalyst

The $Ni(OH)_2$ catalyst was first fabricated with a similar method as reported in previous studies to synthesize Ni_2P catalysts.[17, 18] Briefly, 1 mmol $Ni(NO_3)_2{\cdot}6H_2O$ and 240 mg urea were first dissolved in 30 mL distilled water. The cleaned nickel foam (4 cm x 2 cm, thickness of 1 mm) was placed into the as-prepared solution and proceeded with hydrothermal reaction at 120 °C for 12 h. The as-synthesized $Ni(OH)_2$ catalyst was placed in the tube furnace with 1 g NaH_2PO_2 on the upstream side under the N_2 atmosphere for 10 min to exclude the air. A ramping rate of 10 °C min^{-1} was used to reach 300 °C and maintained for 1 h. The Pt-Ni_2P catalyst was subsequently prepared by a facile solution reduction method. Specifically, the Ni_2P catalysts were placed in the beaker and different feed amounts of Pt precursors (H_2PtCl_6 (8wt%)), including 20, 50, and 150 μL, were used combined with a reduction reagent of $NaBH_4$ (100 mg/10 mL) solutions to incorporate Pt sites on the Ni_2P catalysts.

5.3.2 Characterizations

The morphology was revealed by the TEM (JEOL, JEM-2100) and the SEM (JEOL LSM 7600). XRD patterns were collected by STOE SEIFERT diffractometer (Cu source radiation). XPS (Thermo scientific K-alpha photoelectron spectrometer) spectra were recorded with the calibration of

284.8 eV for C 1s. MP-AES (Agilent 4210) was used to analyze the Pt loading mass.

The Bruker Senterra Raman spectrometer was used to collect spectra with wavelengths of 532 nm. the Ag/AgCl electrode was used as the reference electrode; the self-standing catalyst on nickel foam was selected as the working electrode; the Pt wire was utilized as the counter electrode.

5.3.3 Electrochemical measurement

The Gamry Interface 1000 potentiostat was used to conduct electrochemical measurements at room temperature. 1 M KOH solution with and without 0.33 M urea was used as the electrolyte. The Ag/Ag Cl (sat. KCl) was selected as the reference electrode and the graphite rod was adopted as the counter electrode. LSV tests were performed at a scan rate of 5 mV s^{-1} with IR compensation. The Tafel plot was gained by replotting the polarization curve (Y-axis: potential, X-axis: log|current density|). The Tafel slope was thus obtained from a linear fitting of the Tafel plot. All the potentials were transformed versus RHE based on the equation: $E_{RHE} = E_{Ag/AgCl} + 0.197 + 0.059$ pH. The *in situ* EIS measurements were performed in 1M KOH at the frequency range from 10^{-2} to 10^{5} Hz at different applied potentials.

A polished Zn plate (negative electrode) and catalysts ink (1 mg Pt-Ni_2P and 1 mg Pt/C, 20 μL Nafion, and 300 μL ethanol) drop-casted on the carbon paper (positive electrode) were used for Zn-air and Zn-urea-air batteries test. The fresh electrolyte was added every 10 hours to obviate the effect of rapid urea consumption.

MEA tests were conducted by using a setup with two stainless steel plates (circular serpentine channels, 1 cm^{-2}). The Pt-Ni_2P catalysts were employed as the anode and cathode. The anion exchange membrane was used with the type of Sustainion X37-50 Grade 60.

5.3.4 DFT calculation

DFT calculations were carried out in the Vienna *ab initio* simulation package (VASP) with the projector augmented wave (PAW) pseudopotential.

Generalized gradient approximation (GGA) of Perdew-Burke-Ernzerhof (PBE) functional was used to describe the exchange and correlation interactions. The cut-off energy for plane waves was set to 400 eV. The thresholds of convergence were set to 1 × 10^{-5} eV for self-consistency. The Brillouin zone was sampled with a 1 × 1 × 1 *k*-point grid for all calculations and the van der Waals interaction was considered by the empirical correction of Grimme's scheme (DFT-D3). The model was built by construing a tetrahedron Pt_4 cluster on the Ni_2P (001) and NiOOH (001) surfaces, respectively.

The adsorption energies (E_{ads}) of the urea on the surface of the substrates are calculated by the following equation:

$$E_{ads}=E_{urea/sub}-E_{urea}-E_{sub}$$

where the $E_{urea/sub}$, $E_{urea,}$ and E_{sub} are the total energy of urea and substrate, the energy of isolated urea, and the energy of the substrate system.

5.4 Results and discussion

5.4.1 Pt-Ni_2P catalysts

The Pt was first incorporated on nickel phosphide catalysts based on nickel foams *via* solution reduction synthesis. A single phase of Ni_2P (PDF No. 89-4864) was revealed by the XRD patterns (Figure 5.2).

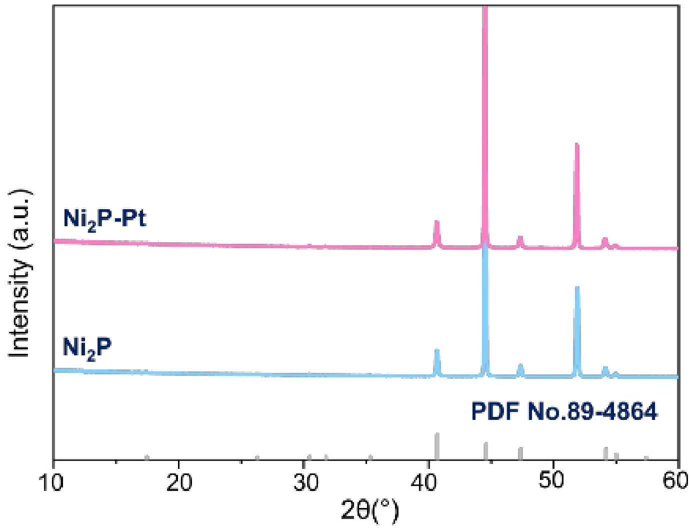

Figure 5.2. XRD patterns of $Ni_2P$and Pt-Ni_2P catalysts.

The HRTEM image presents Pt nanoparticles with (111) lattice, indicating the successful construction of Pt sites on Ni_2P catalysts (Figure 5.3). The corresponding EDS mapping images further indicate the uniform distribution of Pt on the Ni_2P catalyst (Figure 5.4).

The different feed amounts of Pt precursors were also investigated by MP-AES, with the loading mass of 20, 80, and 131 μg cm^{-2} when utilizing 20, 50, and 150 μL Pt precursors (Figure 5.5 a). According to the results of XRD patterns and SEM images, the Pt was incorporated into Ni_2P catalysts with a notable change in the roughness of morphologies (Figure 5.5 b and Figure 5.6), offering the possibility of optimizing the interaction between reactants/intermediates with the electrode surface.

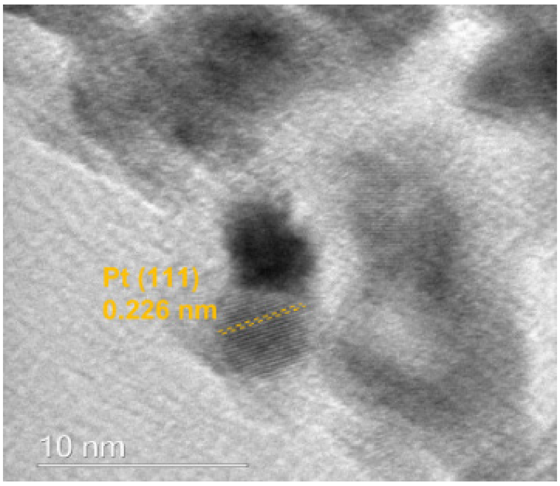

Figure 5.3. HRTEM image of Pt-Ni_2P catalysts.

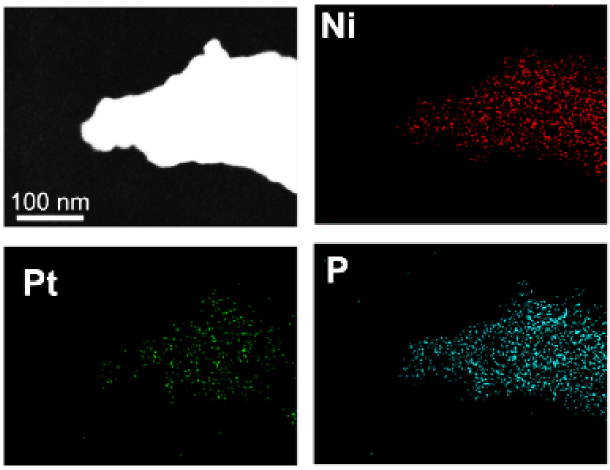

Figure 5.4. EDS mapping of Pt-Ni_2P catalyst, including elements of Ni, P, and Pt.

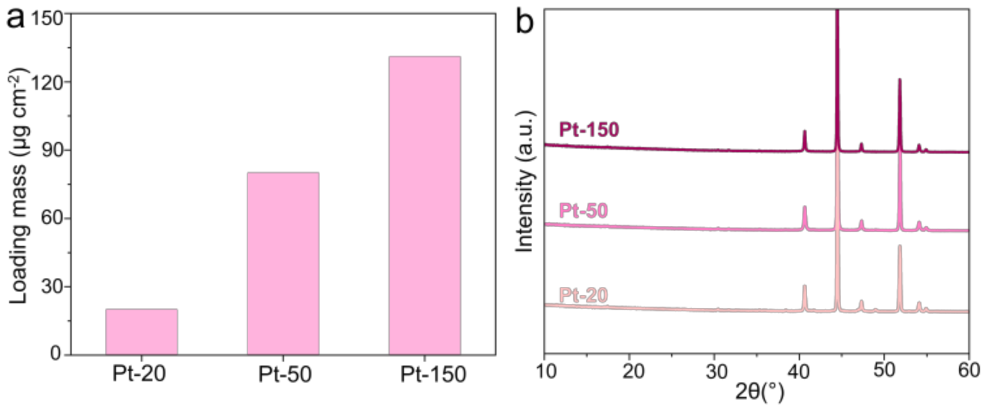

Figure 5.5. Characterization of catalysts with diverse feed amounts of Pt, including 20, 50, and 150 µL Pt precursor, labeled as Pt-20, Pt-50, and Pt-150, respectively. (a) the loading mass of Pt species quantified by MP-AES. (b) XRD patterns.

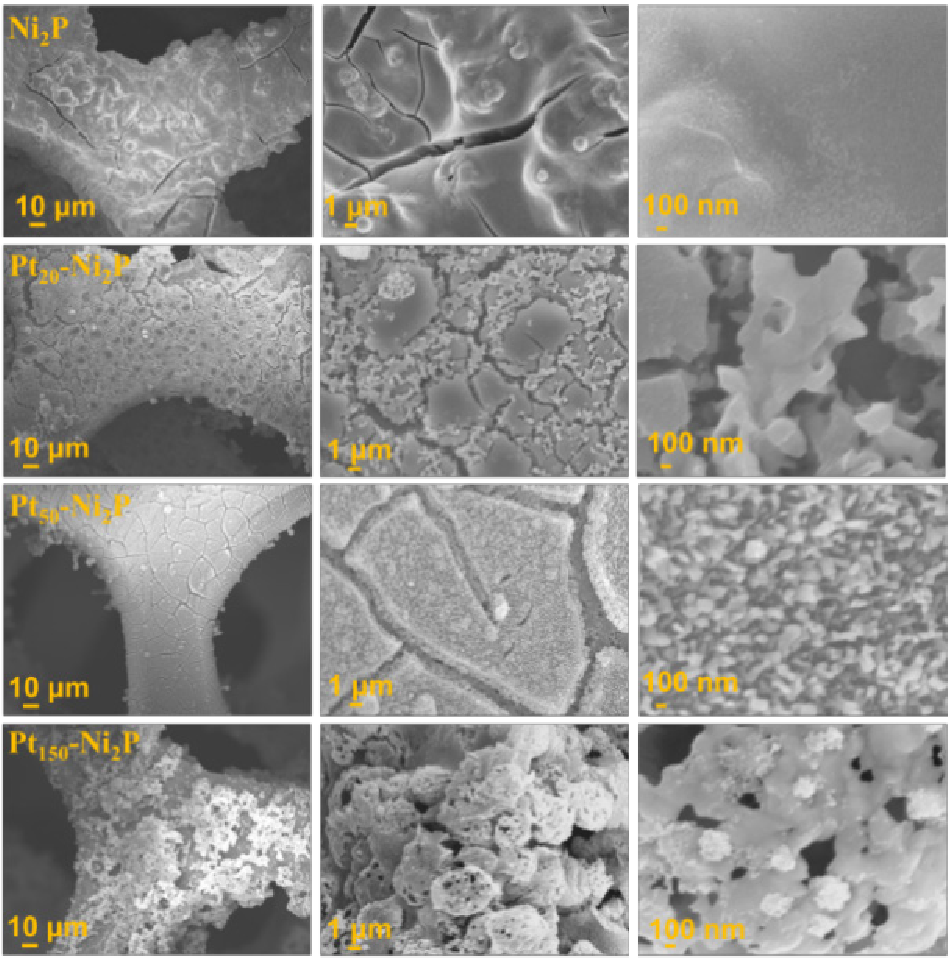

Figure 5.6. Morphologies of Ni_2P and Pt-Ni_2P with different feed amounts of Pt precursor, including 20, 50, and 150 µL Pt precursor, labeled as Pt-20, Pt-50, and Pt-150, respectively.

5.4.2 Electrocatalytic performance

The electrochemical UOR performance was subsequently evaluated in a three-electrode system. The Pt-Ni_2P catalysts required only 1.38 V *vs.* RHE to reach the current density of 100 mA cm^{-2} (Figure 5.7 a) and yield a remarkably smaller Tafel slope (28.3 mV dec^{-1}), implying accelerated UOR kinetics and outperform most recently reported electrocatalysts (Figure 5.7 b). The potential was negatively shifted by 203 mV as compared to the OER under the current density of 100 mA cm^{-2} (Figure 5.7 c). The feed amounts of the Pt precursor (50 μL) were confirmed as the optimized ratio with good commercial feasibility (Figure 5.7 d).

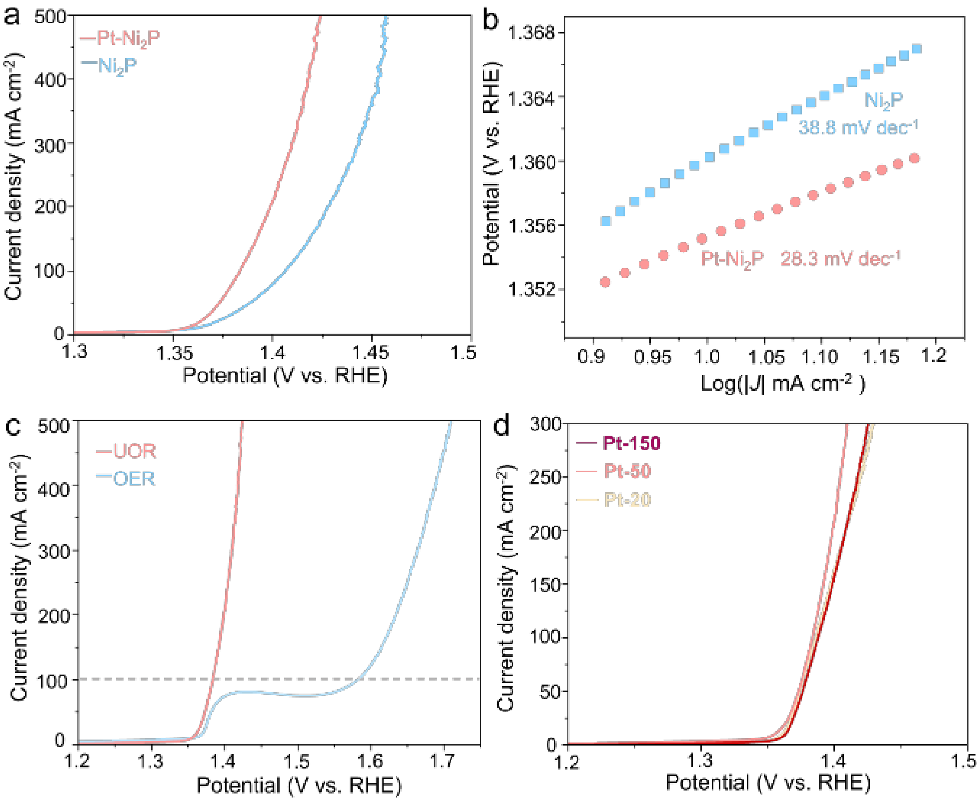

Figure 5.7. (a) Polarization curves of Ni_2P and Pt-Ni_2P catalysts. (b) Tafel slopes. (c) LSV curves of Pt-Ni_2P catalysts during UOR and OER. (d) LSV curves of Pt-Ni_2P with different feed amounts of Pt source.

The *in situ* EIS investigation was thereafter performed to unearth the potential-dependent interfacial charge transfer in different phases. To obviate the effect of urea dehydrogenation on the Ni^{3+} species formation, *in situ* EIS studies were conducted in 1 M KOH (Figure 5.8 a and b). The peak in the

Bode plot can be observed at high frequency, corresponding to the surface oxidation to form Ni^{3+} species (Figure 5.9). It is notable that the phase angle remarkably decreases when the potential reaches 1.37 V *vs.* RHE and disappears after 1.42 V *vs.* RHE, signifying the rapid formation of Ni^{3+} species on the surface.

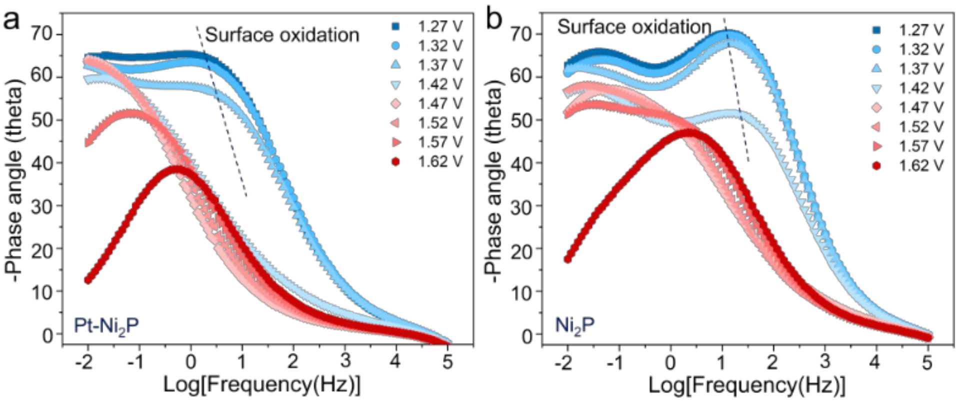

Figure 5.8. *In situ* EIS for OER at different potentials.

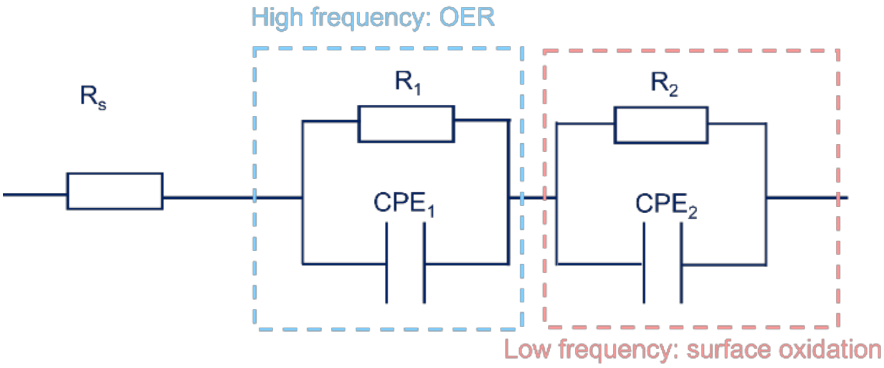

Figure 5.9. Schematic illustrations of the equivalent circuit to demonstrate the interfacial electron charge transfer behavior in varying phases during the OER process.

To probe the role of Pt sites in the generation of Ni^{3+} species, the Faradaic charge transfer for Ni^{2+} to Ni^{3+} was calculated (Figure 5.10 a and b). Introducing Pt sites remarkably boosted the Ni^{3+} active species formation with a higher Faradaic charge of 854 mC. Additionally, the reduction peak of CV curves during UOR features an enhanced and negative trend than Ni_2P catalysts. This reduction peak correlated to Ni^{3+} to Ni^{2+} elucidated a higher concentration of Ni^{3+} species when incorporating Pt sites (Figure 5.10 c). The C_{dl} of Pt-Ni_2P is 11.5 mF cm^{-2}, higher than Ni_2P (Figure 5.10 d-f), substantiating sufficient active sites *via* introducing Pt sites. The Pt/C catalyst was further utilized as the control sample to verify the activity of Pt during UOR (Figure 5.11).

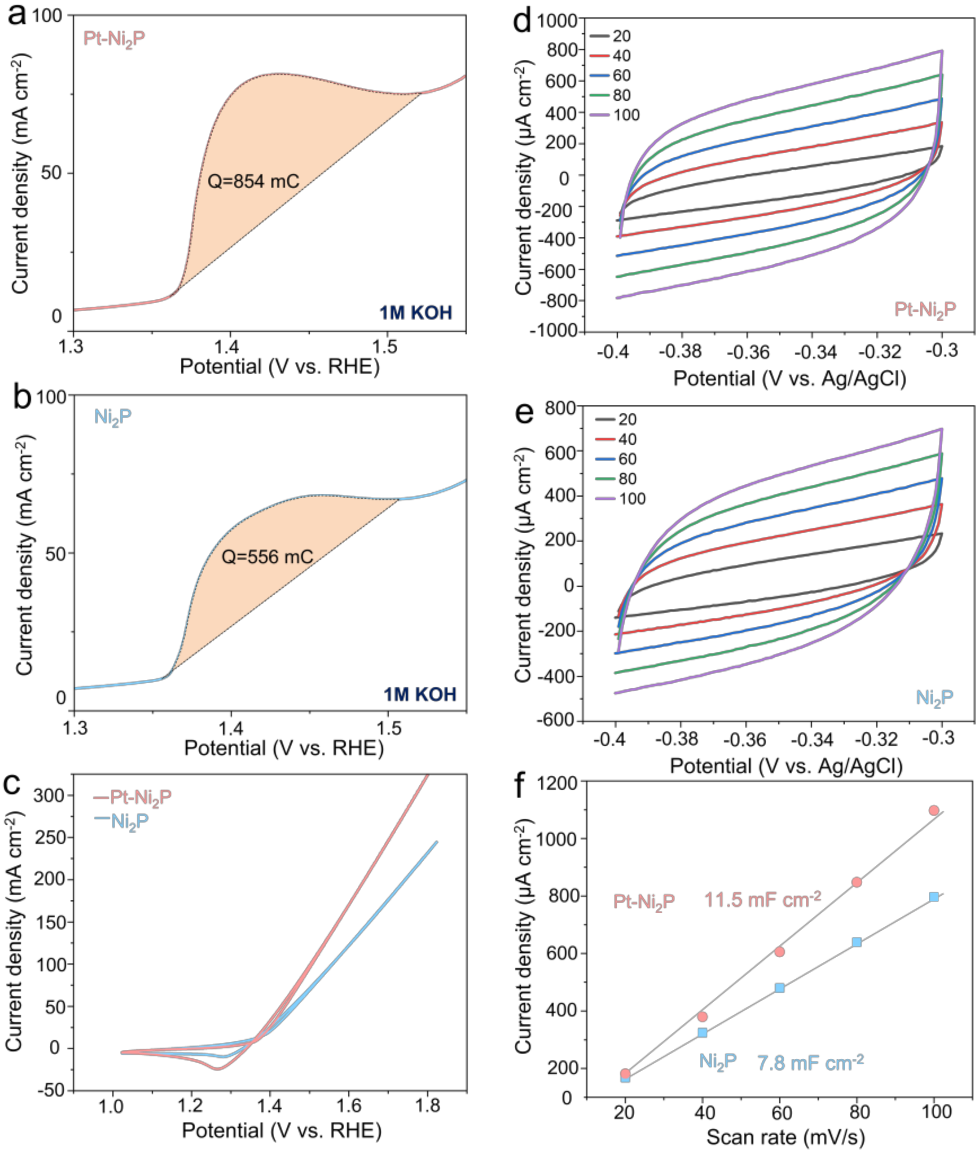

Figure 5.10. The evaluation of the dynamic Ni^{3+} active species formation. (a-b) integrated Ni^{2+} to Ni^{3+} oxidation peak of Pt-Ni_2P and Ni_2P, respectively. Q is the faradaic charge transfer to estimate the ability of Ni^{2+} to Ni^{3+} and the value can be calculated by the equation: Q= S/*v*, where *v* is the scan rate (5 mV/s) and S represents the integrated mathematical area (yellow shadow). (c) CV curve of Pt-Ni_2P and Ni_2P catalysts in the electrolyte of 1M KOH +0.33M urea. (d)-(e) CV scanning curves at various scan rates in the non-Faradaic potential region. (f) Capacity current density at -0.35 V vs. Ag/AgCl as functional of scan rate.

It was discovered that the onset potential of the Pt/C catalyst was around 1.6 V *vs.* RHE, corroborating an undesirable activity for urea conversion with only Pt sites. To further comprehend the electrochemical process of the UOR, the intermittent UOR test was carried out by separating the process of urea dehydrogenation and proton deintercalation from the catalyst (Figure 5.12).

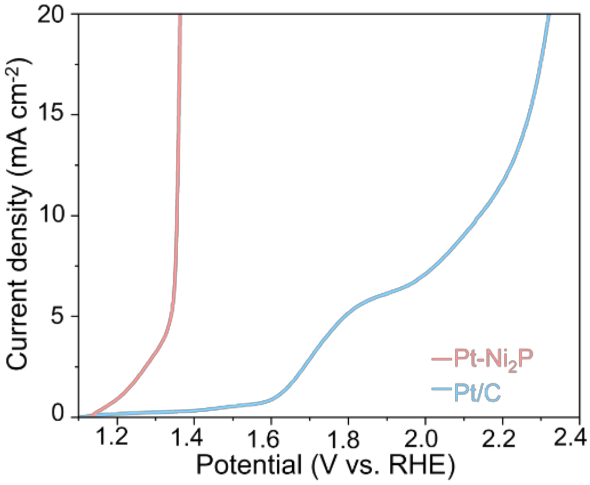

Figure 5.11. Polarization curves of Pt/C and Pt-Ni_2P catalysts.

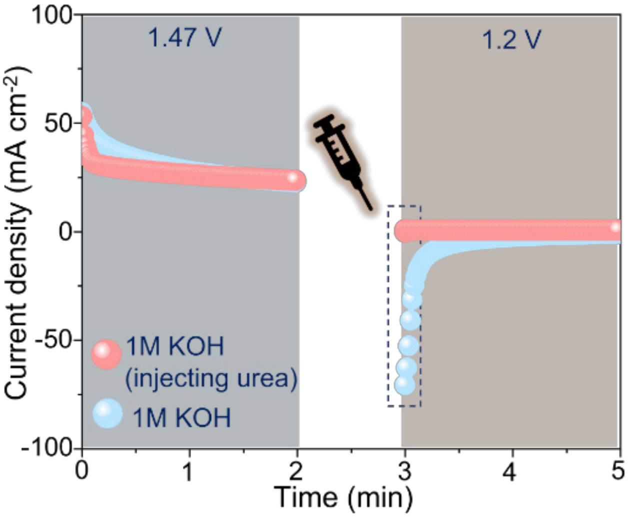

Figure 5.12. Intermittent UOR test.

An oxidation current related to forming NiOOH species was first observed in 1 M KOH at 1.47 V *vs.* RHE and lasted for 2 mins. The 0.33 M urea was then injected at OCP and lasted for 1 min. Intriguingly, no reduction current was observed at a cathodic applied potential of 1.2 V *vs.* RHE. Contrastingly, a significant reduction occurred without adding urea. According to the above results, it can be speculated that the electro-generation of oxyhydroxide species would proceed during surface reconstruction and accept protons from urea to be reduced to hydroxide spontaneously, and thus without reduction current being detected.

The OER competing effect is another enormous challenge to obviate during UOR. The rotating ring-disk electrode (RRDE) system with the elimination of the mass transfer could be an effective method to measure the O_2 generation for evaluation of the selectivity (Figure 5.13).

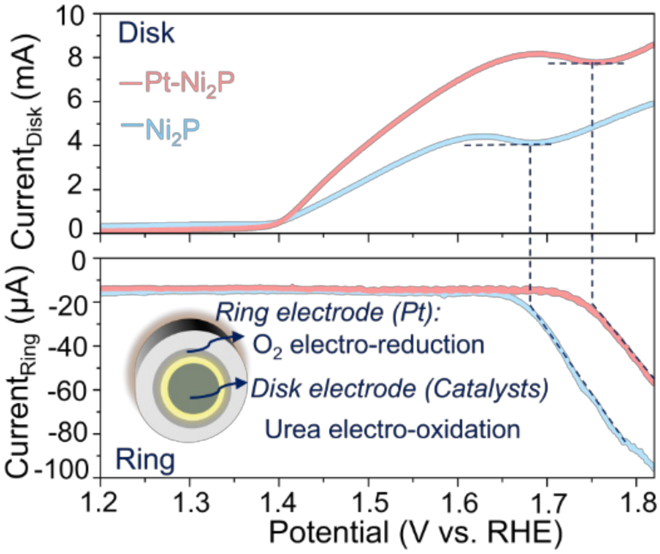

Figure 5.13. RRDE system (1600 rpm) for oxygen reduction detection.

It was perceived that negligible oxygen reduction current could be observed before 1.65 V *vs.* RHE for both Pt-Ni_2P and Ni_2P catalysts. Impressively, the intensified OER competition on Ni_2P would be detected at 1.67 V *vs.* RHE. There is a ~ 100 mV positive shift for Pt-Ni_2P catalysts to be affected by the OER competition, demonstrating a relatively promising selectivity as compared to pure Ni_2P catalysts.

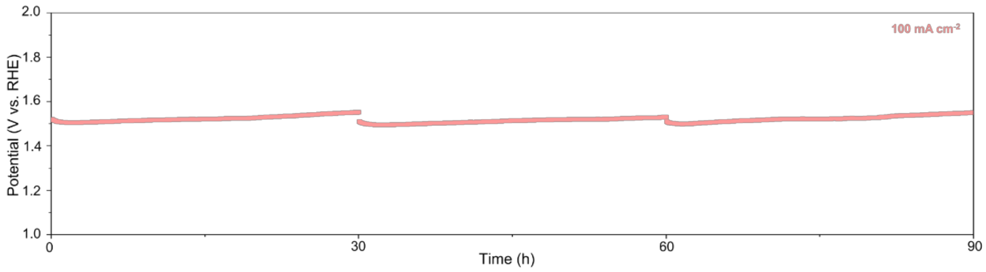

Figure 5.14. Stability test at 100 mA cm^{-2} over 90 hours (adding fresh electrolyte every 30 hours).

Moreover, over 90 hours of chronopotentiometry test was operated at a constant current density of 100 mA cm^{-2}, verifying good stability for practical applications under industrial currents (Figure 5.14).

To decipher the effect of Pt mediation on Ni_2P catalysts and establish the structure-performance relationship, mechanism studies were accordingly performed. The XRD patterns after the stability test over 90 h exhibit negligible variation with only one single phase of Ni_2P (Figure 5.15).

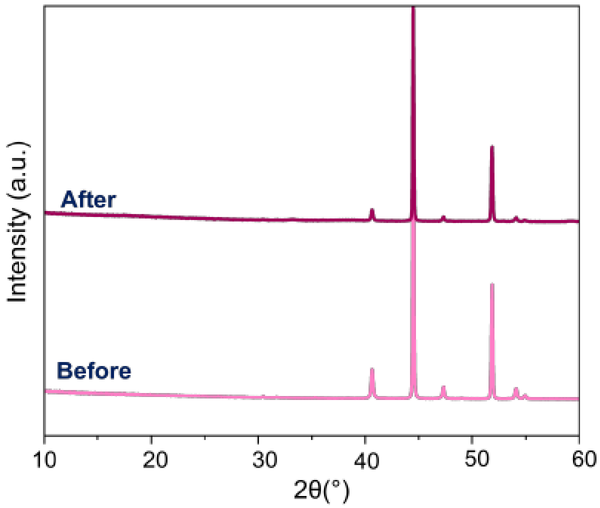

Figure 5.15. XRD pattern of post-UOR Pt-Ni_2P catalysts.

Significant P leaching was revealed by XPS spectra before and after UOR, signifying surface reconstruction proceeding during UOR (Figure 5.16 a).

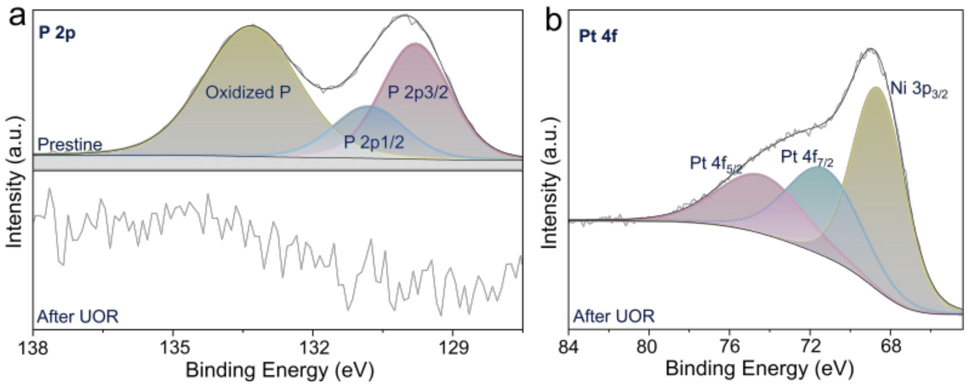

Figure 5.16. XPS spectra of P 2p and Pt 4f.

The peaks from XPS spectra of Pt 4f located at 71.3 and 74.5 eV correspond to metallic Pt, elucidating the stable existence of Pt sites during the long-term stability test (Figure 5.16 b). The morphology changes were then unearthed by SEM and HRTEM (Figure 5.17).

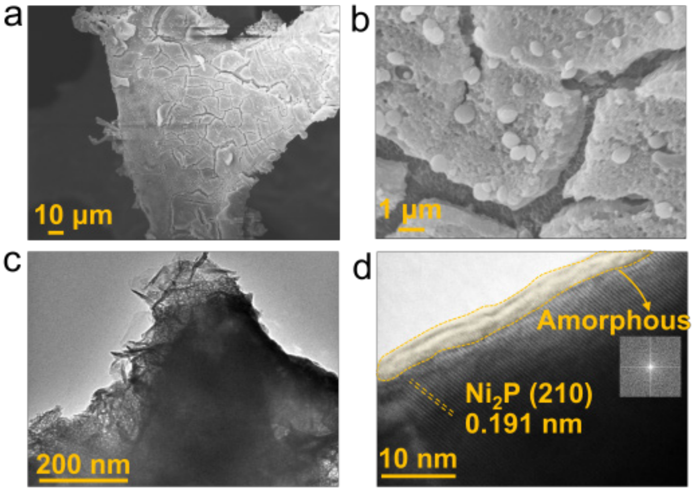

Figure 5.17. The morphology of post-UOR Pt-Ni_2P catalysts. (a)-(b) SEM images. (c)-(d) HRTEM images

Nanosheet-like structures were observed on the edge of the catalysts, which might be the formation of Ni (oxy)hydroxide species as revealed by previous studies. Specifically, the amorphous layer was discovered, close to the Ni_2P phase, affirming the electro-generation of amorphous Ni (oxy)hydroxides on the edge of Ni_2P catalysts during surface reconstruction.

5.4.3 Investigation of surface reconstruction

The surface reconstruction was further dissected by *in situ* spectroscopic investigation. As revealed by Raman spectra, two peaks situated at 474 and 553 cm^{-1}, corresponding to Ni^{3+}–O in NiOOH species (Figure 5.18), emerged at 1.42 V *vs.* RHE, which is notably lower than that of pure Ni_2P catalysts (1.57 V *vs.* RHE) (Figure 5.19). When the applied potential came back to OCP, the peaks of Ni^{3+}–O could not be discernible. As for proceeding during OER, the paired peaks of Ni^{3+}–O occurred after 1.37 V *vs.* RHE and could be maintained at OCP (Figure 5.20 a). As revealed by Raman spectra, the Ni oxyhydroxides species accumulated during OER at 1.47 V *vs.* RHE over 600 s would be rapidly reduced when adding urea into the electrolyte at OCP (Figure 5.20 b), which is in line with the results of intermittent UOR test (Fig. 5.12).

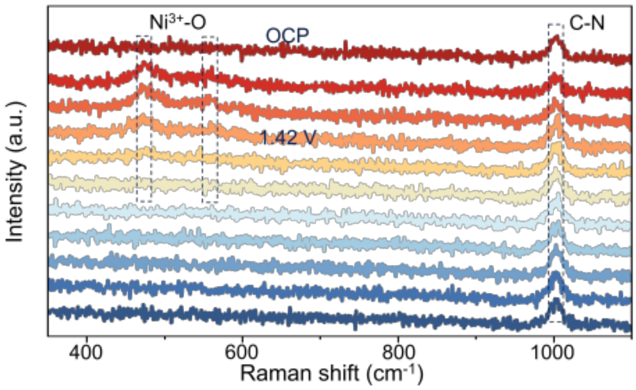

Figure 5.18. Raman spectra of Pt-Ni_2P at varying applied potentials during UOR.

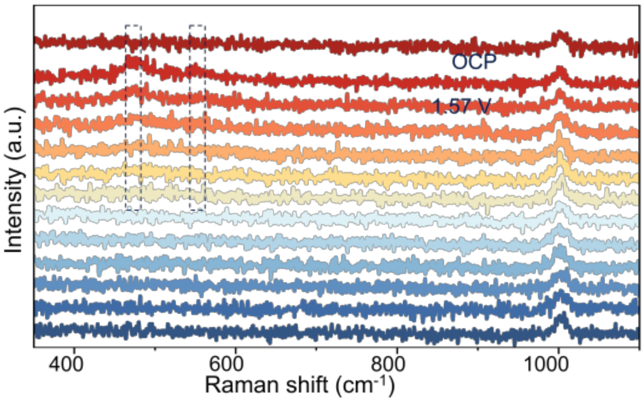

Figure 5.19. Raman spectra of Ni_2P at varying applied potentials during UOR.

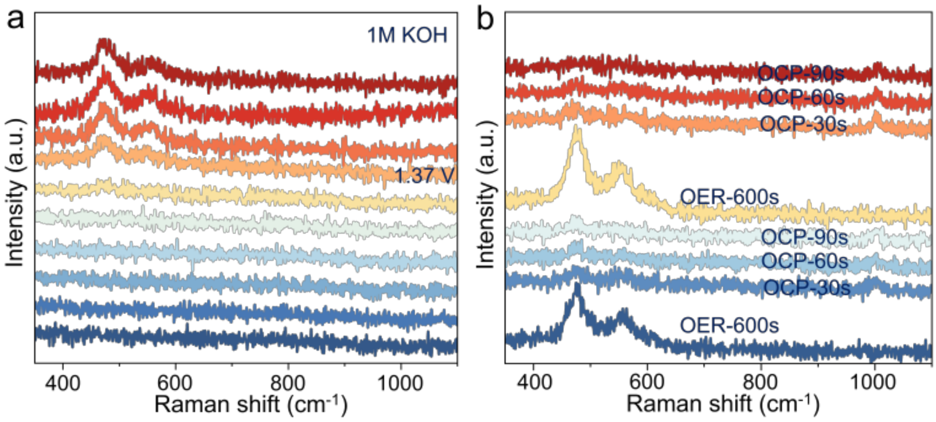

Figure 5.20. The Raman spectra. (a) OER. (b) intermittent UOR test.

DFT calculation was then carried out to certify the consistency with the experimental observations. It showed that more negative adsorption energy of OH^- species on Pt-Ni_2P surface than that of pure Ni_2P (Figure 5.21), including adsorption configuration of Ni–OH (0.22 eV), P–OH (0.01 eV), and Pt–OH (-0.13 eV).

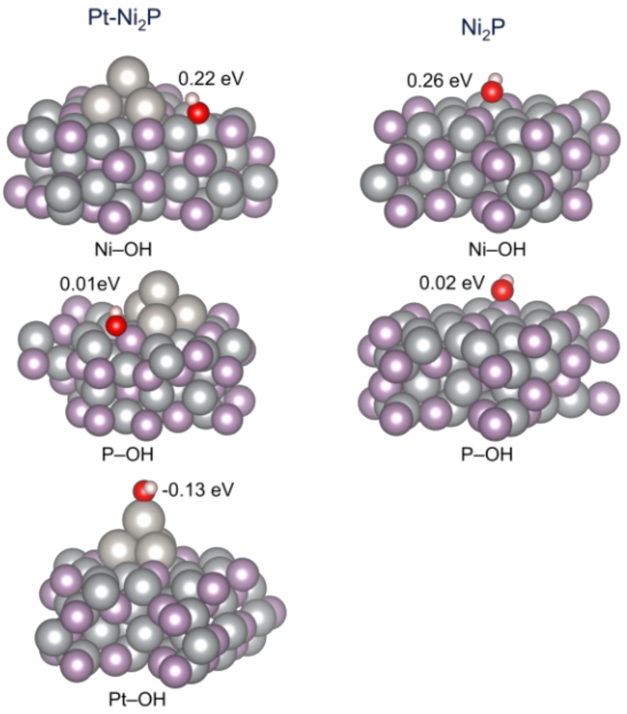

Figure 5.21. The adsorption energy of OH^- on Pt-Ni_2P and Ni_2P optimized model.

Based on the above experimental studies and theoretical calculations, it could be deduced that the surface reconstruction process of Ni_2P is fast to form stable high valence Ni active sites, the reconstituted Ni oxyhydroxide surface layer is the real active species during UOR.

5.4.4 Applications of Pt-Ni_2P catalysts

To achieve this promising vision, the HER performance of as-prepared Pt-Ni_2P catalysts was evaluated, which exhibits superior activities than commercial Pt/C catalysts and high stability at 100 mA cm^{-2} over 100 h (Figure 5.22). As for the two-electrode system, the Pt-Ni_2P catalyst also shows higher activities compared to pure Ni_2P and has the potential to replace OER in practical scenarios (Figure 5.23 a and b). During 12 hours of chronopotentiometry tests at 100 mA cm^{-2}, the cell voltage was stable without conspicuous increases (Figure 5.24).

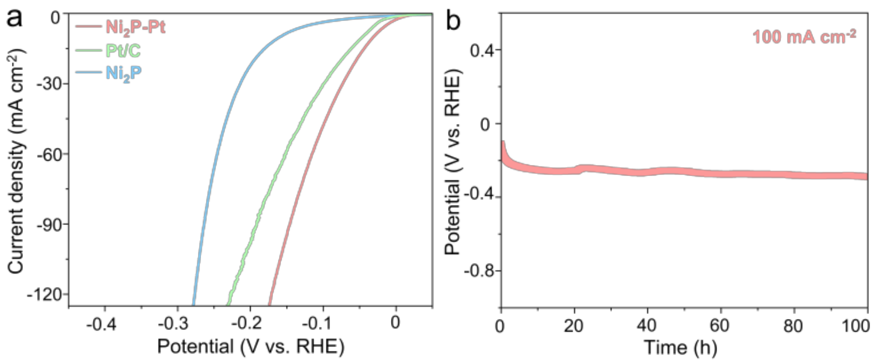

Figure 5.22. HER performance evaluation. (a) LSV curves. (b) Stability test at 100 mA cm^{-2} over 100 hours.

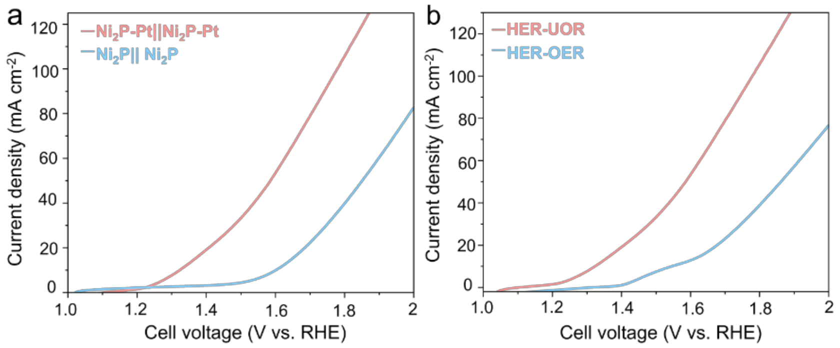

Figure 5.23. (a) Polarization curves of two-electrode for Ni_2P and Pt-Ni_2P catalysts. (b) Polarization curves of two-electrode for HER-UOR and HER-OER.

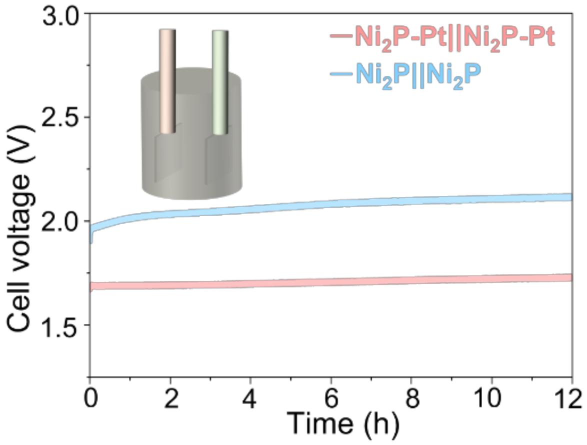

Figure 5.24. Stability test during 12 hours.

Another proof of concept for substituting OER with UOR in energy conversion systems is the Zn-air battery. The cycling measurements over 66 hours were carried out with and without adding urea, labeled as Zn-air battery and Zn-urea-air battery. The charging process involving OER would proceed with UOR instead. The charging curves of the Zn-air battery and Zn-urea-air battery demonstrated a remarkable reduction of the charging voltage after adding urea to the electrolyte (Figure 5.25). The cycling stability test during 66 h further exhibits about ~ 162 mV decrease in the charging voltage than that of the Zn-air battery (Figure 5.26).

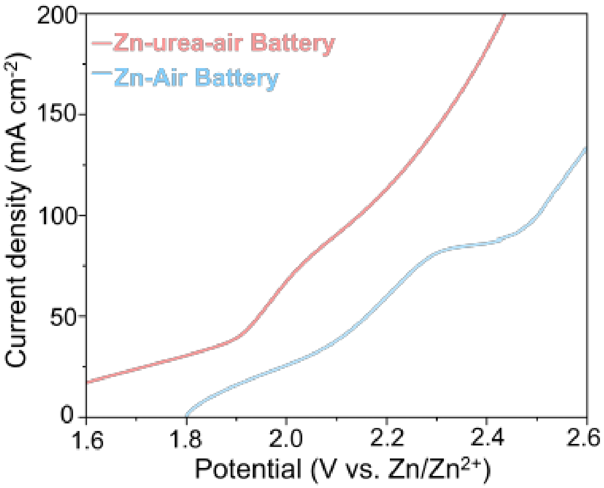

Figure 5.25. Charging curves of the Zn-battery and Zn-urea-air battery.

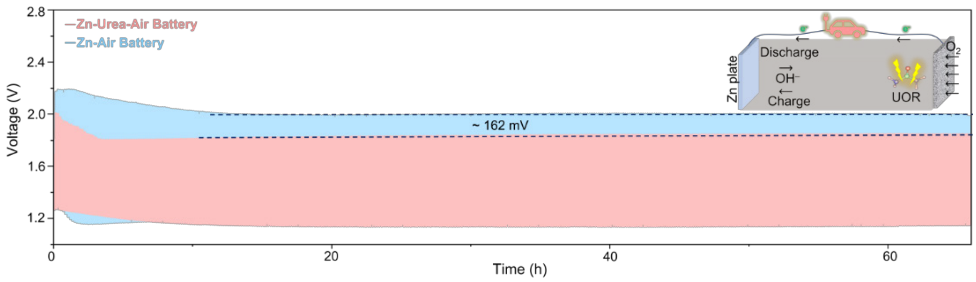

Figure 5.26. Electrochemical measurement for Zn-air battery and Zn-urea-air battery (current density of 5 mA cm^{-2}).

To realize urea-assisted hydrogen production for large-scale applications by direct usage of urea-bearing wastewater, the MEA test was conducted (Figure 5.27). As-prepared Pt-Ni_2P catalysts possessed superior activity (Figure 5.28) and stability at industrial-level current densities of 200 mA cm^{-2} during chronopotentiometry measurement over 135 h. No conspicuous voltage depletion could be observed, implying the possibility for extensive practical applications.

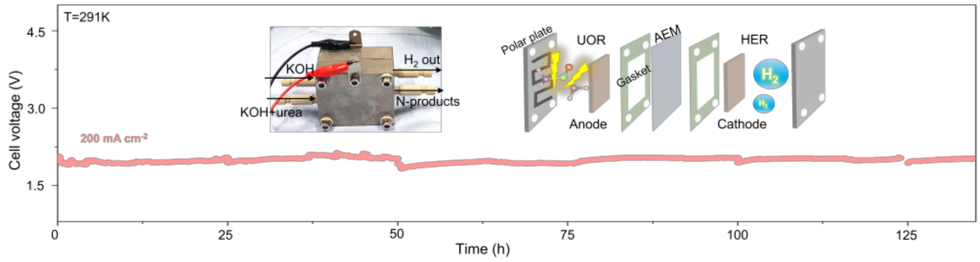

Figure 5.27. MEA test to validate Urea-assisted water electrolysis under large current densities.

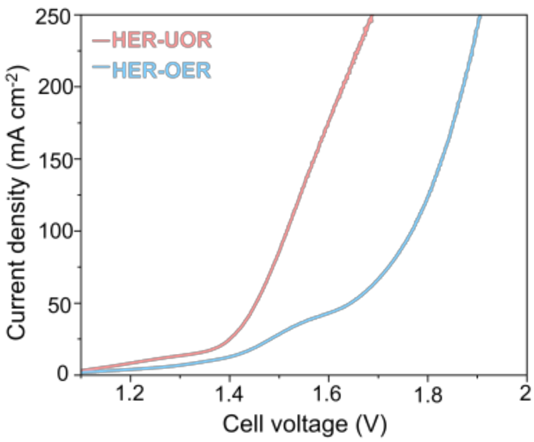

Figure 5.28. Polarization curves during MEA tests.

5.5 Conclusion

The high activity, selectivity, and stability of Pt-mediated Ni_2P catalysts were achieved by using a Pt-mediated strategy to facilitate the adsorption of OH^- and optimize the electron distribution around Pt-Ni sites. The abundant dynamic Ni^{3+} active sites could be discerned during the surface reconstruction of nickel phosphides. Combined with *in situ* spectroscopic investigation and DFT calculations, it is disclosed that the notable enriched Ni^{3+} active species would accelerate urea conversion. The Pt-Ni_2P catalysts exhibit superior UOR activity amidst the concurrent process of UOR and OER. Additionally, as-prepared catalysts also exhibited promising HER performance. 60 h Zn-urea-air battery cycle test and over 135 h MEA test for urea-assisted water electrolysis demonstrate the practicality of Pt-Ni_2P catalysts and high potential to replace OER with UOR. It is expected that this work supplies valuable insights into the regulation of electrocatalysts for green energy production.

5.6 References

1. X. Zou; M. Tang; Q. Lu; Y. Wang; Z. Shao, *et al. Energy Environ. Sci.*, **2024**, *17*, 386-424.
2. J.-T. Ren; L. Chen; H.-Y. Wang; W.-W. Tian; Z.-Y. Yuan. *Energy Environ. Sci.*, **2024**, *17*, 49-113.
3. J. Li; H. Li; K. Fan; J. Y. Lee; W. Xie, *et al. Chem Catal.*, **2023**, *3*, 100638.
4. X. Zhang; S. Feizpoor; M. Humayun; C. Wang. *Chem Catal.*, **2024**, *4*, 100840.
5. Q. Zheng; Y. Yan; J. Zhong; S. Yan; Z. Zou. *Energy Environ. Sci.*, **2024**, *17*, 748-759.
6. X. Xu; Y. Lu; J. Shi; X. Hao; Z. Ma, *et al. Nat Commun*, **2023**, *14*, 7708.
7. Y.-N. Zhou; F.-T. Li; B. Dong; Y.-M. Chai. *Energy Environ. Sci.*, **2024**, *17*, 1468-1481.
8. Z. Yang; S. Wang; C. Wei; L. Chen; Z. Xue, *et al. Energy Environ. Sci.*, **2024**, *17*, 1603-1611.

9. Z. Ji; W. Yuan; S. Zhao; T. Wang; S. Umer*, et al. Chem Catal.*, **2023**, *3*, 100501.

10. X. Gao; X. Bai; P. Wang; Y. Jiao; K. Davey*, et al. Nat Commun*, **2023**, *14*, 5842.

11. R. Lin; L. Kang; T. Zhao; J. Feng; V. Celorrio*, et al. Energy Environ. Sci.*, **2022**, *15*, 2386-2396.

12. M. Zhong; M. Xu; S. Ren; W. Li; C. Wang*, et al. Energy Environ. Sci.*, **2024**, *17*, 1984-1996.

13. S. Xu; X. Ruan; M. Ganesan; J. Wu; S. K. Ravi*, et al. Adv. Funct. Mater.*, **2024**, *34*, 2313309.

14. W. Chen; L. Xu; X. Zhu; Y. C. Huang; W. Zhou*, et al. Angew Chem Int Ed Engl*, **2021**, *60*, 7297-7307.

15. B. Zhou; Y. Li; Y. Zou; W. Chen; W. Zhou*, et al. Angew Chem Int Ed Engl*, **2021**, *60*, 22908-22914.

16. W. Chen; C. Xie; Y. Wang; Y. Zou; C.-L. Dong*, et al. Chem*, **2020**, *6*, 2974-2993.

17. J. Zhang; J. Zhu; L. Kang; Q. Zhang; L. Liu*, et al. Energy Environ. Sci.*, **2023**, *16*, 6015-6025.

18. J. Zhang; X. Song; L. Kang; J. Zhu; L. Liu*, et al. Chem Catal.*, **2022**, *2*, 3254-3270.

Chapter 6. Conclusions and perspectives

The PhD project is focused on the modification of Ni-based catalysts for UOR to overcome the challenges of undesirable UOR performance in terms of activity, stability, and selectivity, gaining reliable reaction mechanisms, and the validation of practical scenarios to replace OER with UOR based on device tests for energy conversion applications.

The strategies used in this thesis to elevate the UOR performance mainly involved incorporating the second elements with partially filled d electrons into Ni-based catalysts to modulate the electronic structure of Ni active sites. The Cr, Ru, and Pt with variously filled d electrons were introduced into $Ni(OH)_2$ and Ni_2P, respectively. The electronic structures of as-prepared catalysts were well-tuned. The doping strategies also facilitate wetting property control by incorporating micro-nano hierarchical structures, which can boost the mass and electron transfer. The electrochemical step for Ni^{3+} formation could be accelerated by favorable adsorption of OH^- after incorporating extra metal sites to optimize the interfacial electric field to stabilize the crucial intermediates.

Except for the electrochemical performance improvements, the strategy for gaining reliable reaction mechanisms during the UOR process is to employ *in situ* spectroscopic characterization. The Raman spectra were verified as an effective tool to reveal the dynamic evolution of Ni^{3+} active sites and dopant structure changes. Combined with the DFT calculations, the Cr dopant leaching issues and rate-determining step in both low and high urea concentrations were revealed.

To validate the applicability of as-prepared catalysts, the Zn-urea-air battery and zero-gap MEA test were designed and carried out. During more than 100 hours of operation test, a large current density of over 100 mA cm^{-2} was used to extend the fundamental research to meet the industrial requirements.

Based on the above strategies, the objectives for realizing urea-assisted water electrolysis were well achieved. Some generic conclusions from the whole thesis could be gained. (1) Regulation of wetting properties can significantly influence the reaction interface between electrolyte and electrode involving electrons, ions, and gas products. (2) Metal dopant dissolution issues during electro-oxidation reactions can notably affect the electrochemical performance. (3) Balancing Ni active sites plays a key role in elevating UOR performance.

Despite the achievements in the modification of Ni-based catalysts for UOR during my Ph.D. stage, there are still several challenges in this area that require to be overcome in the future with more desirable strategies.

First, the catalytic reaction pathway can vary for a specific Ni-based catalyst. Exploring the reaction pathways of UOR for different Ni-based catalysts is still needed. The in-depth and novel structure-performance relationship should be established based on the more advanced *in situ* characterization methods, such as Raman, XAS, FTIR, and DEMS, to reflect the reaction microenvironments in real time and effectively detect the short-lived intermediates.

Second, to achieve commercial applicability, high-performance UOR catalysts are expected to be synthesized by facile, environmentally friendly, and cost-effective fabrication methods with earth-abundant and inexpensive materials. Meanwhile, the as-prepared catalysts should retain their activity over long-term operations (>1000 hours) without notable performance depletion. This is the primary goal of developing new UOR catalysts for large-scale applications.

In addition, how to realize the lab-to-fab process remains a huge challenge. For example, the direct usage of urea-bearing wastewater like urine is rarely reported. The complicated compositions of urine would probably affect the sustainable efficiency of active sites. Furthermore, most of the studies only worked on the development of catalysts, overlooking the device test in practical scenarios. To achieve the goal of urea-assisted water electrolysis for hydrogen production, the optimized zero-gap membrane electrode assembly (MEA) test under large current density should be performed to validate the applicability of as-prepared catalysts.

Moreover, performing theoretical calculations based on density functional theory (DFT) and machine learning to realize high-throughput screening is expected to predict efficient catalysts and gain more reliable catalytic mechanisms based on experimental studies, such as reaction pathways, synergetic effects between various dopants, and active site analysis.

Furthermore, the studies of over-oxidation of urea with the main products of nitrite or nitrate have recently emerged from the research community. Instead of generating low-value N_2 gas, it is expected to synthesize high-value N-products during the UOR process with the suitable modification of the reaction pathway. Another challenge is to extend the UOR application from water electrolysis for green hydrogen production to the electro-reduction of CO_2 and NOx. Achieving high-value C or N-based chemicals with lower energy consumption is mainly hindered by anodic reactions with large overpotentials. Developing UOR catalysts with an overpotential close to zero is still required to be realized in the future.

Publication list

1. **Jichao Zhang**, Xuedan Song, Liqun Kang, Jiexin Zhu, Longxiang Liu, Qing Zhang, Dan J. L. Brett, Paul Shearing, Liqiang Mai, Guanjie He, and Ivan P. Parkin. Stabilizing Efficient Structures of Superwetting Electrocatalysts for Enhanced Urea Oxidation Reactions. ***Chem Catal***., 2022, 2, 3254–3270.

2. **Jichao Zhang,** Jiexin Zhu, Liqun Kang, Qing Zhang, Longxiang Liu, Fei Guo, Kaiqi Li, Jianrui Feng, et al. Balancing Dynamic Evolution of Active Sites for Urea Oxidation in Practical Scenarios. ***Energy Environ. Sci.*** 2023, 16, 6015-6025.

3. **Jichao Zhang,** Jianrui Feng, Guanjie He, et al. Regulating reconstruction-engineered active sites for accelerated electrocatalytic conversion of urea. ***Angew. Chem. Inter. Ed.*** 2024 (In submission)

4. Longxiang Liu, Liqun Kang, Jianrui Feng, David Hopkinson, Christopher Allen, Yeshu Tan, Hao Gu, Iuliia Mikulska, Veronica Celorrio, Diego Gianolio, Tianlei Wang, Liquan Zhang, Kaiqi Li, **Jichao Zhang**, et al. Atomically Dispersed Asymmetric Cobalt Electrocatalyst for Efficient Hydrogen Peroxide Production in Neutral Media. ***Nat Commun*** 2024.